

Q
225
N3
J4
1980
c.1

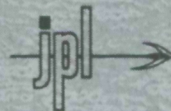
(NASA-CR-173535)
Propulsion Lab.)

JPL HIGHLIGHTS, 1980 (Jet
109 p

N84-74128
THRU
N84-74174
Unclass
13432
00/99

JPL HIGHLIGHTS 1980

ERBSAC
TECHNICAL INFORMATION CENTER



JET PROPULSION LABORATORY
CALIFORNIA INSTITUTE OF TECHNOLOGY
PASADENA, CALIFORNIA

ORIGINAL CONTAINS
COLOR ILLUSTRATIONS



JPL HIGHLIGHTS

1980

ORIGINAL CONTAINS
COLOR ILLUSTRATIONS

ERRSAC
TECHNICAL INFORMATION CENTER



JET PROPULSION LABORATORY
CALIFORNIA INSTITUTE OF TECHNOLOGY
PASADENA, CALIFORNIA

Page intentionally left blank

Page intentionally left blank

CONTENTS

INTRODUCTION	1
I. DEEP SPACE EXPLORATION	
A. Planets and Their Satellites	
Saturn	
Voyager Saturn Encounter	4
Saturn's Magnetic Field	7
Saturn's Rotation Rate	8
Vertical Structure of Saturn's Equatorial Ionosphere and Middle Neutral Atmosphere	10
Jupiter	
Jupiter's Newly Discovered Satellites	12
Jupiter's Red Spot Dynamics	14
Jupiter's Atmosphere Analyzed via Voyager Radio Occultation . .	17
Discovery of X-Ray Emissions From Jupiter	18
Mapping SO ₂ Frost and Sulfur on Io's Surface	20
Mars	
Viking Project	22
Venus	
Structures and Variations of the Atmosphere on Venus	24
Terminator and Nightside Ionosphere of Venus	26
B. Sun	
Solar Wind Latitude Variations	28
Solar Irradiance Studies on the Solar Maximum Mission	30
C. Astrophysics	
High-Resolution Gamma Ray Spectroscopy Experiment on HEAO 3 . .	32

D. Deep Space Navigation and Communication	
New Frequency Standard Test Facility	34
Improved Hydrogen Maser Performance	36
Distribution of Standard Frequency Signals by Microwave	38
Radio Source Catalogs	40
II. ENERGY AND ENERGY CONVERSION TECHNOLOGY	
Coal Pump Development	44
Supercritical Fluid Extraction of Coal	46
Solar Thermal Power Conversion	48
Extremely Low Energy Electron Studies of Gases Used as High-Voltage Insulators	52
Electric Power Systems Simulator	54
Stirling Laboratory Research Engines	56
III. EARTH ORBITAL APPLICATIONS	
Seasat Data Utilization: Scanning Multichannel Microwave Radiometer	60
Ocean Currents Measured by Seasat Radar	62
Ocean Wave Patterns Under Hurricanes	64
Project ARIES (Astronomical Radio Interferometric Earth Surveying)	66
Combining Seasat Radar and Landsat Multispectral Images	68
IV. INFORMATION SYSTEMS AND SPACE TECHNOLOGY DEVELOPMENT	
Dynamic Balancing in a Vacuum	72
Spacecraft Contamination Investigations	74
X-Ray Photoelectron Spectroscopy Interface Studies	76
Charged Coupled Imaging Device Test Facility	78
Development of an Ultraviolet Excimer Laser for Atmospheric Sensing	80

Advanced MPD Thruster Research	82
Nickel-Cadmium Battery Research	83
Coated Oxidizers for Stability in Space Propulsion Rockets . .	84
Fluorine-Hydrazine Propulsion System	86
V. TECHNOLOGY APPLICATIONS	
Aerosol Particle Analysis by Mass Spectrometry	90
Ocean Bottom Exploration System	92
The Hand-Held Ratioing Radiometer	94
VI. BASIC RESEARCH	
Low-Energy Ion Collision Studies	98
Studies of Atmospheric Photochemistry and Kinetics	100
INDEX OF NATIONAL AERONAUTICS AND SPACE ADMINISTRATION SPONSORING	
PROGRAM OFFICES	102

INTRODUCTION

The impressive revelations of Saturn's and Jupiter's environments by the twin Voyager spacecraft head this report on the significant accomplishments of the Jet Propulsion Laboratory in research and technology for the fiscal year ending September 30, 1980.

The entries were selected as the most important work completed during the fiscal year. Many of the achievements are in continuing programs and some are advances of work that was included in "JPL Highlights 1979."

Representing a broad spectrum of activities, the selections emphasize the three major programmatic goals of JPL: (1) the implementation of deep space missions for NASA, together with tracking and data acquisition and analysis; (2) a leadership role in the Department of Energy's solar electric development program for the nation; and (3) participation in Earth-orbital flight projects and experiments.

JPL often collaborates with other research centers, universities, and private industry. Where feasible, subcontracting is done. The Voyager Mission, as an outstanding example, is a multi-year collaborative effort involving thousands of scientists, engineers, and technicians from a variety of institutions and agencies in this country and abroad.

The first of this report's six sections summarizes major achievements in exploring the solar system and analyzing new discoveries produced by various planetary missions. These, of course, were highlighted by the photography of Saturn's rings and large moons by Voyager 1 prior to its encounter with the Saturnian system. The planetary radio astronomy experiment aboard the two Voyagers determined Saturn's

rotation rate at a very precise 10 hours, 39.4 minutes (plus or minus 9 seconds). Data on Saturn's magnetic field, ionosphere, and middle atmosphere, acquired previously by the Pioneer 11 flyby, have been analyzed.

The Voyager team discovered three new tiny moons around Jupiter to bring that planet's satellite total to 16. Jupiter's Great Red Spot has winds of over 100 meters per second (225 miles per hour), a dynamics study found. Profiles of gases, pressure, temperatures and microwave absorption in Jupiter's troposphere and stratosphere were made. That Jupiter emits X-rays was discovered by a special telescope aboard the HEAO 2 satellite. And JPL laboratory work determined that sulfur dioxide frost covers almost 20 percent of the Jovian moon Io.

The conclusion of Viking Orbiter activity after four years at Mars was marked by a bonus of 2770 medium-resolution photographs that will help complete maps 2.5 times the scale of the previous best of Mars. Viking Lander 1 is still active on Mars and is programmed to send data until December 1994.

Radio occultation techniques used with the Pioneer Venus Orbiter produced measurements of the Venusian cloud structure and the electron density of the ionosphere.

Several solar studies included a solar wind finding, based on Mariner 10 (Mercury-Venus Mission) data, of the out-of-ecliptic flux. Fluctuations of the sun's radiation output were measured with a new sensitivity by a JPL instrument aboard the Solar Maximum Mission spacecraft. A high-resolution spectrometer aboard the HEAO 3 satellite confirmed the existence of a strong electron-positron annihilation line from the center of our galaxy.

Upgrading of the Deep Space Network continues to meet requirements for communicating with and guiding spacecraft at distances of the outer planets. The DSN improved hydrogen maser performance for greater frequency stability and developed a frequency standard test facility. Radio astrometric catalogs of 170 quasars and 109 other radio sources were compiled.

JPL's work in the energy field, summarized in the second section, includes several promising technology developments in the Solar Thermal Power Systems program for DOE. Coal pump and fluid extraction methods were studied, along with gaseous insulation for high-voltage electrical power transmission. A computerized simulator of electrical power systems operations was built for utilities use. A Stirling engine prototype was developed for ongoing research.

Earth orbital applications, covered in the third section, were widened through continuing processing of Seasat and Landsat data. Advances were made by Seasat radar measurements of ocean current and hurricane wave effects. ARIES, an interferometric Earth-measuring system using a portable antenna, continued to develop data of potential use in understanding earthquakes.

The fourth section describes new instruments and technology advances for space application. These include research gains in rocket propulsion systems, nickel-cadmium batteries, spacecraft contamination monitoring, and ultraviolet laser development for atmospheric sensors. For the space-photo systems of the 1980s and 1990s, a new facility has been built for testing charge-coupled devices (CCDs).

In technology applications for basically terrestrial use, found in section five, JPL produced three diverse endeavors. One, a mass spectrometer system, promises to be a useful tool in identifying air-polluting aerosols. Image-enhancement techniques developed by space programs proved applicable to mid-Atlantic ocean bottom imaging for a British oceanographic venture. And a likely geological tool was developed -- a hand-held ratioing radiometer which can identify minerals for an investigator in the field.

The sixth and final section, covering the important area of basic research, reports on laboratory studies of how low-energy ion collisions may activate electrons in the atmosphere and space. Moreover, laboratory techniques were developed for studying gas-phase chemical reactions in the atmosphere.

I. Deep Space Exploration

21

VOYAGER SATURN ENCOUNTER

The observatory phase of the Voyager 1 encounter at Saturn began August 22 and ran through October 24, 1980. The two-month period produced many spectacular pictures of the planet, its rings and moons before the November 11-13 near-encounter phase.

The historic picture (opposite page) of ringed Saturn and six of its moons was taken by Voyager 1 on September 17 from a distance of 76 million kilometers (47 million miles). The quality and resolution of the image are far superior to the best Earth-based photographs.

Saturn's largest moon, Titan, is the reddish disk visible at the mid-upper right. This satellite, almost twice the diameter of Earth's moon and known to have a significant atmosphere, was targeted for close scrutiny by Voyager 1 on November 12, 18 hours before closest Saturn approach. The spacecraft was to fly within 4000 km of Titan's cloud tops and proceed behind the satellite for experiments which analyze sunlight and radio waves passing through the atmosphere.

Five of Saturn's other inner satellites are also shown. Mimas, closest to Saturn, and Enceladus are located just below Saturn's outer ring (right center). Rhea, Tethys, and Dione (left to right) are seen in the upper left corner. During a 2-1/2-hour period on November 13, Voyager 1 was scheduled to pass close to Mimas, Dione, and Rhea (89,000, 161,000, and 73,000 km, respectively).

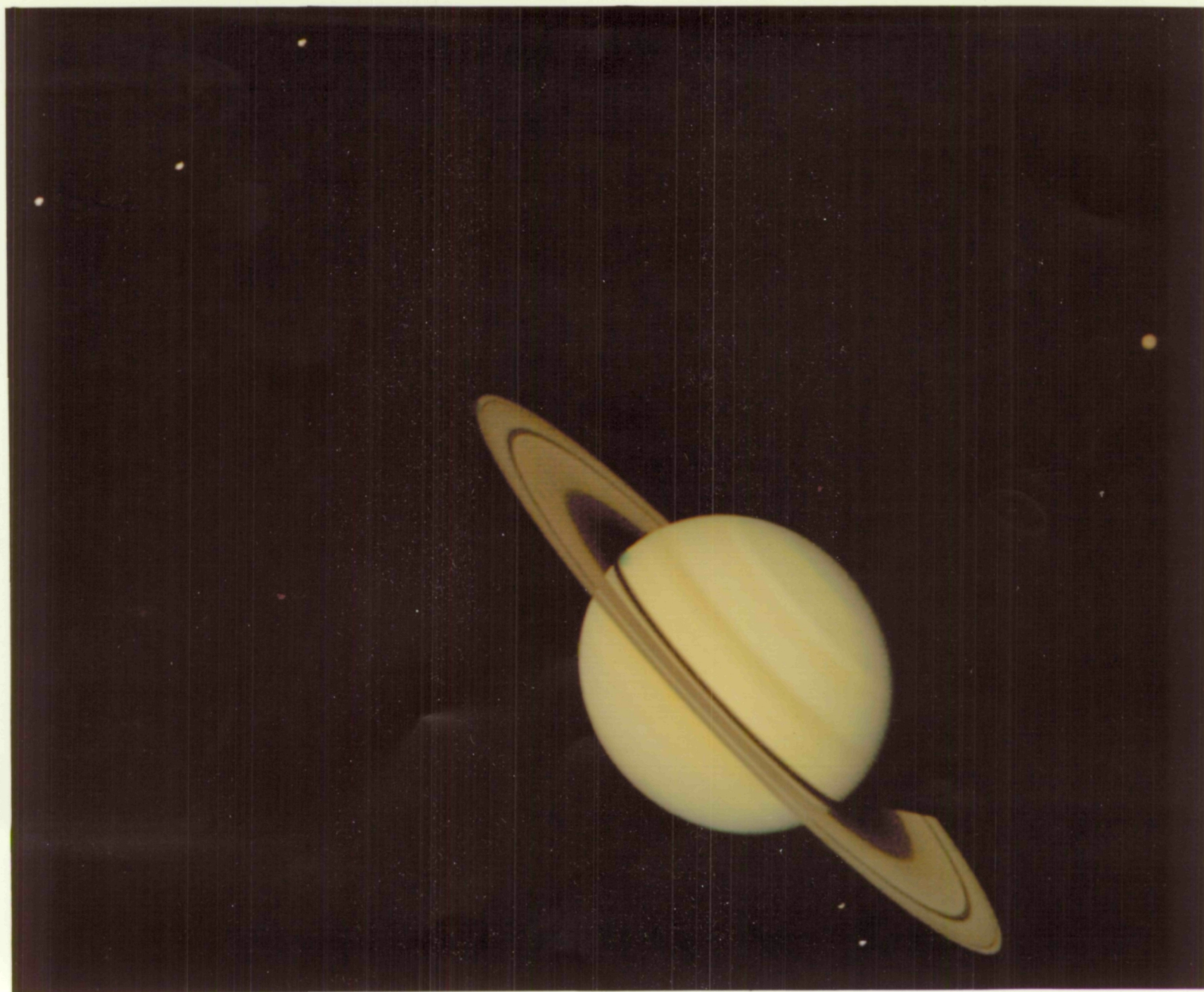
To capitalize on the particularly close Rhea flyby, extraordinary efforts were planned to reduce the image smear that would normally occur during photography at high velocity so far from the sun. During part of the flyby the spacecraft was to be maneuvered at a rate and in a direction chosen to compensate for Rhea's motion.

Enceladus and Tethys will be best photographed by Voyager 2 when it flies through the Saturn system in August 1981.

Also shown in this photograph is significant detail in Saturn's rings including the Encke (outer) and Cassini (inner) Divisions. Radial variations and gaps never observed before are pictured, including at least two narrow rings of material within the Cassini Division. Also revealed in the Voyager data are dark features which extend radially out through the rings. Such circumferential asymmetries are inconsistent with previous theoretical models of the rings.

During the approach, Voyager images disclosed many discrete features in Saturn's atmosphere, which permitted the measurement of wind velocities at many latitudes.

The early Voyager observations indicate clearly that, despite many fundamental similarities between Jupiter and Saturn, the latter planetary system has many characteristics which, so far, appear unique in the Solar System.



Page intentionally left blank

SATURN'S MAGNETIC FIELD

A JPL magnetometer aboard Pioneer 11, the first spacecraft to fly past Saturn, detected that planet's magnetic field and determined its properties. The field, it was found, extends beyond a million kilometers from the planet and, unlike Earth, Jupiter, and Mercury, exhibits a high degree of symmetry about Saturn's axis of rotation. Thus, the equivalent magnetic dipole source is tilted only slightly with respect to the pole. The magnetic pole is less than one degree from the rotational axis, and the magnetic moment is 0.2 gauss r^3 .

The strength of the field is 0.2 gauss atop the atmosphere at the equator, slightly less than the

Earth's field at the corresponding location. It is slightly stronger at the north pole, 0.63 gauss, than at the south pole, 0.48 gauss, because the magnetic source is slightly north of the equator.

The planetary magnetic field was found to be deformed by the interplanetary wind streaming outward from the sun. The field is compressed near noon (observed when Pioneer was inbound) and stretched into a long magnetic tail near dawn (when Pioneer was outbound). Saturn's magnetic field forms a cavity from which the solar wind is excluded.

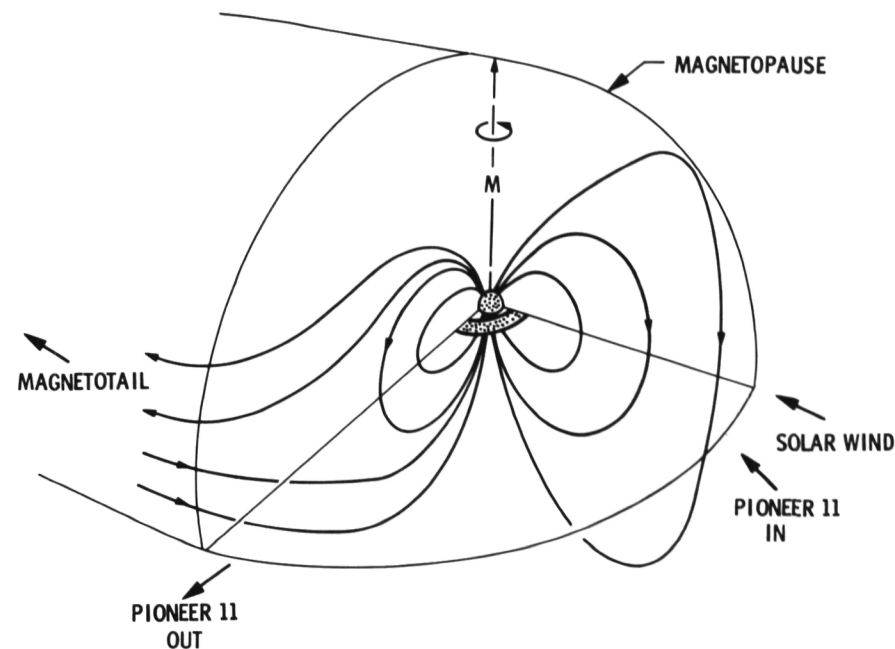


Diagram of the magnetic field of Saturn as observed by Pioneer 11. During the outbound portion of the trajectory, Pioneer observed that the magnetic field lines were being swept downstream to form a long tail. Saturn's magnetic dipole (capital M) is nearly aligned with the rotation axis of the planet. The magnetopause represents the boundary of the region from which the solar wind is excluded by the planetary field.

93

SATURN'S ROTATION RATE

The planetary radio astronomy experiment aboard the two Voyager spacecraft has determined the rotation rate of Saturn to be 10 hours, 39.4 minutes \pm 9 seconds. Such a precise measurement was not possible before for several reasons. Previous outer planet spacecraft did not carry instrumentation required for obtaining the data. Also, the measurements are impossible from Earth because of the great distance (8.54 astronomical units) and the fact that Saturn's peak radio emissions fall in the standard AM radio broadcast band used on Earth. Previous measurements by ground-based astronomy have measured the rotation of Saturn's clouds, not the rotation of Saturn itself.

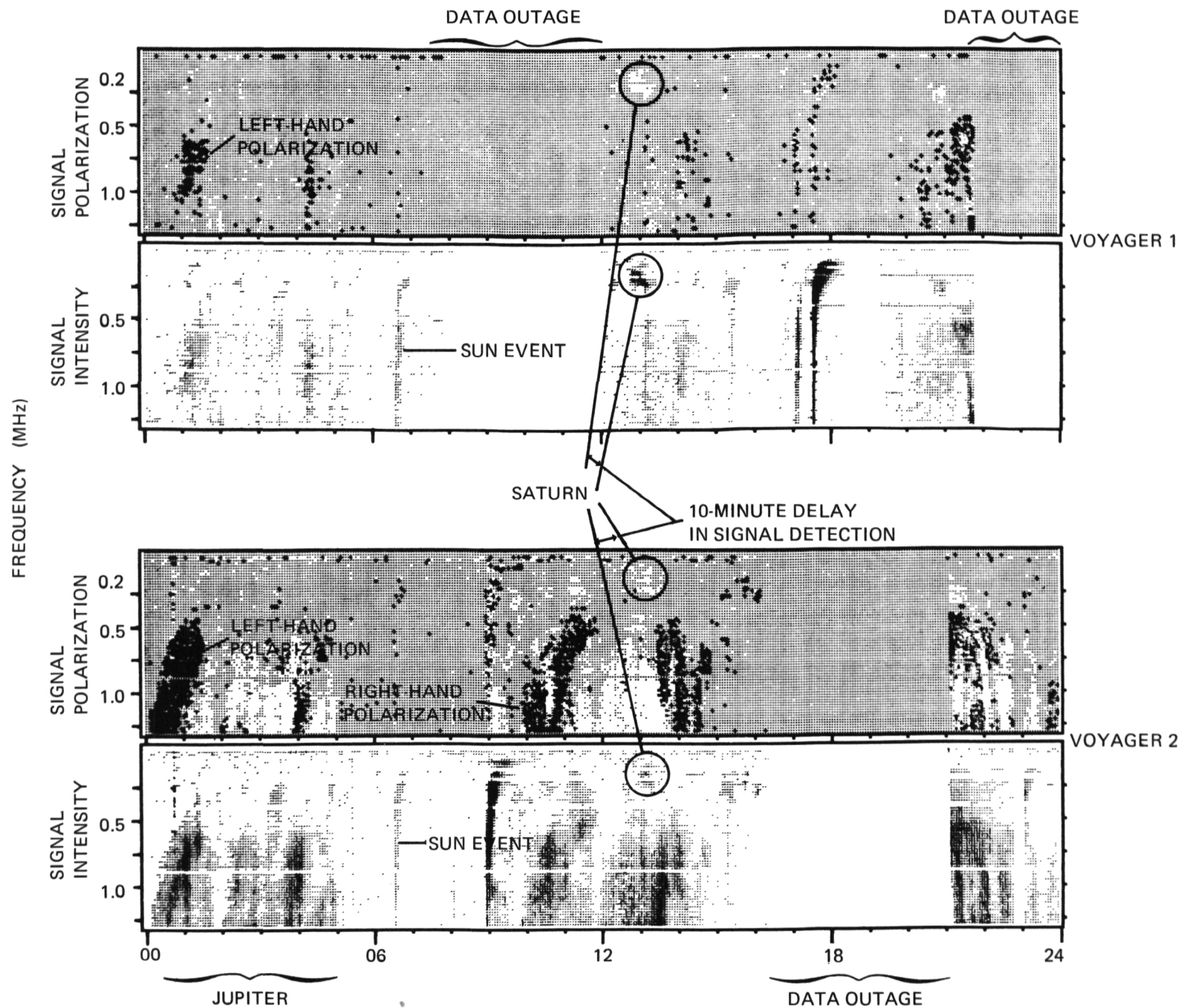
Correlation of data acquired by both spacecraft shows cyclical bursts of non-thermal radio noise from Saturn at regular intervals of 10 h, 39.4 min. The noise frequency is near 200 kilohertz, and the radiation is right-hand polarized. It most likely is emitted in the extraordinary magnetoionic mode from Saturn's northern hemisphere.

The emissions were distinguished by several criteria from Jupiter's bursts, from solar type III bursts, and from background noise. First, only the signals that were stronger for Voyager 1 were counted because that spacecraft was closer to Saturn than Voyager 2. Secondly, the light-time delay of 10 min between the Voyagers also was used to identify the right signals. Finally, the spectral character and polarization of the Saturn events are distinct from solar type III bursts and the Jovian emissions.

The initial rotation rate determination was based on a survey of 33 events totaling 24.5 h of activity over 40 days. Subsequent measurements refined the rate by 0.5 min.

The ability to determine a rotation period implies a deviation from perfect axial symmetry of the planetary magnetic field.

Figure (opposite page): The Saturn rotation rate was determined by interpretations of a large number of plots similar to the one shown. The four rectangles contain typical plots of radio signals from Saturn, Jupiter and the sun as received by the two Voyager spacecraft in the indicated 24-hour period. The white background plots show intensity signals while the gray ones show the corresponding polarizations. In the gray polarization plots, left-hand polarization is shown as black, right hand as white. Typical Jovian emissions and solar bursts are indicated. Saturn emissions are circled. The Saturn emissions repeat every 10 hours, 39.4 minutes to give the rotation rate of the planet's core. The Jupiter emissions repeat every 9 hours, 55.5 minutes, and the solar events are unpredictable. Some data outages are shown for both spacecraft.



24

VERTICAL STRUCTURE OF SATURN'S EQUATORIAL IONOSPHERE AND MIDDLE NEUTRAL ATMOSPHERE

Radio occultation data at S-band frequency (2.293 gigahertz) collected during the close flyby of Saturn by the Pioneer 11 spacecraft in September 1979 produced important first results on the structure of the Saturnian ionosphere and middle neutral atmosphere near the equator. This was accomplished despite strong perturbations from fluctuations of solar wind plasma electrons resulting from the proximity of the Earth-Saturn line of sight to the sun of 8 degrees.

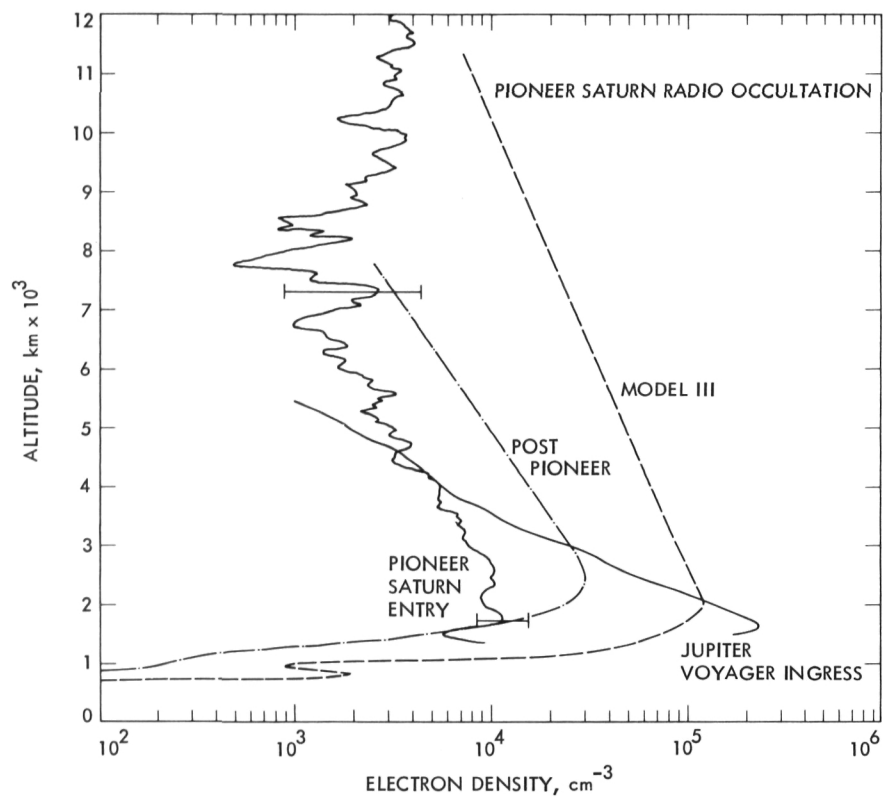
It was found that the principal electron density peak of the ionosphere occurs at an altitude of about 1800 kilometers and has a maximum density of 11,400 electrons per cubic centimeter, with a narrow lower peak of 9000 electrons per cubic centimeter, some 600 km below the main peak. The measured scale height indicates an exospheric temperature of about 1150 kelvins for an H^+ ionosphere. Ionization appears to extend to a radial distance of 80,000 km, with a broad peak of 7000 electrons per cubic centimeter at 74,500 km, corresponding to the radial distance of the inner edge of the C-ring.

The unexpectedly low density of the main peak could be explained by the presence of an equatorial

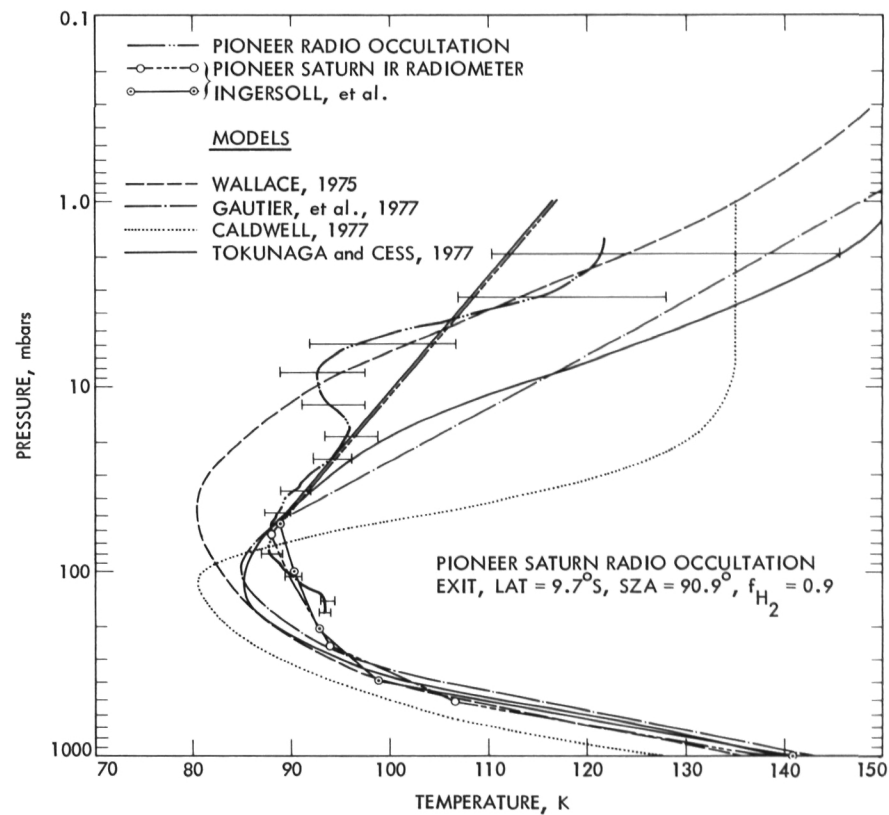
anomaly and by the effects of ring shadowing. The presence of significant ionization above the main peak, if real, could be explained if the main peak electron densities of about 100,000 electrons per cubic centimeter exist at higher latitudes, which are connected to the equatorial site of measurement by magnetic field lines. Plasmaspheric heating by Saturn's rings may also be important.

In the neutral atmosphere, measurements were carried out to the pressure level of about 180 millibars, showing the temperature inversion region having a triple minimum. The temperature at the principal minimum at an equatorial radius of 60,344 km is 88 ± 4 K at a pressure of 74 mbars, and there is another prominent minimum about 80 km above the principal one.

Comparisons of the temperature structure with the results derived from the Pioneer 11 Saturn Infrared Radiometer data suggest that the fraction of helium (by number) in the Saturnian atmosphere is 10 ± 4 percent, which is similar to the helium fraction in the atmosphere of Jupiter, as deduced by Voyager investigators.



Electron Density structure of the equatorial ionosphere of Saturn as determined from Pioneer 11 radio occultation data. Model III refers to a model by J. H. Waite et al., and the Post Pioneer model is one taking ring shadowing into account and computed for a solar zenith angle of 80 degrees. The remaining discrepancy between the observation and the model may be explained by equatorial anomaly.



The radio occultation temperature structure in the middle atmosphere of Saturn (curve with error bars) compared with Pioneer 11 infrared radiometer temperature retrievals (straight line segments) and several models based on ground-based infrared observations. The wavy nature of the radio occultation profile could indicate the effect of gravity waves, or it could be an artifact introduced by the spacecraft oscillator.

Db

JUPITER'S NEWLY DISCOVERED SATELLITES

Before Voyager the only small satellite thought to orbit closer to Jupiter than the Galileans was Amalthea. The Voyager data have revealed the existence of at least three other small satellites.

The first new satellite, 1979J1, was discovered in long exposure frames taken 23 hours before the closest approach of Voyager 2 to Jupiter primarily to study the Jovian ring. The two discovery frames are the only data that so far have been found for 1979J1, and they indicate that it has an orbit period of about 7 h, 8 min and is 30 to 40 kilometers in diameter. It orbits at about 57,800 km above Jupiter's cloud tops. 1979J1 was discovered in October 1979.

An attempt in March and April 1980 to find data confirming the existence and orbit of 1979J1 then led to the discovery of two other small satellites. A shadow was observed on the Jovian atmosphere in frames taken 4-1/2 h before Voyager 1's closest approach to Jupiter in March 1979. The shadow could not have been caused by any satellite known at the time, and an analysis of the motion of the shadow allowed a calcu-

lation of the satellite's orbit and a prediction of its reappearance in other Voyager 1 frames. It was subsequently found many more times in both Voyager 1 and Voyager 2 frames. This new satellite, 1979J2, was found to have an orbit with a period of 16 h, 11 min and to be 80 km in diameter. It orbits at about 151,000 km above Jupiter's cloud tops.

During this same search through Voyager 1 frames, a satellite/shadow pair was observed moving across the equatorial region of Jupiter. At first this satellite was thought to be the desired confirmation of the existence of 1979J1, since the satellite size and orbit inferred from the new data were very similar to those of 1979J1. A detailed analysis of this and other data, however, proved that this satellite would be in a position on the far side of Jupiter at the time of the original discovery frames of 1979J1. This new satellite, 1979J3, was subsequently found in Voyager 2 frames very near the position predicted from the Voyager 1 data and found to have an orbit period of 7 h, 4 min, 30 s, and to orbit 56,200 km above Jupiter's cloud tops. Its diameter is about 40 km.

Figure (opposite page): The largest of the three tiny new moons of Jupiter discovered by the Voyager Project is seen against the face of the planet. Its dramatic shadow is visible at the end of the dark streak in the Jupiter clouds (right center). The new satellite, designated as 1979J2, is only 80 kilometers in diameter and orbits Jupiter about 151,000 kilometers above the cloud tops.



76

JUPITER'S RED SPOT DYNAMICS

Our understanding of Jupiter's dominant feature, the spectacular Great Red Spot (GRS), has been greatly enhanced by studies of many pictures taken of it by the Voyagers. The images were improved by special techniques employed by JPL's Image Processing Laboratory (IPL).

The GRS supposedly was discovered by Sir Robert Hooke over 300 years ago, and has been observed more or less continuously for 100 years. A vast, elliptical anticyclone covering over 200 million square kilometers, it is the largest known single atmospheric vortex.

Voyager photo sequences designed to measure motions in and around the GRS confirm that the highest velocities, over 100 meters per second (some 225 miles per hour), are concentrated in a white and hazy oval ring around the storm's periphery. The velocities are very low in the redder interior.

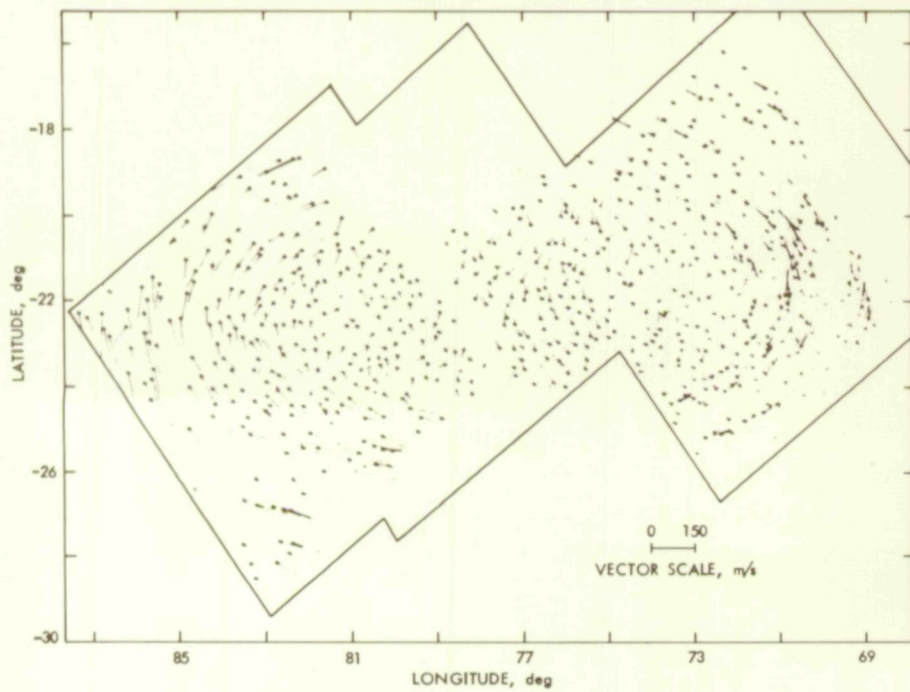
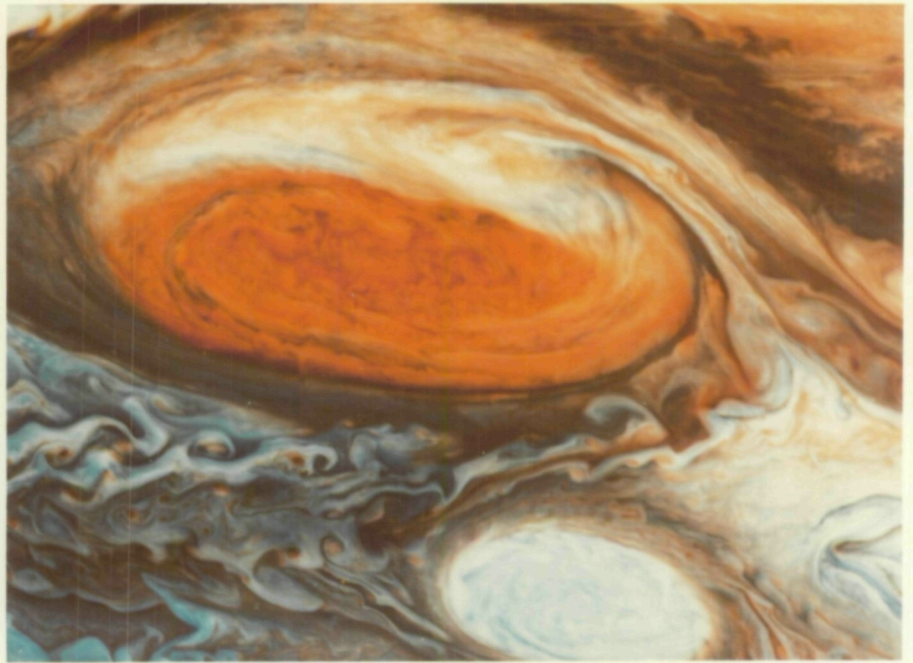
The dynamics of white, oval, Earth-size storms in the Jovian atmosphere appear to be remarkably similar to that of the GRS, except for the latter's quiescent interior.

The three-fold difference in size between the GRS and the white ovals can probably be explained by the difference in latitudes of these features. This can be taken to mean that the GRS is not unique but rather is the largest of many vortices in the swiftly spinning Jovian atmosphere.

Ongoing JPL studies make use of the measured velocity fields around the GRS and white ovals to identify energy sources for Jupiter's long-lived storms. A major question that soon should be answered is: Does the ambient wind drive the GRS or is the opposite true? These studies hold the key to unlocking the secrets of the mysterious, beautiful Great Red Spot.

Special enhancement of Voyager pictures by IPL made possible the inference that higher velocities existed around the periphery of the GRS. The Voyager color photographs consisted of a blend of several monochromatic, digital images. IPL made the red parts redder and the blue parts bluer, facilitating the studies of cloud structures associated with the Great Red Spot.

Figure (opposite page): At top left, Jupiter (with Great Red Spot just below center) is seen by Voyager 1 from 40 million kilometers distance. In top right, Great Red Spot is shown from only 24,000 kilometers, and, lower right, at the same distance but greatly enhanced with smallest features visible about 30 kilometers across. White feature below the GRS is one of several white ovals first observed 40 years ago from Earth. Lower left drawing shows how Great Red Spot winds swirl, many of them at speeds well over 200 mph (100 to 150 meters per second).



Page intentionally left blank

D7

JUPITER'S ATMOSPHERE ANALYZED VIA VOYAGER RADIO OCCULTATION

Radio occultation measurements with Voyagers 1 and 2 have provided new information on the troposphere and stratosphere of Jupiter. Observations of spacecraft radio signals at 2.3 and 8.4 gigahertz have yielded profiles in height of the gas refractivity, molecular number density, pressure, temperature, and microwave absorption at latitudes ranging from 0 to about 70 degrees south. The data cover a pressure range from 1000 millibars to 1 millibar over a height interval of 160 kilometers.

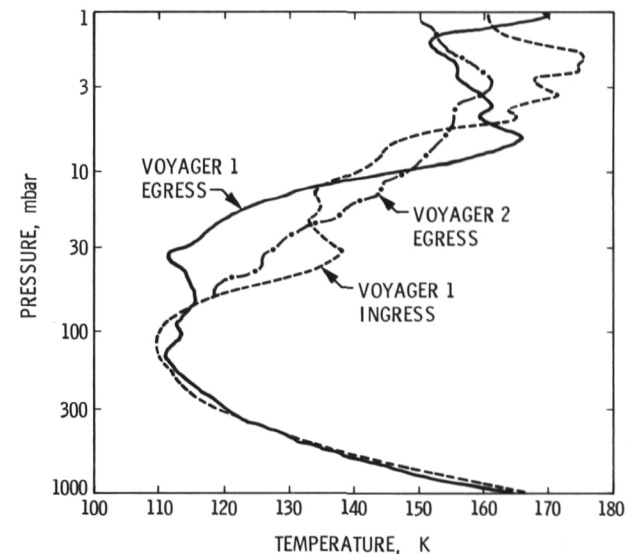
At the 1000-mbar level, the temperature was 165 ± 7 kelvins; the main error source is the current uncertainty in the hydrogen-to-helium mixing ratio. The temperature lapse rate was equal to the adiabatic value of 2.1 K per kilometer, within the resolution of the measurements. The ammonia abundance in this region of the atmosphere was about 0.022 ± 0.008 percent -- in approximate agreement with the value derived from

cosmic abundance considerations. The tropopause, which was detected near the 140-mbar level, had a temperature of 110 K.

Above the tropopause, the temperature increased with altitude, reaching 160 ± 20 K in the 10- to 1-mbar region of the stratosphere. Significant horizontal density variations were detected in the stratosphere. This may imply a non-uniform temperature and aerosol distribution across the Jovian disk, or high- and low-pressure regions due to local atmospheric dynamics. The gravity equipotential surface which best fits the 100-mbar isobaric surface has an equatorial radius of $71,541 \pm 4$ km and a polar radius of $66,896 \pm 4$ km.

This is the joint work of JPL, Stanford University's Center for Radar Astronomy, and SRI International's Radio Physics Laboratory.

Temperature profiles derived from doppler frequency perturbations observed on the S- and X-band tracking links during the occultations of the Voyager spacecraft by Jupiter. These profiles were computed for a gas mixture of 89 percent H_2 and 11 percent He.



98

DISCOVERY OF X-RAY EMISSIONS FROM JUPITER

Observations made with the focusing X-ray telescope on the High-Energy Astrophysical Observatory HEAO 2 have resulted in the discovery of X-ray emission from Jupiter. The findings are expected to add to our knowledge concerning the belts of trapped, energetic, charged-particle radiation that surround the planet, and could provide new information on the surface composition of Jupiter's large moons. Analysis of the results is being conducted by JPL in collaboration with scientists at the Massachusetts Institute of Technology, Smithsonian Astrophysical Observatory, the Danish Space Research Institute, and the French Center for the Study of Space Radiation.

A search to detect X-rays produced within Jupiter's magnetic field began several years after the detection of radio wave emission, based on an analogy of terrestrial aurorae that are accompanied by X-ray emission. Since the Earth's atmosphere is opaque to X-rays, experiments have been carried out on balloons, rockets, and satellites. During this search the measured upper limits of emission have been reduced by several orders of magnitude. In recent years there has been a study at JPL to calculate the X-ray emission from the Galilean satellites resulting from their bombardment by the energetic particles in Jupiter's radiation belt. The observed X-rays fall in the 0.2

to 3-keV range. The preliminary analysis indicates that most, if not all, of the observed X-rays are coming from the proximity of Jupiter itself.

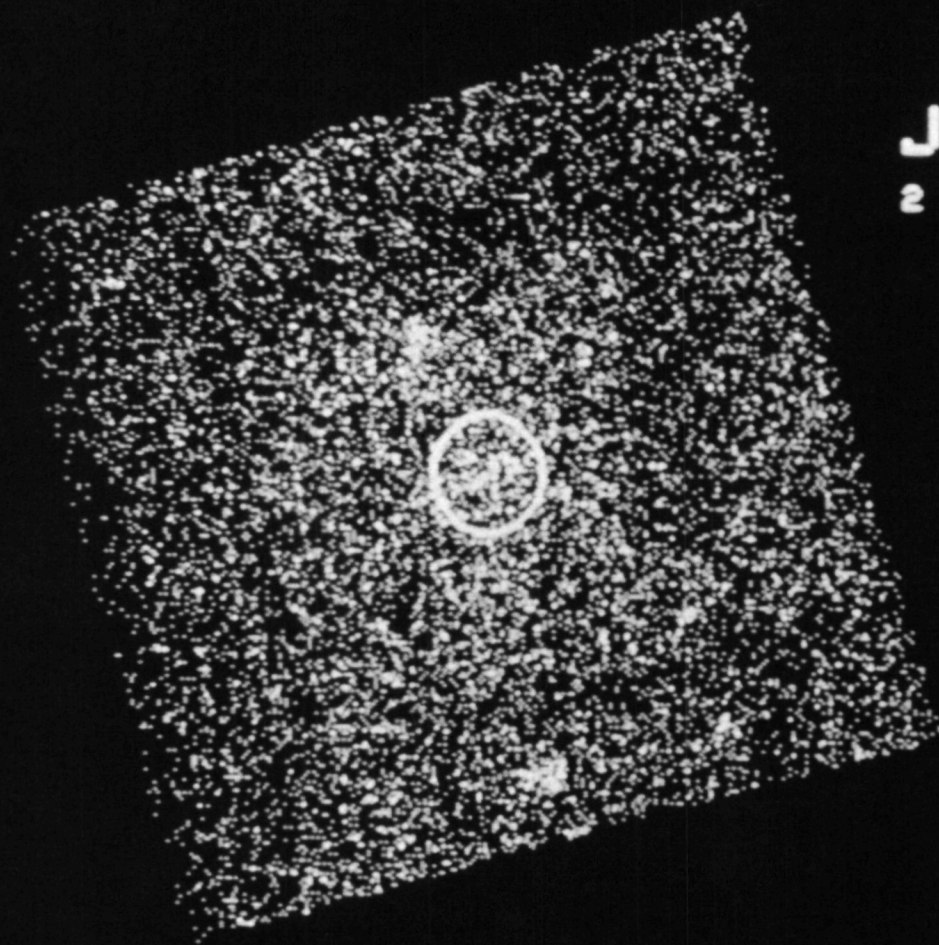
The recent observation of Jovian aurora made by the ultraviolet experiment on the Voyager 1 and 2 spacecraft suggests a common origin for the X-rays. The UV and X-ray emission may be products of a similar mechanism -- from free electrons interacting with particles in the atmosphere of Jupiter.

The X-ray observations provide a new method of studying the characteristics of the Jovian magnetosphere to improve our understanding of the mechanisms by which energy is provided to Jupiter's magnetic field, transferred to the radiation flux within it, and subsequently dissipated. Because the measurements can be made by an Earth satellite, they can be made over long periods of time.

A comparison of these observations, with relevant measurements made by the UV spectrometer, particle flux detector, and radio astronomy instrument on the two Voyagers, is expected to assist in their interpretation as well as in planning future X-ray observations of Saturn and Uranus.

Figure (opposite page): One of the three observations of X-ray emission from Jupiter made by the Einstein (HEAO 2) Observatory in 1979 using an Image Proportional Counter positioned at the focus of the X-ray telescope.

EINSTEIN OBSERVATORY
SEQUENCE: 7106
RA, DEC: 160.942 9.137
SECONDS: 9209
OBSERVER: JMAC
DATE: 83-DEC-79



JUPITER
2 ARC-MIN: H

DO9

MAPPING SO₂ FROST AND SULFUR ON IO'S SURFACE

Laboratory experiments on SO₂ frost and other sulfur compounds were combined with observational data from the International Ultraviolet Explorer (IUE) spacecraft to estimate the distribution of SO₂ and sulfur on the surface of Io, which is in synchronous rotation about Jupiter. The results have been indirectly confirmed by the Voyager spacecraft.

JPL research has established that frozen SO₂ is more abundant on Io's leading side at longitudes between 72 and 137 degrees, and that sulfur allotropes are most abundant on the trailing side at longitudes from 250 to 323 deg.

Last year JPL experimenters identified frozen SO₂ as a significant component of Io's surface material by comparing laboratory infrared reflectance spectra of SO₂ frost with Earth-based telescopic spectra of Io. This year the observational and laboratory work was extended into the ultraviolet to learn more about Io's surface composition. A laboratory spectrum of SO₂ frost was measured in the ultraviolet and visible spectral range. When compared with Earth-based spectra of Io, the new laboratory data served to strengthen the case for the existence of an SO₂ solid phase on the satellite, and at the time to set an upper limit on the

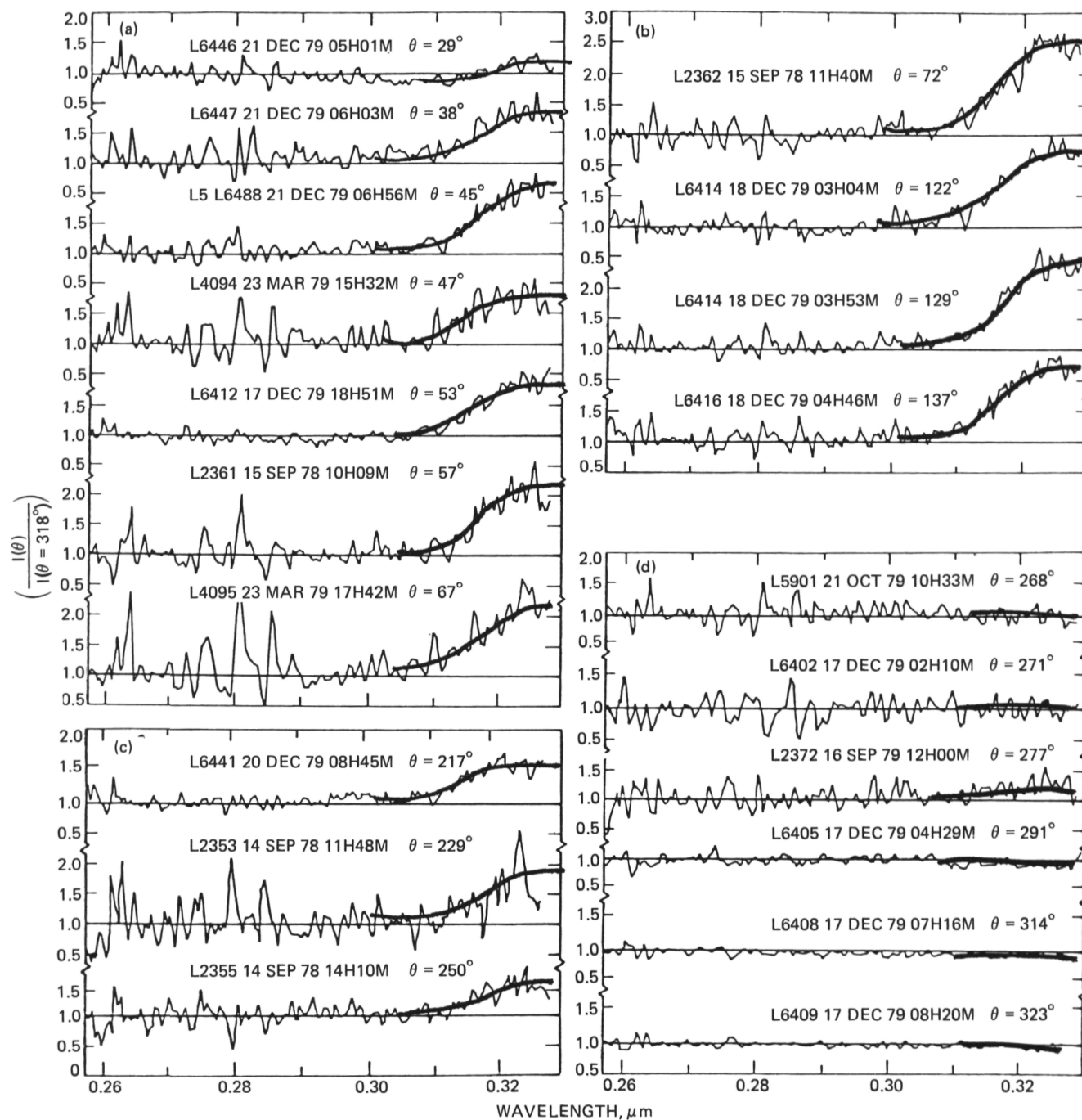
fraction of Io's disk that is covered by SO₂ frost at less than 20 percent.

Analysis of 20 IUE ultraviolet spectra of Io, gathered by JPL observers using IUE, showed that the strength of the distinct ultraviolet absorption band they found near 0.31 micrometer varied systematically with Io's orbital phase angle (i.e., the position of Io in its orbit about Jupiter) at the time of each observation. This discovery, combined with Io's synchronous rotation about Jupiter, led to the conclusion that the abundance of frozen SO₂ on Io varies with longitude.

The variation in frozen SO₂ abundance is inversely related to another spectral feature on Io at 0.4-0.5 μm that had been attributed by previous observers to the presence of allotropic forms of sulfur. Thus, it was concluded that at Io longitudes where frozen SO₂ is most abundant, the sulfur allotropes are least abundant and vice versa.

While the Voyager imaging cameras were not designed to respond to the 0.31- μm feature in frozen SO₂, the spacecraft saw the white areas on Io. The whitest areas correspond to those with the heaviest concentrations of SO₂, according to IUE observations.

Figure (opposite page): Io's sulfur dioxide frost is shown in the broad band marked on these data charts of the IUE spacecraft measurements of the variation of Io's ultraviolet spectral reflectance. All spectra have been divided by the spectrum at an orbital phase angle of theta equals 318 degrees. Changes in the spectral intensity between 0.30 and 0.33 μm are interpreted to be due to variations in the fractional cover of SO₂ frost on Io's apparent disk as observed by IUE from Earth orbit.



D10

VIKING PROJECT

The most significant fact about the Viking Mission in 1980 is that it was still active, after producing more information about Mars than all previous observations combined. Of the four Viking spacecraft that began observing Mars in the summer of 1976, two were still operating in 1980, and one has been programmed to continue transmitting data to December 1994. The mission of two orbiters and two landers was originally designed for only 90 days!

The one spacecraft still active, Viking Lander 1, has made surface pressure observations that reveal a dramatic amplification of the global-scale atmospheric tidal components during great dust storms on Mars. At the time of the storms in 1977, absorption of solar radiation by airborne dust produced an enormous thermal tidal forcing.

A newly developed model can infer the effective opacity of the haze during the great dust storms by choosing that opacity which reproduces the amplitude of the twice daily surface pressure oscillation observed at Viking Lander 1. The model simulation of past storms is remarkably good. Future episodes of Martian great dust storms can be monitored as Lander 1 continues to measure pressure.

From November 1979 to July 1980, Orbiter 1 took more than 7000 pictures. Some 2770 of them filled in the remaining gaps in the medium-resolution mapping of the planet's surface. Not even considered in the orig-

inal Viking planning, this program provided the data base from which the U.S. Geological Survey is generating a new set of Mars maps at 2.5 times the scale of the Mariner 9 maps.

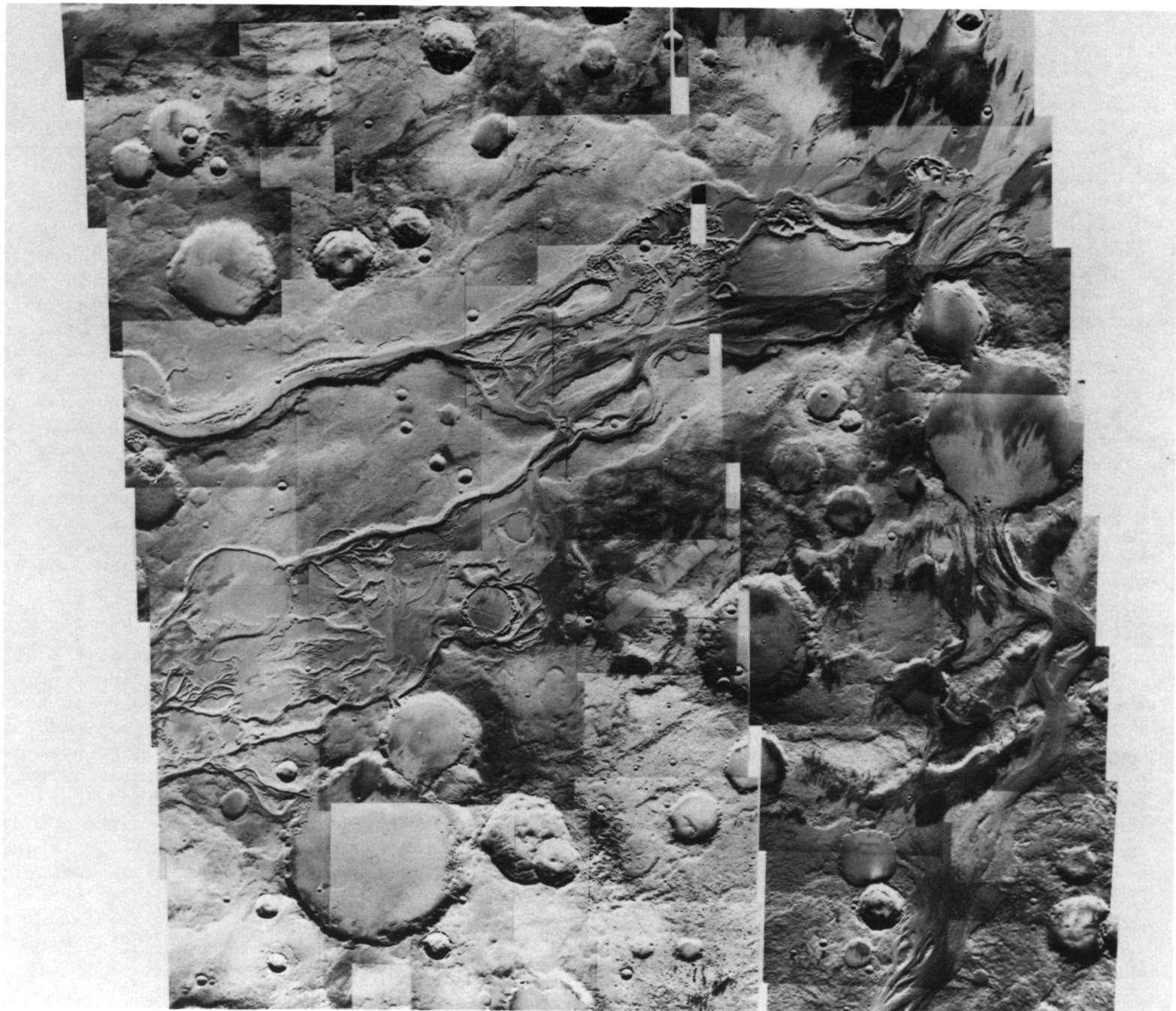
The orbiter's infrared measurements of temperature and water vapor abundance continued at a low level. Its radio systems continued to measure the Earth-Mars distance, the Martian gravitational field, radius, and atmosphere. Finally, its attitude control gas was exhausted and its transmitter was turned off on August 7 after it had made 1488 orbits of Mars.

The lander mission during 1980 was also restricted to photography, meteorological measurements, and radio science. Lander 2's last transmission was on April 11 after its batteries had degraded to the point where it could no longer support the power requirements.

Lander 1 continues to acquire data automatically, transmitting weekly to Earth if enabled by a signal from the Deep Space Network. Viking Orbiter 2 was shut down July 24, 1978, after running out of attitude control gas.

The data obtained from the two landers and Orbiter 1 in 1980 has been of excellent quality. The magnitude of their contribution to our understanding of Mars will become known in the future. Few of the pictures have yet to be processed, and the data analysis is in its early stages.

Figure (opposite page): This photomosaic of the Mangala Vallis region of Mars was taken by Viking Orbiter 1 on three successive days, June 19-21, 1980, commemorating the fourth anniversary of Viking 1's arrival at Mars. The pictures were taken at a range of 1600 kilometers. The geologically varied region lies southwest of Olympus Mons near the Martian equator and contains vast channel systems that appear to have been carved by running water in the distant past.



21

STRUCTURES AND VARIATIONS OF THE ATMOSPHERE ON VENUS

The radio occultation experiment aboard the Pioneer Venus Orbiter has been used to study latitudinal variations in the vertical structure of the Venus atmosphere and cloud morphology in the polar regions of Venus. As the spacecraft, which has circled Venus every 24 hours since December 1978, passes behind the planet in relation to the Earth, its radio signals (13.06 and 3.56 centimeters) are occulted.

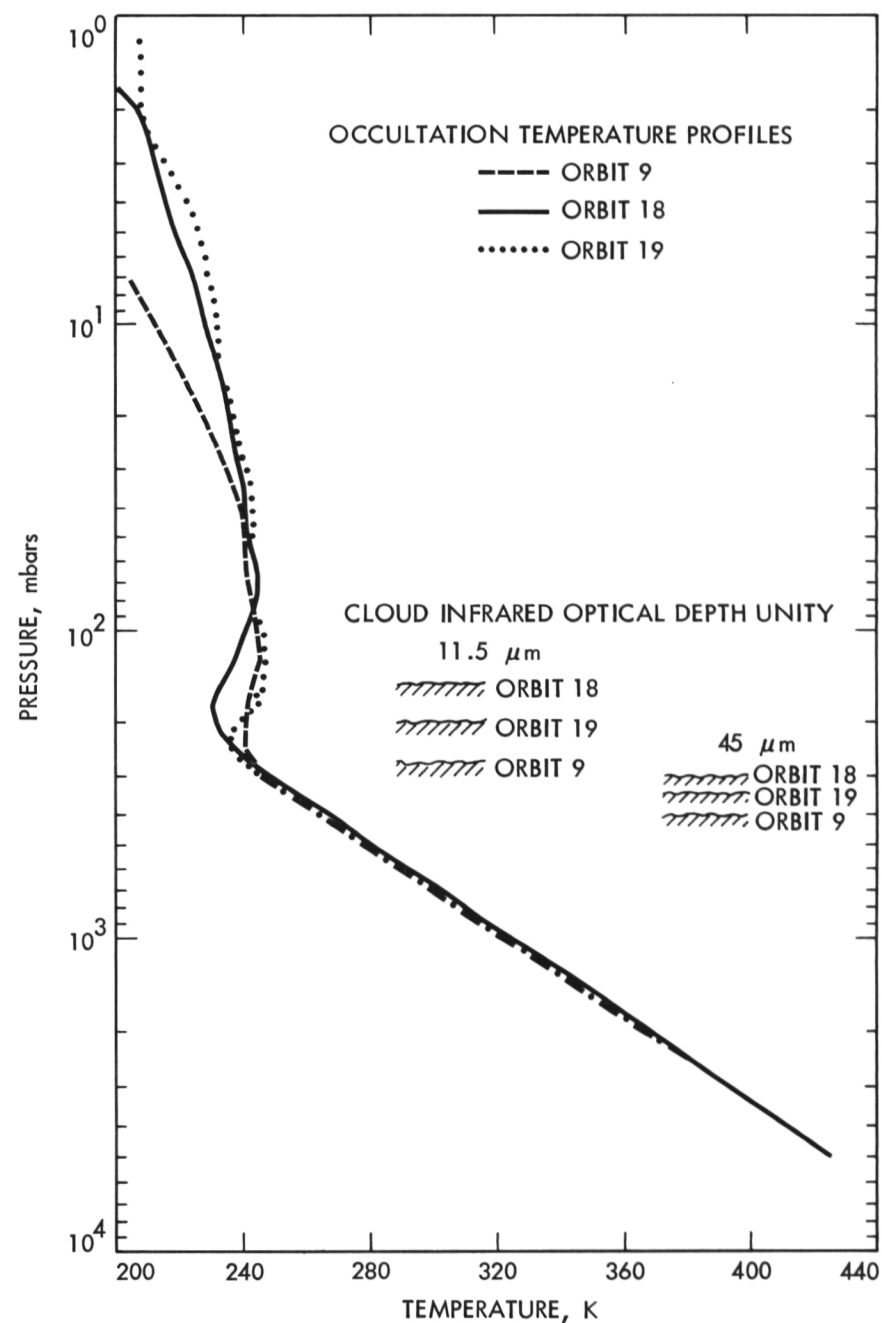
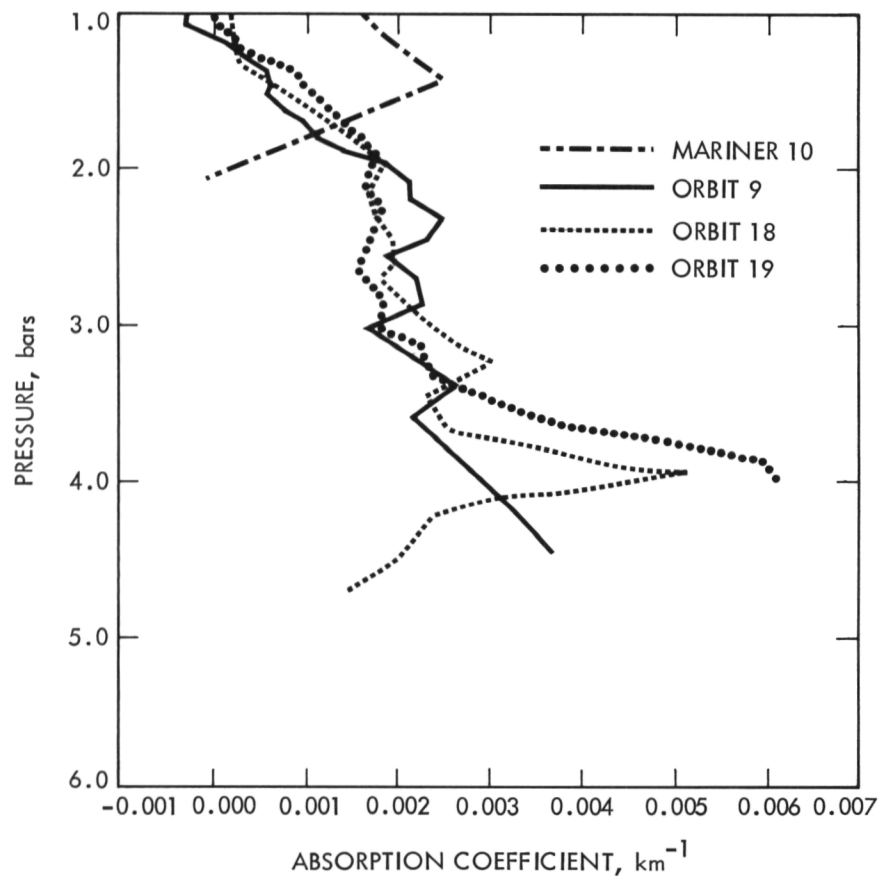
Many radio occultation data sets, taken at different latitudes, have provided information on changes in the temperature structure with latitude. Thirteen measurements taken at north and south latitudes ranging from 7.1 to 88.3 degrees have revealed the existence of a temperature inversion at the level of the tropopause. The tropopause is a region of transition between the troposphere, in which convection dominates, and the stratosphere, in which radiative processes dominate. Comparisons with the observations of the Venus Orbiter infrared radiometer indicate that this tropopause region corresponds to the level of the tops of the visible clouds. The deepest inversions occur at latitudes between 60 and 70 deg, where a cold collar cloud feature was observed by the radiometer. The inversion disappears at latitudes lower than about 45 deg, and its magnitude decreases poleward of 70 deg, indicating a lowering of the tropopause region from a level of about 86 millibars at 70 deg to about 200 mbars at 87 deg.

The temperature structure of the middle and lower atmosphere was found to be remarkably similar for measurements taken at the same latitude, but independent

of the hemisphere, the time between measurements, or the solar illumination conditions. This indicates a symmetrical and very stable circulation pattern in the atmosphere of Venus.

S-band data from Pioneer orbits 9, 18, and 19 were used to study the vertical cloud structure in the north polar region. These occultation profiles represent three different regions of the north pole in terms of vertical temperature structure and proximity to the polar hot spots (regions of elevated temperatures) as seen by the 11.5-micrometer infrared radiometer aboard Pioneer. Dense cloud decks were revealed at the 1- to 5-bar level of the atmosphere. The cloud decks are lower in altitude and denser than those found in the equatorial region by the Mariner 10 radio occultation experiment and the Pioneer probes. These lower clouds appear to be fairly uniform in absorption properties throughout the polar region, with some suggestion of a deeper peak absorption near the polar hot spots.

Data from the 11.5- μ m channel of the JPL infrared radiometer aboard Pioneer Orbiter were combined with the occultation temperature data to interpret the upper cloud structure in the north polar region. Regions near the hot spots appear to have depressed upper cloud heights as well as increased optical density. These areas lack the temperature inversions characteristic of the north polar regions far from the hot spots. In addition, the cloud tops at the pole are about 100 mbars deeper in the atmosphere than at the equator.



The Pioneer Venus spacecraft has been orbiting Venus every 24 hours since December 4, 1978. As the spacecraft passes behind the planet, the radio signals (13.06 and 3.56 centimeters) are occulted twice: at entry into and at exit from occultation. Each occultation provides data for the analysis of the structure of the Venus atmosphere in terms of temperature, pressure, and absorption coefficient. These profiles are used to study the vertical cloud structure in the Venus atmosphere.

TERMINATOR AND NIGHTSIDE IONOSPHERE OF VENUS

Simultaneous reception of S- and X-band radio signals from the Pioneer Venus Orbiter was used at occultation to determine the vertical structure of electron density in the planet's ionosphere.

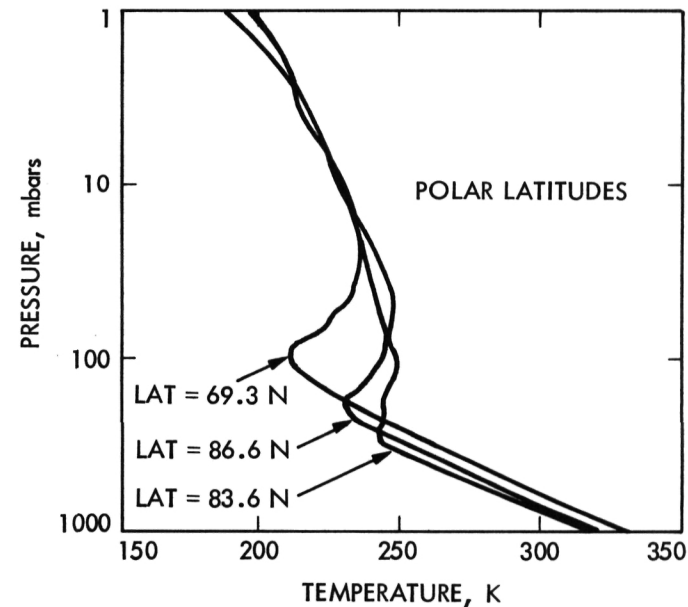
The geometry was favorable during the first occultation season for studying the ionosphere from near the terminator, across it, and almost to the anti-solar point.

Measurements near the terminator showed an orderly decrease of the peak density from about 164,000 electrons per cubic centimeter at a solar zenith angle of 87 degrees to about 30,000 electrons per cubic centimeter at 96 deg (6 deg beyond the terminator). As the site of measurement approaches the terminator, a region of almost constant electron density develops above the main peak, beginning at an altitude of about 250 kilometers and extending up to 500 km. The height of the ionosphere varied from about 300 to about 700 km and was apparently influenced by diurnal changes in the solar wind conditions. The structure of the profiles above the main peak, showing a transition in scale height at about 170 km, is consistent with models in which the O_2^+ ion is dominant at the main peak (about 140 km), but O^+ becomes the principal ion at higher altitudes.

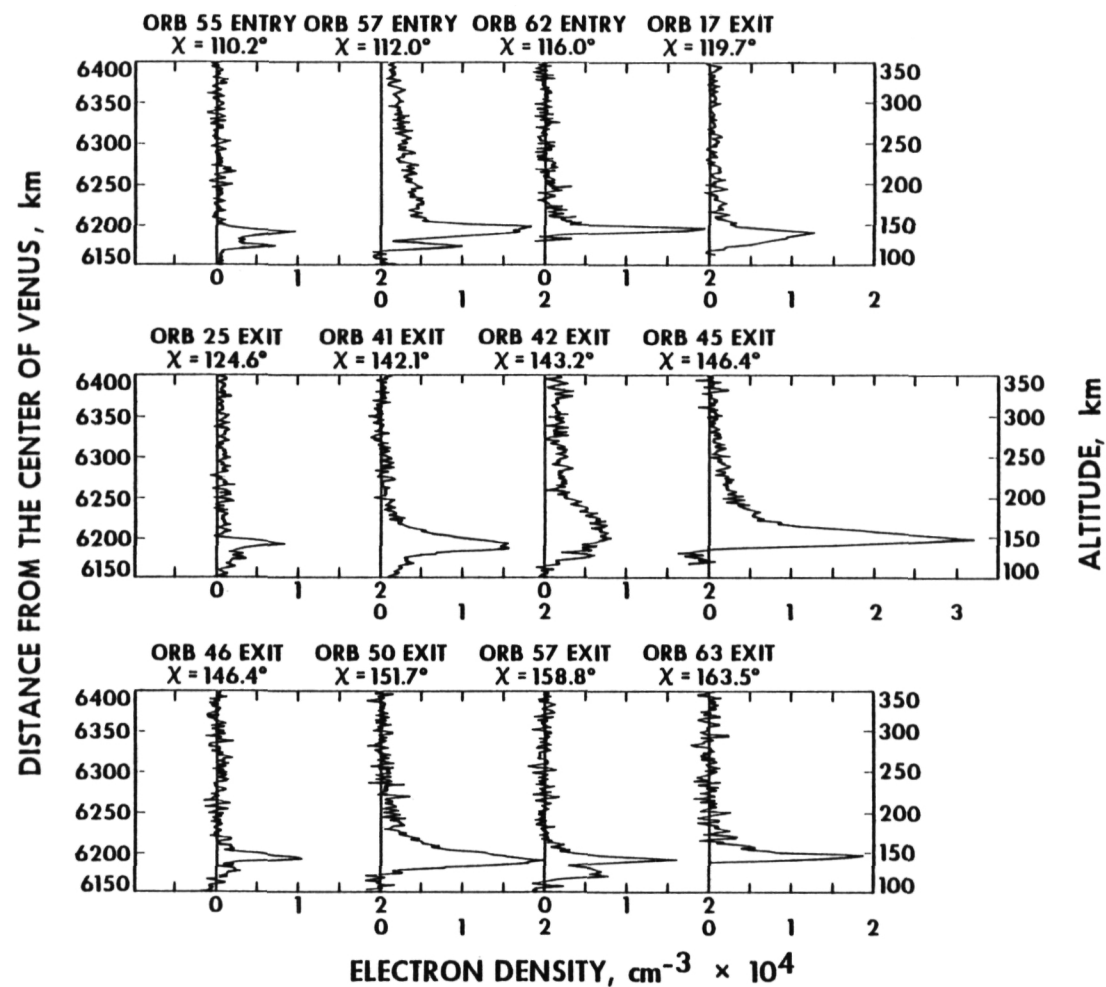
Beyond a solar zenith angle of about 110 deg, the "deep" nightside ionosphere begins, and no further effect of the distance from the terminator is observed. The structure and magnitude of the electron density are highly variable and show no correlation with measurements taken 24 hours earlier or later. The mean main peak electron density is $16,700 \pm 7200$ (standard deviation) electrons per cubic centimeter. The altitude of the main ionization peak, which is always observed, remains fairly constant

at 142.2 ± 4.1 km, virtually identical to the mean peak altitude on the dayside.

The two principal mechanisms that have been mentioned in connection with explaining how the nightside ionosphere is maintained through the long Venusian night are: (1) horizontal transport of major ions, mostly O^+ and O_2^+ , from the upper regions of the dayside ionosphere, followed by downward diffusion; and (2) direct impact ionization by precipitating electrons or protons. It has been suggested that the former mechanism could be responsible for the extremely variable, tenuous ionization above the peak, but that the main peak is formed by the latter mechanism.



Superimposed temperature-pressure characteristics of the Venus circumpolar atmosphere showing the decrease of the tropopause inversion magnitude and the lowering of the tropopause level from 70 degrees latitude to the polar regions.



Selected electron density profiles from nightside measurements of Venus. Both the magnitude and structure of the main peak are highly variable, possibly indicating the variability of the participating electron flux that defines the main peak ionization magnitude, and the energy distribution, which defines the vertical structure.

913

SOLAR WIND LATITUDE VARIATIONS

Analysis of the Mariner 10 Lyman-alpha data has made possible the first determination of variations in the solar wind flux out of the ecliptic. Previously, velocity measures have been made of the "solar wind" in the out-of-the-ecliptic region by ground-based observations of interplanetary scintillations from high latitude radio sources and by studies of comet tail orientations from high latitude comets. But the new JPL analysis has produced the first flux measurements at high latitude.

The new study is considered important in the planning of the forthcoming International Solar Polar Mission that is designed to ascertain in detail the solar wind properties out of the ecliptic. This information will be added to the well-known solar wind ecliptic properties as measured by planetary probes.

As it approaches the sun, the interstellar neutral hydrogen flowing into the solar system, known as the "interstellar wind," is ionized, largely from charge exchange reactions with solar wind protons. The reactions decrease the amount of Lyman-alpha radiation from the neutral hydrogen, excited by Lyman-alpha radiation from the sun.

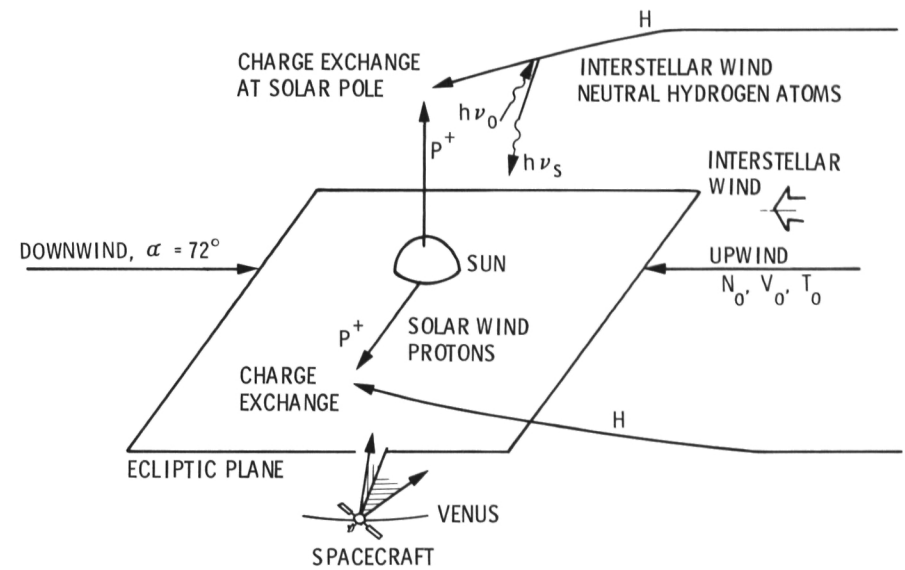
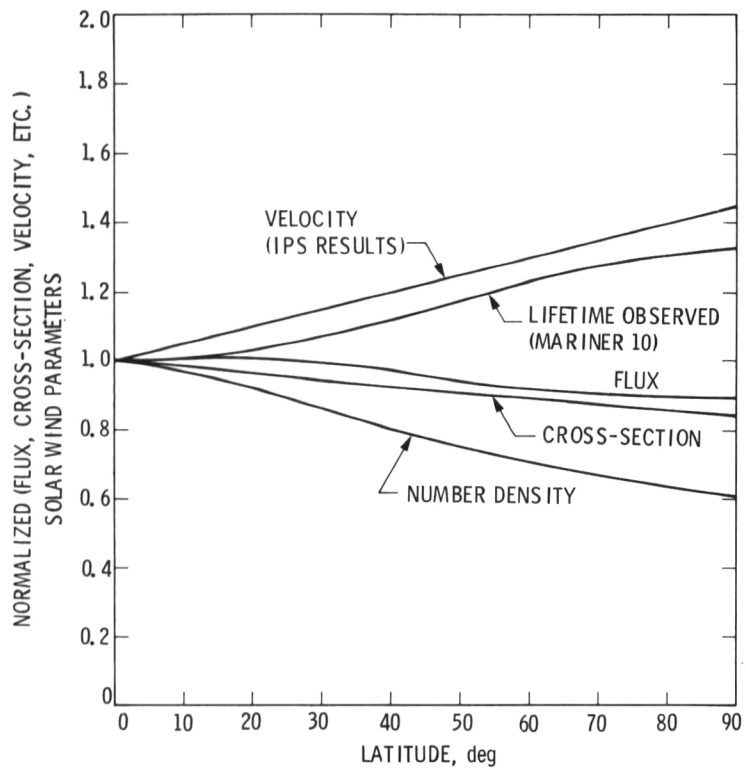
The Mariner 10 Lyman-alpha measurements show an enhancement of the backscattered radiation from those lines of sight nearest the solar poles. From this it

can be deduced that at higher solar latitudes the loss of neutral hydrogen from ionization by solar wind protons is less than at lower latitudes.

The Lyman-alpha data made it possible to determine quantitatively the latitudinal dependence of the charge exchange rate of solar wind protons with neutral hydrogen. It was found that the mean charge exchange rate decreases with latitude by 33 percent between the solar equator and the poles. This corresponds to an increase of the neutral hydrogen ionization lifetime of 25 percent.

The latitude variation of hydrogen lifetime can be coupled with the interplanetary scintillation measurements (which show that the solar wind speed increases with latitude) to determine the average solar wind mass flux variation and density variation as a function of latitude. The results imply that the solar wind flux decreases at the solar pole to about 85 percent of its equatorial value.

The study emphasizes the importance of the out-of-the-ecliptic mission to measure the effects of the solar cycle on the high latitude flux and on other important solar wind parameters such as magnetic field strength and solar activity center locations. The latter parameter is important in determining whether a polar variation of solar wind fields is induced by high latitude solar activity centers.



The graph (left) shows the results of the Mariner 10 interplanetary Lyman-alpha observations of latitude variations in the solar wind. The drawing outlines the geometry for the interplanetary Lyman-alpha observations and indicates how protons from the sun interact with neutral hydrogen from the interstellar wind.

D14

SOLAR IRRADIANCE STUDIES ON THE SOLAR MAXIMUM MISSION

The Active Cavity Radiometer Irradiance Monitor (ACRIM) experiment was launched on the NASA Solar Maximum Mission spacecraft in February 1980 to make regular observations of the solar total irradiance. The principal goals of the experiment are: (1) to begin a climatological data base on solar irradiance variability to be extended over at least one solar magnetic cycle (about 22 years) with ± 0.1 percent long-term precision, and (2) to provide a shorter-term data base (minutes to months) with maximum precision for studying aspects of solar variability significant to solar physics investigations.

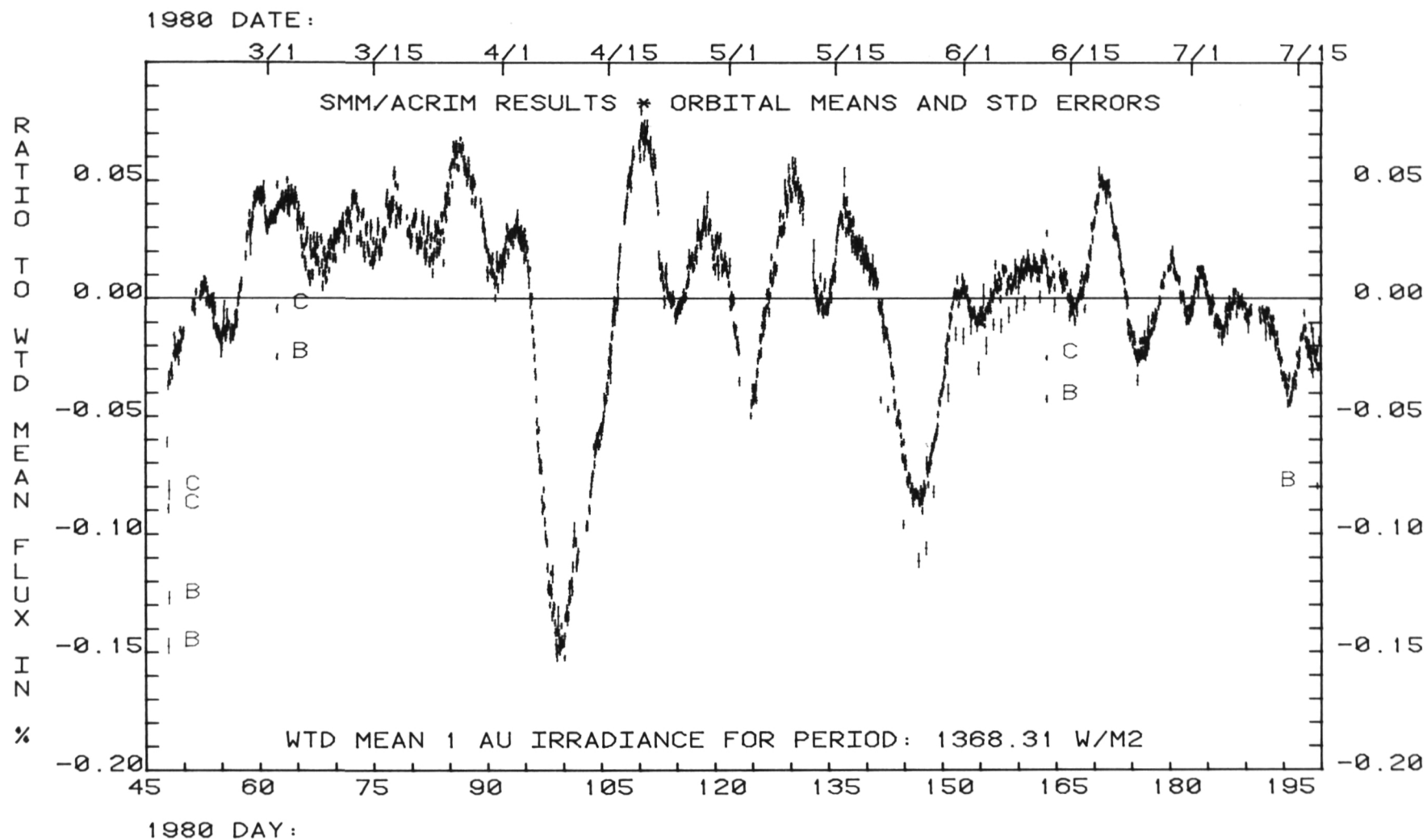
The first high-precision spacecraft measurements of solar irradiance by ACRIM show that this varied throughout the first 153 days of operation. Fluctua-

tions about the mean 1-astronomical unit irradiance of 1368.31 watts per square meter approached ± 0.05 percent.

Two large irradiance events were observed, however, in which the total flux changed by up to 0.2 percent over a 7- to 10-day period. These large decreases in irradiance were linked to specific sunspot groups in early April and late May 1980. The ACRIM detection represents the first direct evidence of large-scale energy storage within the solar convection zone in solar active regions.

Another feature of the ACRIM record was the seeming continuous variability at smaller amplitudes. Thus far, frequencies corresponding to cycles of less than 7 days appear to be absent. This appears to be consistent with sunspot activity, which usually takes more than 7 days to evolve fully.

Figure (opposite page): The 1 AU total solar irradiance for the ACRIM channel A sensor is shown as a percentage variation about the weighted mean for the first 153 days of the Solar Maximum Mission. The individual tick marks represent the mean irradiance for the sunlit portion of one orbit. The vertical bars through each tick mark are the ($\pm 1\sigma$) standard errors of the orbital means. The tick marks with associated "B" and "C" designations are the channel B and C measurements during comparisons with channel A.



15

HIGH-RESOLUTION GAMMA RAY SPECTROSCOPY EXPERIMENT ON HEAO 3

Existence of a 0.511-MeV electron-positron annihilation line from the galactic center region has been confirmed by the JPL high-resolution gamma ray spectrometer aboard the Third High-Energy Astronomy Observatory (HEAO 3). The instrument, whose prime objective was to perform an all-sky survey of gamma ray line emissions in the 0.045- to 10-MeV energy range, produced other significant results in 8-1/2 months until the prime sensor's life ended prematurely with depletion of the cryogen required to cool its germanium detectors. However, all scientific objectives were achieved and the cesium iodide shield detectors continue to detect gamma ray bursts and solar flares.

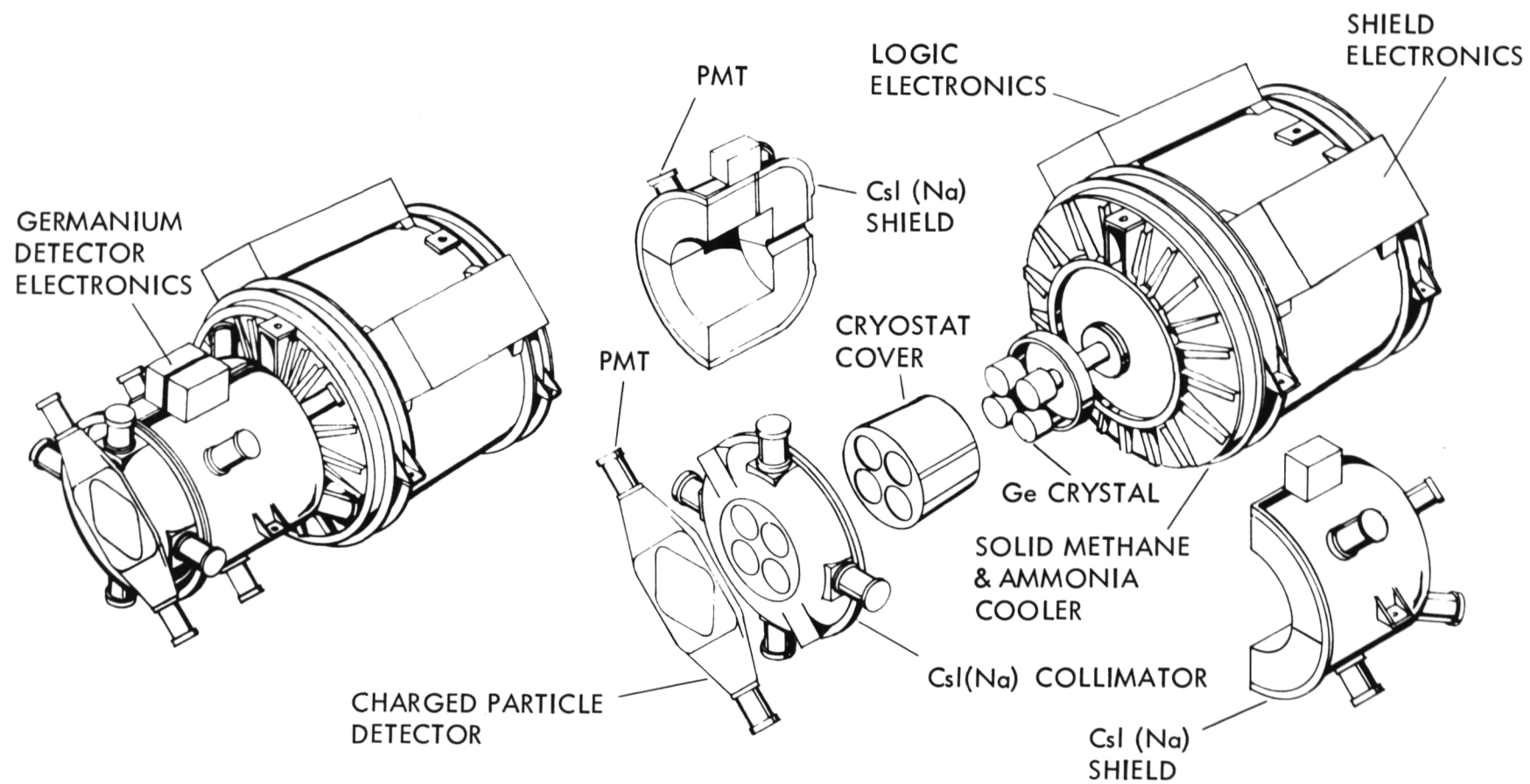
The HEAO 3 scanning mission allowed the instrument (employing a 30-degree field of view) to cover the entire celestial sphere within 6 months of launch into Earth orbit on September 20, 1979.

During the first 8 months of the mission, the spacecraft was maneuvered on two occasions -- for 2

weeks in the fall of 1979 and 18 days in the spring of 1980 -- to scan the galactic plane. In addition to detecting the electron-positron annihilation line, the spectrometer detected the continuous gamma ray emissions from the Crab Nebula and Cygnus region. Numerous solar flares and one gamma ray burst were also observed. A flare on November 9, 1979, indicated a strong 2.2-MeV deuterium line. Although such a line had been measured by others using scintillation detectors, this was the first measurement of the feature with high spectral and temporal resolution. A gamma ray burst lasting about 18 seconds occurred on November 16, 1979. Preliminary results of the event show possible spectral structures, although the data are limited by counting rate statistics.

Overall results of the observations will lead to a better understanding of the processes of high-energy interactions occurring in various astrophysical environments in the universe.

Figure (opposite page): Components of the high resolution gamma ray spectrometer used aboard the HEAO 3 are shown. The spectrometer includes a cluster of four coaxial high purity germanium (Ge) detectors surrounded by pieces of cesium iodide (CsI) scintillator operating in active anticoincidence with the central detectors and defining a 30-degree field of view.



D16

NEW FREQUENCY STANDARD TEST FACILITY

JPL has developed a facility for measuring the performance of ultra-precise frequency standards to within 1 part in 10^{16} . This Interim Frequency Standard Test Facility (IFSTF), the only fully operational one of its kind in the United States, provides the extremely stable environment required for measuring this performance.

Future deep space missions will rely on frequency and timing standards which are stable to 1 part in 10^{16} over 10^3 to 10^5 seconds. This accuracy will lead to more precise or lower cost spacecraft navigation, increased knowledge of the characteristics of the interplanetary propagation medium, and an enhanced probability of detection of gravity waves.

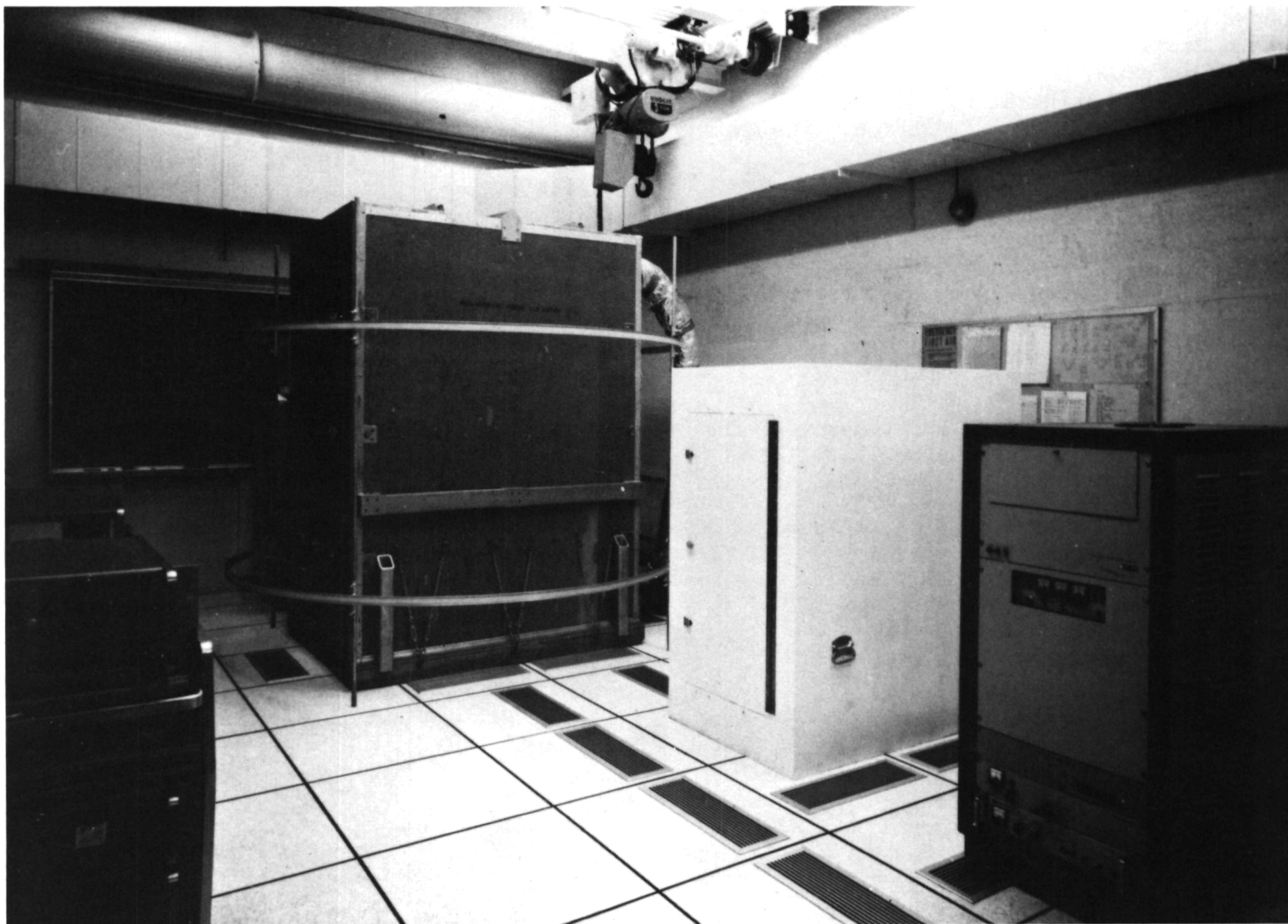
Frequency stability in the range of 1 part in 10^{13} to 10^{15} over 10^3 to 10^4 seconds is achievable from current state-of-the-art frequency standards. These stabilities can only be obtained by using atomic frequency standards, such as a hydrogen maser, coupled with sophisticated environmental control. These standards are still sensitive to small temperature changes, despite thermal control of critical internal components. Further, because of the extraordinary

stability aimed for, no instrumentation existed in the United States to measure the frequency and timing stability of these standards.

The new facility meets these needs. It contains two key features: extreme temperature control and ultra-stable instrumentation. Ambient temperature is controlled to within ± 0.05 degrees Celsius over 24 hours. Control to ± 0.01 degree Celsius is available within special test chambers. Temperature can also be varied as required over a 30 degree Celsius range. Instrumentation stable to 1 part in 10^{16} may be used to evaluate up to 12 frequency standards simultaneously. Two reference hydrogen maser standards are maintained within the facility as references.

Stability curves have been measured showing the variance of measured frequency differences between two hydrogen masers, with and without the extreme temperature control of the facility, over the course of a day. Only with the temperature control can the 10^{15} level of stability be achieved at 10^4 seconds. A stability of 6 parts in 10^{16} at 3×10^3 seconds is the best achieved by any JPL hydrogen maser.

Figure (opposite page): Interior of the new Frequency Standard Test Facility, whose extraordinary temperature and magnetic field controls make it possible to measure the frequency standard performance of hydrogen masers within one part in 10^{16} . The two wooden cabinets in the photograph contain hydrogen masers. One cabinet is encircled with coils that produce a magnetic field capable of changing the magnetic environment. Also shown are floor plenums for forced air.



917

IMPROVED HYDROGEN MASER PERFORMANCE

JPL has designed a better hydrogen maser, one with doubled reliability and greater frequency stability than current masers. Reliable and stable atomic frequency standards are critical to the precise navigation required for deep space exploration. The hydrogen maser provides the standards.

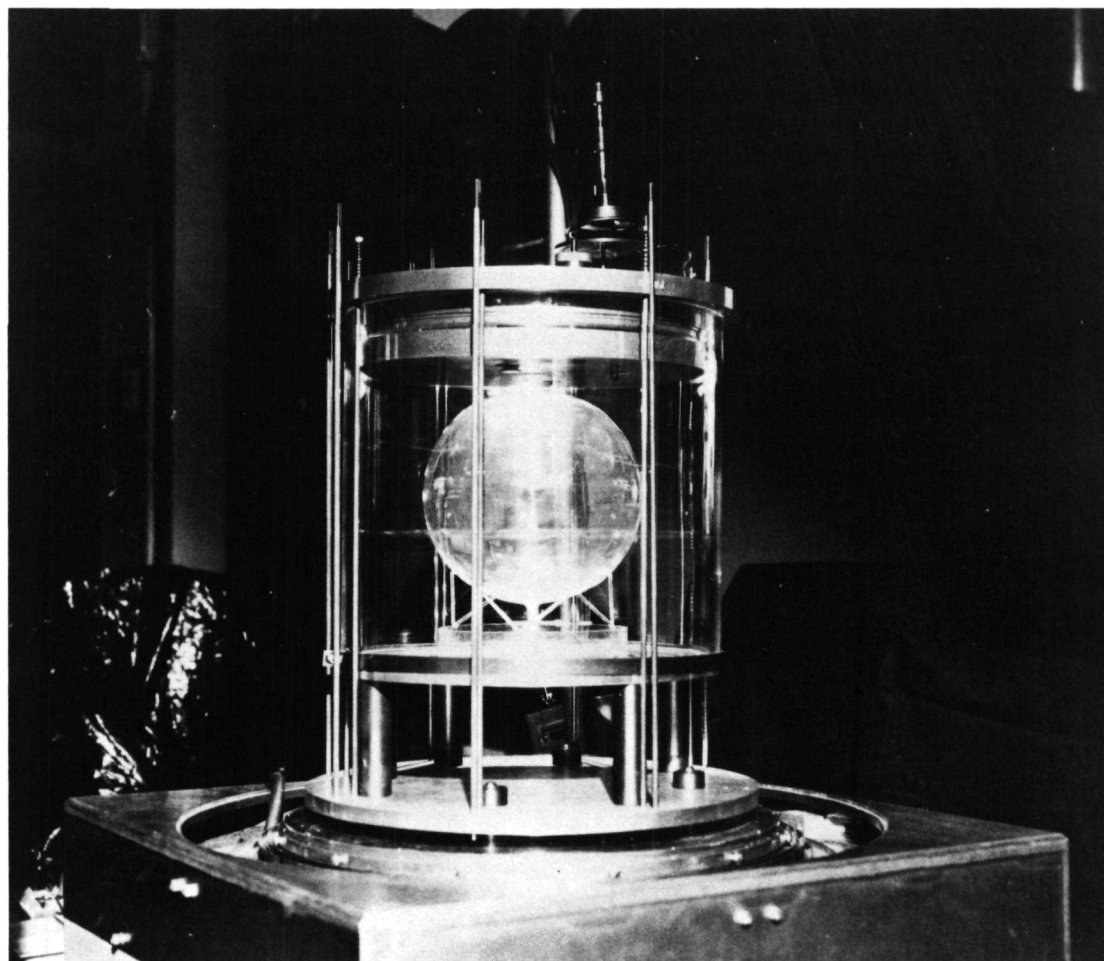
A hydrogen maser is an electronic oscillator which resonates at a frequency precisely determined by the natural properties of the hydrogen atom. In practice, hydrogen atoms are pumped into a storage bulb within a cavity, which they excite at a microwave frequency corresponding to the quantum electrical resonance of the atoms.

Doubled reliability resulted from improving the technique for coating the storage bulb. This improve-

ment doubled the oscillator Q (a measure of sharpness of resonance) to 1.6×10^9 , which permitted the rate of atomic hydrogen usage to be halved. This in turn doubled the expected lifetime of the internal vacuum pump, which feeds the hydrogen to the bulb. The pump is the current limiting factor in hydrogen maser reliability.

Greater stability is now possible because of better cavity and storage bulb mounting techniques. The mounts must have extreme mechanical and thermal stability to isolate the frequency of oscillation from external disturbances. The new three-point strut suspension for the cavity, for example, cuts thermal coupling by a factor of 3, with a corresponding increase in frequency stability.

Figure (opposite page): Hydrogen Maser Storage Bulb with improved bulb mounting is shown with the outside microwave cavity removed. The improved mounting provides greater thermal and mechanical isolation from outside disturbances.



718

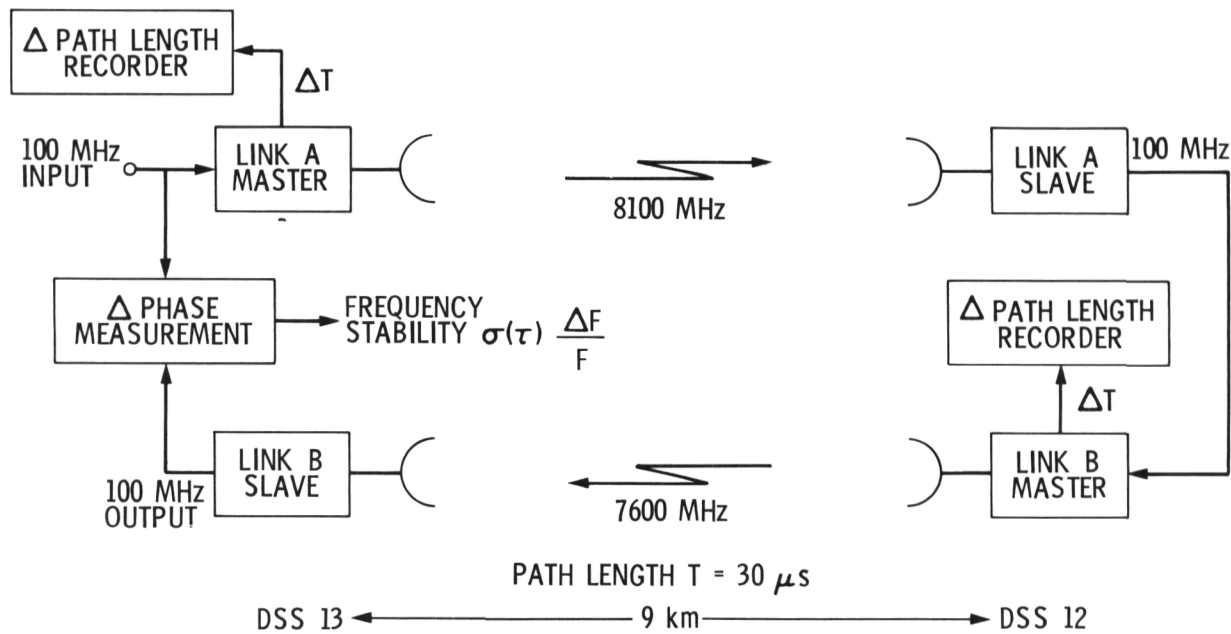
DISTRIBUTION OF STANDARD FREQUENCY SIGNALS BY MICROWAVE

JPL has completed a 9-kilometer microwave link between two deep space stations at the Goldstone complex, and demonstrated distribution of signals over the link that are stable in frequency to 1 part in 10^{15} over at least a 100-second interval. Usually, each deep space station must maintain its own frequency standard. Being able to distribute extremely stable signals between these stations means that only one set of standards needs to be maintained at each complex; all other stations can obtain their frequency and time standard signals by distribution. This represents a potentially large savings in network, complex, and station operation costs.

Frequency stability of 10^{15} or better at each station within a complex is needed for next-generation

navigation systems, increased probability of gravity wave detection, and greater knowledge of the characteristics of the interplanetary propagation medium.

Most microwave links cause dramatic reduction of frequency stability over even modest distances. The 9-km link operated in conventional fashion would yield no better than a stability of 2 parts in 10^{13} . That is, variations in link path caused by electronic parts, microwave towers jostled by wind, and atmospheric effects could cause a perfectly stable signal to be received with the poorer stability. The fifty-fold improvement in stability was achieved over the link's length by utilizing a two-way stabilization technique.



Test setup of the microwave link between the Venus and Echo sites at Goldstone for distributing frequency and time standards signals. This technique provides a more stable distribution than has been possible before.

D19

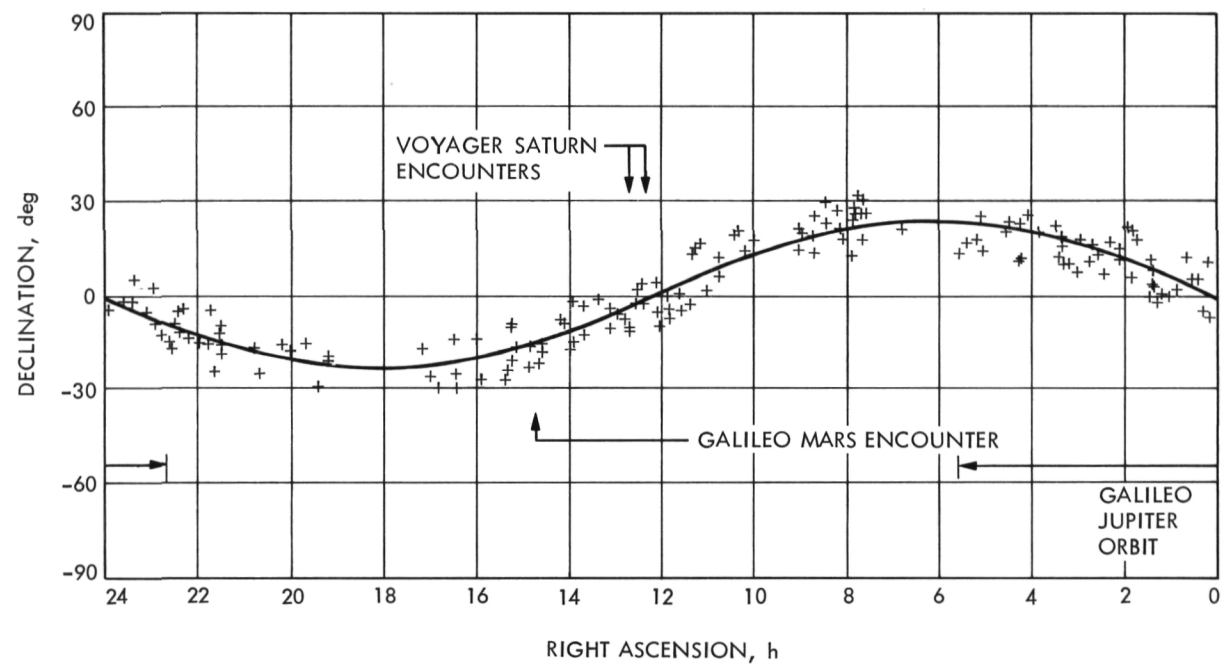
RADIO SOURCE CATALOGS

To support its missions in geodesy and spacecraft navigation, JPL has developed several radio astrometric catalogs. One catalog consists of 170 quasar locations, all lying within a few degrees of the ecliptic plane, the plane in which most of our solar system lies. These radio sources all emit energy greater than 0.1 Jansky at S-band microwave frequencies. The positions of these sources are being determined to an accuracy of 0.01 arc seconds.

Catalogs such as this are one of the keys to a new form of spacecraft navigation, differential very long baseline interferometry (delta VLBI). The technique of cross-correlating signals received at deep space stations separated by intercontinental distances

yields spacecraft angular position with respect to these catalogued quasars. This catalog of ecliptic quasars is for use by Voyager during encounter with Saturn. It is also intended for use by Galileo, both at Mars encounter and during insertion into Jovian orbit.

Another of the catalogs consists of 109 radio sources uniformly distributed over the entire sky. The relative positions of these sources are known to an accuracy of at least 0.01 arc second. This catalog, believed superior to any other radio catalog of its kind in the world, lists objects at the very edges of the visible universe.



This plot describes the locations of 170 catalogued quasars near the ecliptic plane. Their precise locations are for use in the navigation of the Voyager spacecraft at their encounters with Saturn and for Galileo at both Mars and Jupiter.

Page intentionally left blank

II. Energy and Energy Conversion Technology

COAL PUMP DEVELOPMENT

The JPL Coal Pump Development Project for the Department of Energy (DOE) successfully demonstrated plasticating coal pumps ranging in capacity from 25 to 450 pounds per hour. JPL engineers used 11 types of coal, mostly from the eastern United States bituminous fields, in the tests.

The coal was heated to about 400 degrees Celsius in a plasticating screw extruder where it became soft, was pumped to pressure, and was injected directly into a coal conversion reactor. The application of such a coal pump to a hydrogasification process could reduce product cost by about 7

percent in DOE's projected synthetic fuels program.

The rheological properties and solid friction coefficients of various types of coal and their extrudants were categorized in pump runs of up to 34 hours. Theoretical models of the plasticating pump have been developed, aimed at building commercial scale pumps capable of handling 30 to 40 tons of coal per hour.

Techniques for creating a continuous stream of sprayed coal also were developed. In some preliminary batch extrusion tests, coal sprays as fine as 99 percent less than 22 micrometers have been obtained.

Figure (opposite page): A 1.5-inch coal pump (a modified Davis-Standard screw extruder) is shown in a configuration for continuous plastication and generation of a fine spray from coal.



D21

SUPERCRITICAL FLUID EXTRACTION OF COAL

In collaboration with the Caltech Chemical Engineering Department, JPL designed and built a coal batch high-pressure autoclave system for experimentation with supercritical fluid extraction processes. Gases heated above their critical temperatures and compressed to near-liquid densities are called supercritical fluids. These fluids have unusual solvent power capable of breaking down organic matter in coal at a relatively low temperature.

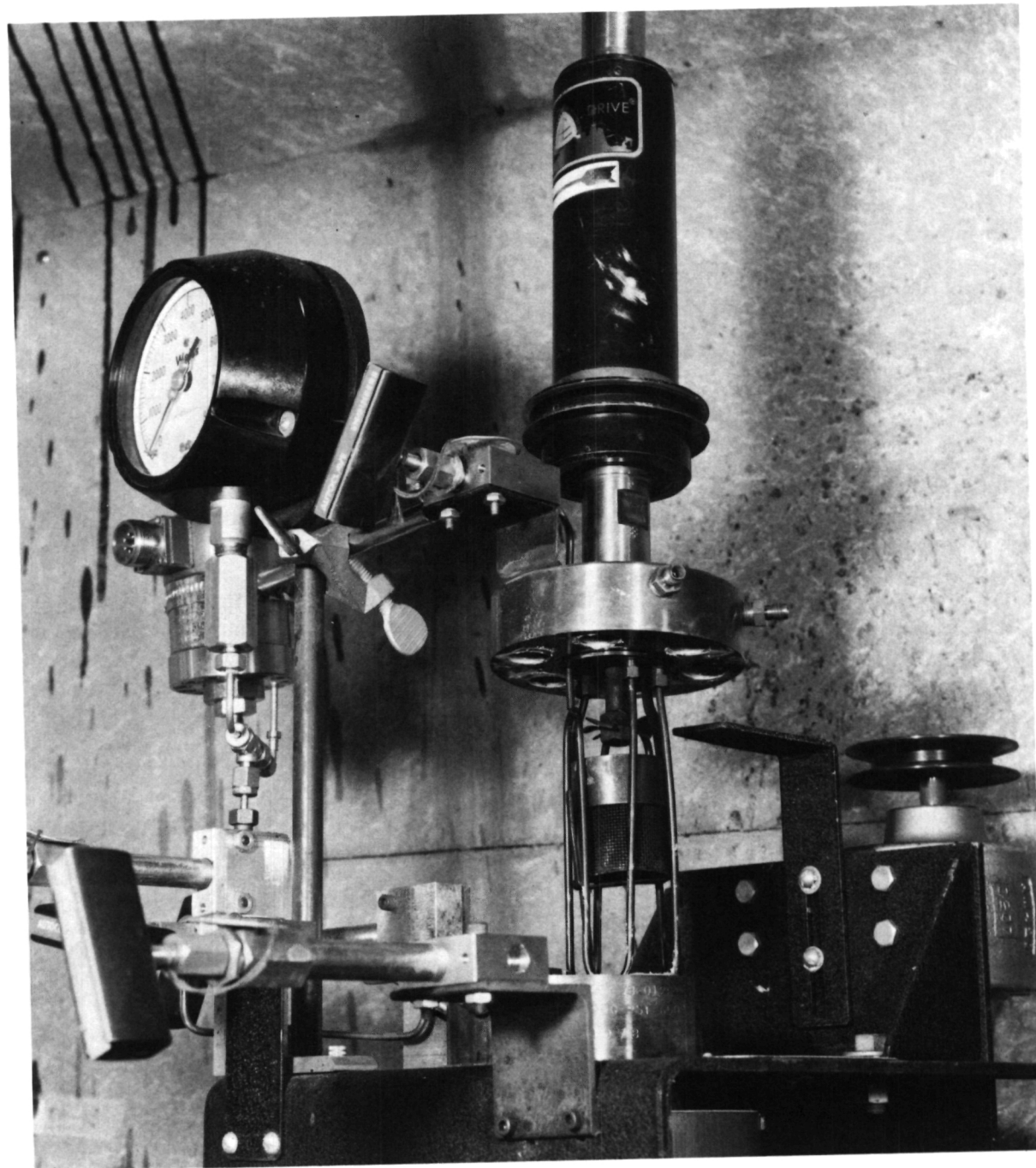
The testing of supercritical fluid extraction processes involved experiments with four types of solvents and three different coals -- two bituminous types and one western lignite. Up to 52 percent by weight of coal (moisture-free) was extracted from one bituminous coal using a unique mixture of two aromatic solvents, phenanthrene and toluene, at 380 degrees Celsius and 61 atmospheres of pressure. The mixture was

also effective on the two other coals. The dual-solvent system appears to enhance the extractability of organic matters. (Pure toluene being used alone in some pilot plants extracts only 20 percent by weight.)

Decreases in weight after extraction agreed well with increases in ash content in the residual char. Sulfur and trace metal contents of the coal extract also should be lower than those of raw coal. Besides phenanthrene, several other dissolution agents may be feasible, including an economical solvent containing anthracene oil.

The process, along with Caltech efforts on mass transfer effects and structural changes, holds promise as a viable alternative for coal liquefaction to meet national energy needs.

Figure (opposite page): This 300-cubic-centimeter high-pressure autoclave reactor system equipped with gas chromatography analysis capability was built at JPL for innovative investigation on supercritical fluid extraction of coals. The picture shows a coal basket (center of shaft), which is normally immersed in the supercritical fluid during the test operation, the pressure-sealed magnetic stirrer above it, solvent and product sampling ports, plus pressure monitoring and heating devices.



D2P

SOLAR THERMAL POWER CONVERSION

As a means of providing heat, electricity, or both from the sun, JPL is developing parabolic dish solar collector technology under the Department of Energy's Solar Thermal Power Systems Project. JPL responsibility for solar point-focusing technology extends from subsystem development through testing of prototype modules, culminating in field experiments that lead to commercial systems for generation of electricity, process heat, or both. An important facet of the work takes place at the JPL parabolic dish test site (PDTS).

Prototype thermal receivers and power converters are to be tested on two test bed concentrators, each 11 meters in diameter, at the PDTS located at JPL's Edwards Test Station in the Mojave desert. Each concentrator uses 224 reflecting mirrors to focus the sun's rays. Optical energy conversion to heat occurs in a receiver at the focal point of the dish, where working fluids can be heated to temperatures, as needed, from about 370 to 1560 degrees Celsius.

To assess the performance of the concentrators, both as to their reflectivity and the geometric accuracy of their construction, the shape and intensity of the beam at the focal plane must be measured. A flux mapper and a cold water calorimeter were developed at JPL to measure these performance parameters. To facilitate the flux-mapping task, an absolute cavity-

type radiometer was adapted to determine solar image intensity. These instruments are described below.

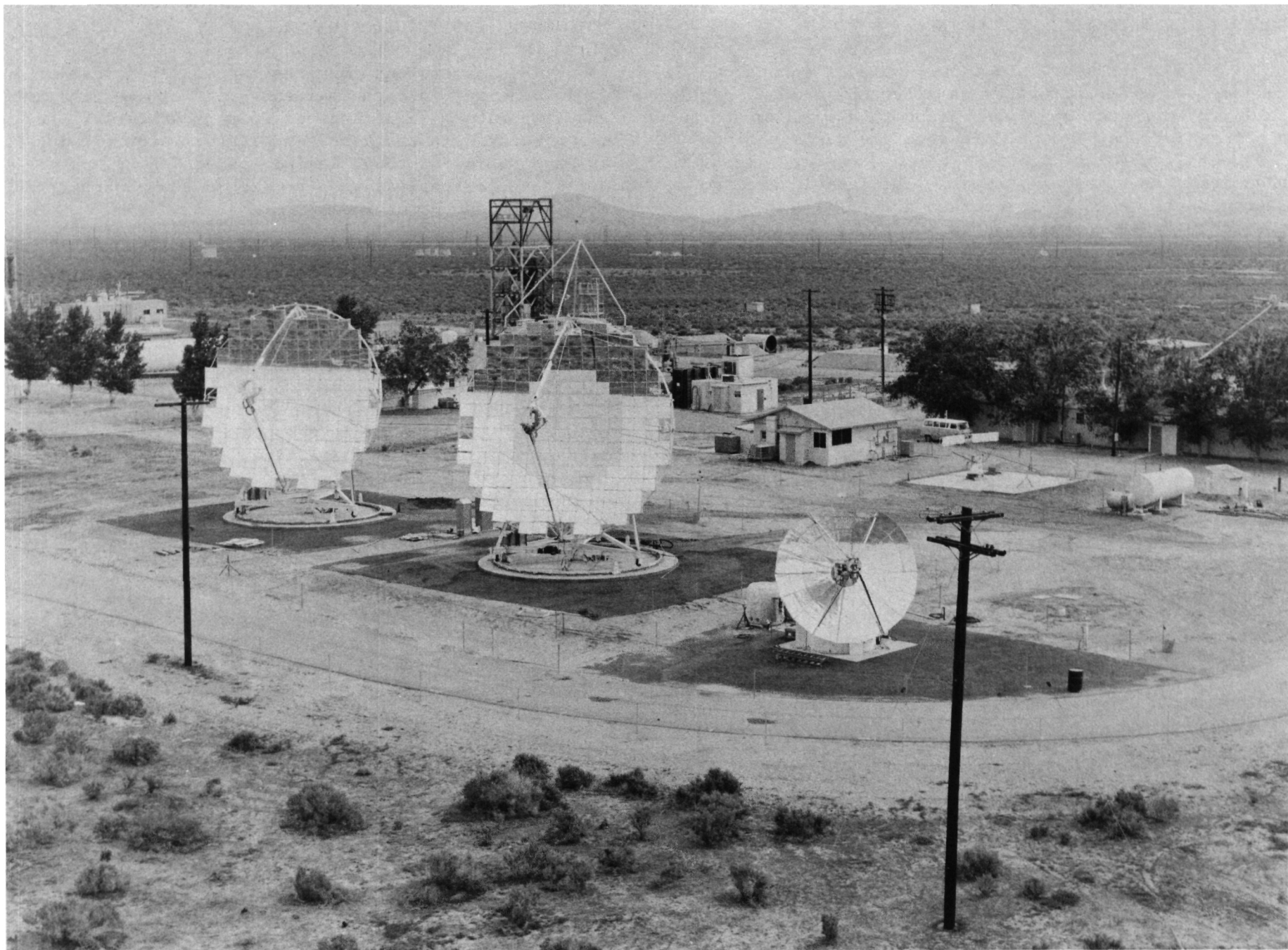
SOLAR CONCENTRATOR FLUX MAPPER

This instrument was designed for three-dimensional mapping of the intensity distribution of highly concentrated solar energy near the focus of an optical concentrator. Data obtained can be displayed as contour maps, digital arrays, and isometric visualization. The mapper is capable of measuring intensities up to 15,000 solar constants, using various radiometer probes which can be selected to provide the desired trade-off between speed of scanning and accuracy of measurement. (Solar constant is the quantity of radiant solar heat received normally at the outer layer of the Earth's atmosphere.)

The flux-mapping system consists of a radiometer sensor probe, a mechanism which moves this probe along three axes, electronics for recording electrical signals, and a microprocessor for controlling the probe. A photodiode probe is available for high-speed scanning of one inch per second, and is accurate to within 5 percent of the true value. With the JPL-designed cavity radiometer, a much slower scan is required but a measurement accuracy to within 1 percent can be achieved.

The flux mapper has successfully delineated flux patterns of both test bed concentrators and a third collector at the Edwards Test Station.

Figure (opposite page): The two 11-meter test bed concentrators, along with a 6-meter dish, are shown at the JPL parabolic dish test site at Edwards Test Station, where technology is being developed for DOE's Solar Thermal Power Systems Project.



D23

SOLAR IMAGE INTENSITY RADIOMETER

This instrument is a water-cooled absolute cavity radiometer. The radiometer is silver plated and highly polished to reduce heat absorption to a minimum (to only 5 percent of what it would be were the surface black). The overall absolute accuracy of measurement made by the radiometer is within 1 percent. The individual items that contribute to this accuracy are: (1) area of aperture (0.0158 cm^2) known to about 0.5 percent; (2) electric calibrating power known to about 0.1 percent; and (3) blackness of conical cavity (0.996) known to about 0.2 percent.

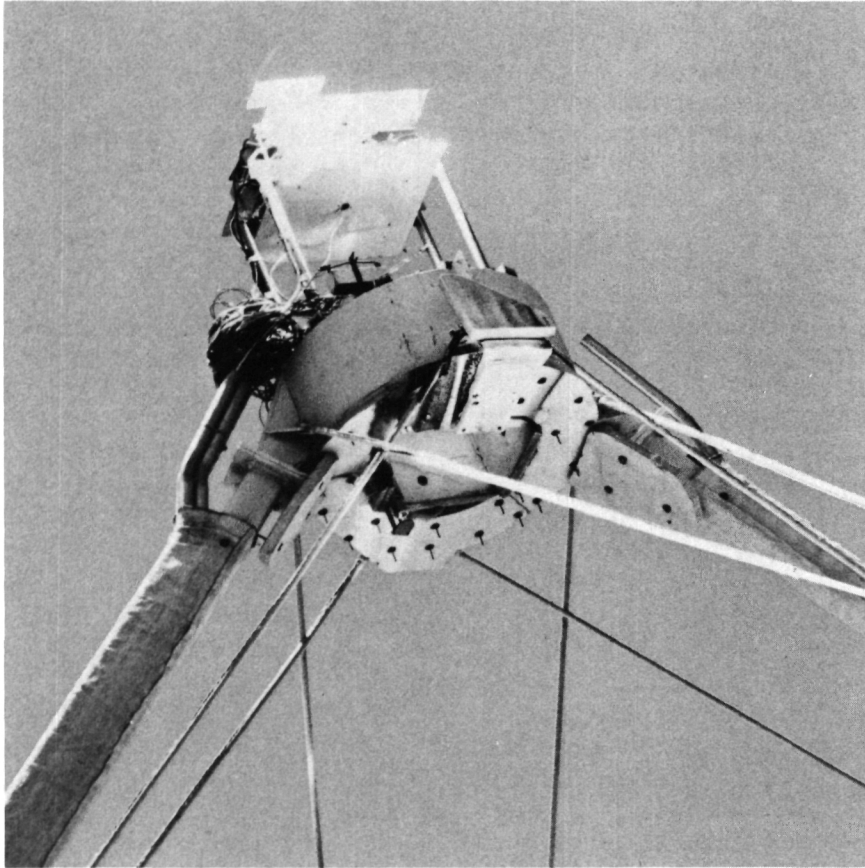
Cooling water needed is about one gallon per minute, which flow rate gives a temperature rise of about 15 degrees Celsius. The acceptance angle is 55 degrees, which is characteristic of most concentrators. The time required for a single point measurement is only 4 seconds even for large changes in irradiance from point to point. It was used to measure the maximum intensity of the solar image at the focus of the test bed collector, which reached approximately 14,000 solar constants with all collector mirrors uncovered.

D24

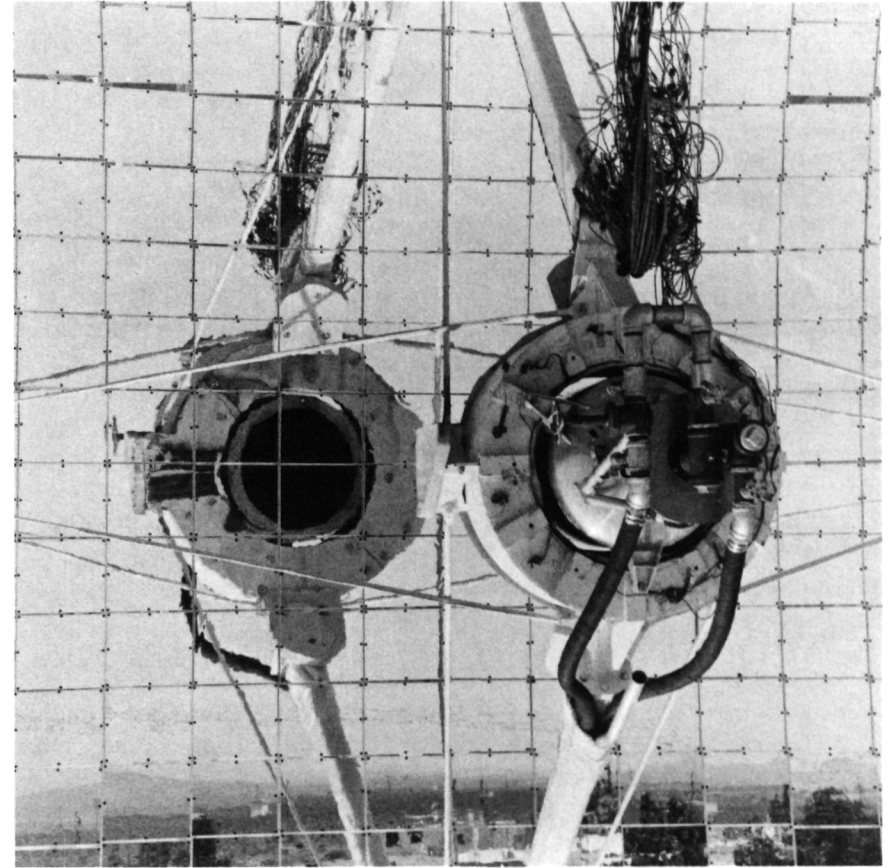
COLD WATER CAVITY CALORIMETER

This instrument converts concentrated insolation (solar energy) into thermal energy at or near the ambient temperature -- 38 degrees Celsius or less. The calorimeter uses the heat capacity of water flowing at up to 50 gpm through coiled copper tubing and measures the temperature rise due to the energy from the solar concentrator dish.

At ambient temperatures thermal losses are minimal. During calibration, for example, the device measured within 2.5 percent of the known power input. The calorimeter is designed to accommodate a nominal 90-kilowatt capacity concentrator which, at a 50-gpm flow rate, yields a fluid temperature rise of 6.82 degrees Celsius. The instrument uses apertures varying from 4 to 10 inches. With these, a correlation of energy concentration (in kilowatts) to aperture size is made to determine the thermal/optical efficiency of the concentrator.



Closeup of the Solar Concentrator Flux Mapper mounted at apex of test bed concentrator. The Solar Image Intensity Radiometer fits in top center of the flux mapper.



The Cold Water Cavity Calorimeter shown here monitors the temperatures on the concentrators.

225
EXTREMELY LOW ENERGY ELECTRON STUDIES OF GASES USED AS HIGH-VOLTAGE INSULATORS

The search for more efficient methods of transporting electrical energy has steadily increased line voltages at which power must be transmitted. Projected transmission line voltages are now in the range of 1 to 1.5 megavolts. This increase is necessitating the development of better gaseous insulators for use in underground transmission lines, circuit breakers, and switch gear.

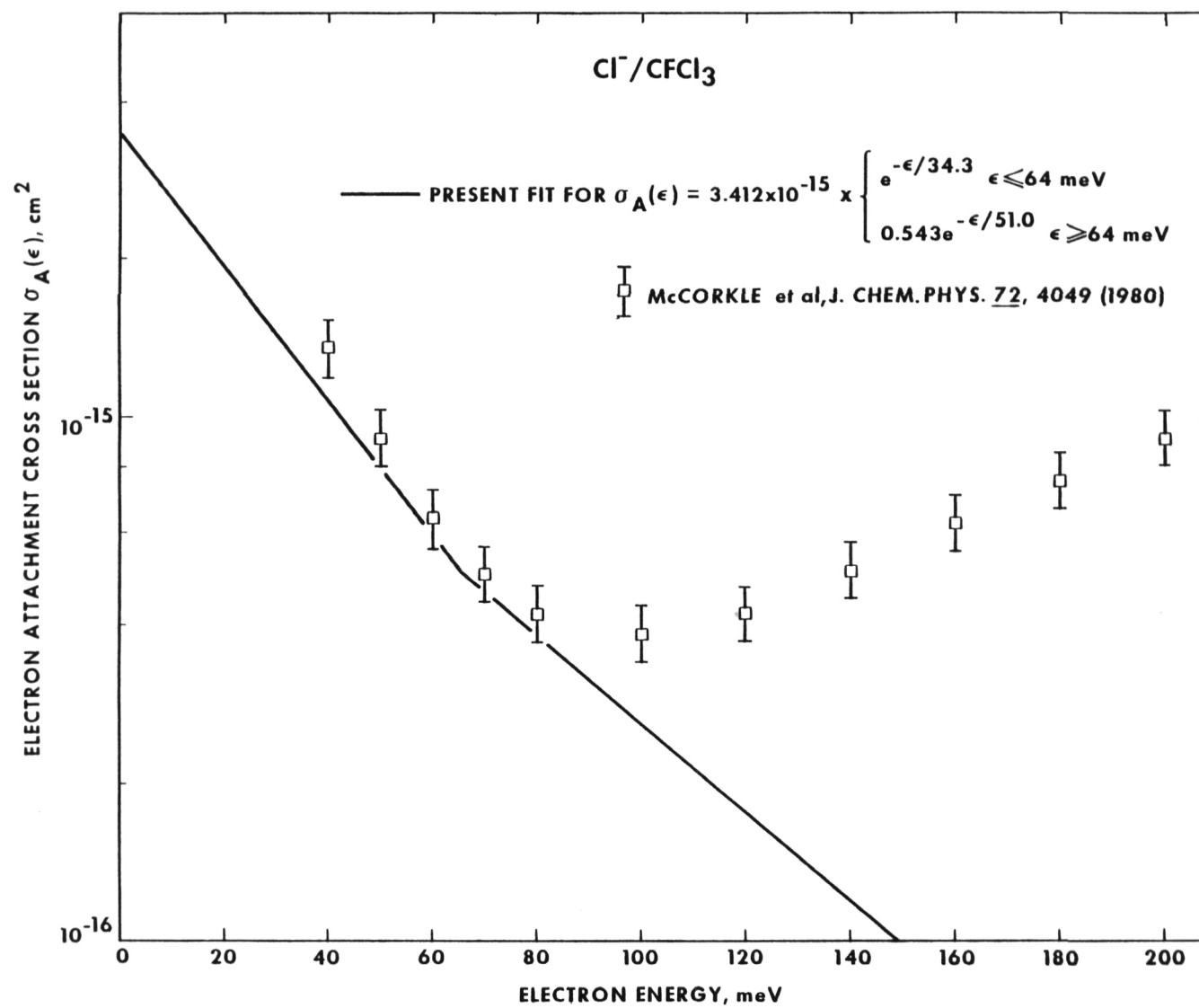
Studies are under way in several laboratories to "custom design" a unitary or multicomponent gas mixture to a particular line voltage, electrode geometry, or operating pressure. Such studies require knowledge of the basic physics and chemistry of each gas and, then, of the mixture. This basic understanding entails knowledge of thermal ("zero energy") attachment cross sections, positions and cross sections of non-thermal negative-ion resonances, and electron-scattering and ionization cross sections.

Using the technique of Threshold Photoelectron Spectroscopy by Electron Attachment (TPSA) developed at JPL, researchers were able, for the first time, to measure absolute electron attachment cross sections in sulfur hexafluoride (SF_6), a gas traditionally used as a dielectric insulator, and in trichlorofluoromethane (CFCl_3), a new candidate for such purposes. In a high-voltage environment, the object is to convert as many free electrons to molecular negative ions as possible. By using attachment cross sections, researchers described the process by which a fast electron is converted to a slow ion. This attachment also inhibits

the development of coronal activity and a breakdown in the ambient gas.

In the TPSA technique, a mixture of xenon gas and SF_6 is photoionized by monochromatic light from a vacuum ultraviolet light source. Electrons having a narrow band of energies (7 meV wide) and of very low energy epsilon (variable in the range 0-200 meV) are generated in situ in a field-free region via the xenon photoionization. These electrons then attach to the SF_6 to form SF_6^- . Detection of the mass-analyzed SF_6^- current versus photoionization wavelength gives the relative electron attachment cross section for the attachment process.

The figure opposite shows a comparison of the two approaches for the electron attachment process $\text{Cl}^-/\text{CFCl}_3$; i.e., that in which a thermal electron attaches to CFCl_3 to yield a Cl^- (negative chlorine) ion and a CFCl_2 (dichlorofluoromethane) radical. The excellent agreement at electron energies below 100 meV of the TPSA technique with previous measurements indicates that (a) the integrated rate coefficient and the swarm-measured $\sigma_A(\epsilon)$ are consistent with one another, and (b) the TPSA-measured lineshape is the correct shape for describing the attachment process down to electron energies of zero meV, where measurements by any other technique are not possible. In fact, by this very simple approach JPL lays claim to the world's indoor record for experiments done at the lowest electron energy and at very high electron resolution! The difference in the figure between the solid line and experiment points at $\epsilon \geq 100$ meV arises from extra negative-ion signal in the swarm data that was purposely excluded from the TPSA data.



Comparison of the present TPSA cross section as calibrated to the integrated rate coefficient, with swarm cross sections. This result represents the consistency of the TPSA technique with two very different sets of experimental measurements.

36

ELECTRIC POWER SYSTEMS SIMULATOR

JPL's Utility Systems Program is designed to help integrate energy sources into the nation's electric utilities and to examine related future changes in utility system design and operations.

One recent development of the program is the JPL-designed Electric Power Systems Simulator, a miniature computerized representation of a utility system complex in simplified form. The simulator portrays graphically a 24-hour cycle of utility system operation and shows the effects on the system of new alternative energy sources, such as solar and wind-driven generators. The simulator visualizes operational problems that can arise when power loads or generation fluctuate. It also provides an overall system operations view to assess whether to use individual alternative sources, or various mixes of power generation and storage.

Any kind of a utility day -- actual or hypothetical -- can be portrayed by the simulator. The season can be selected, as can the geographic location. As an educational tool, the unit can be programmed for

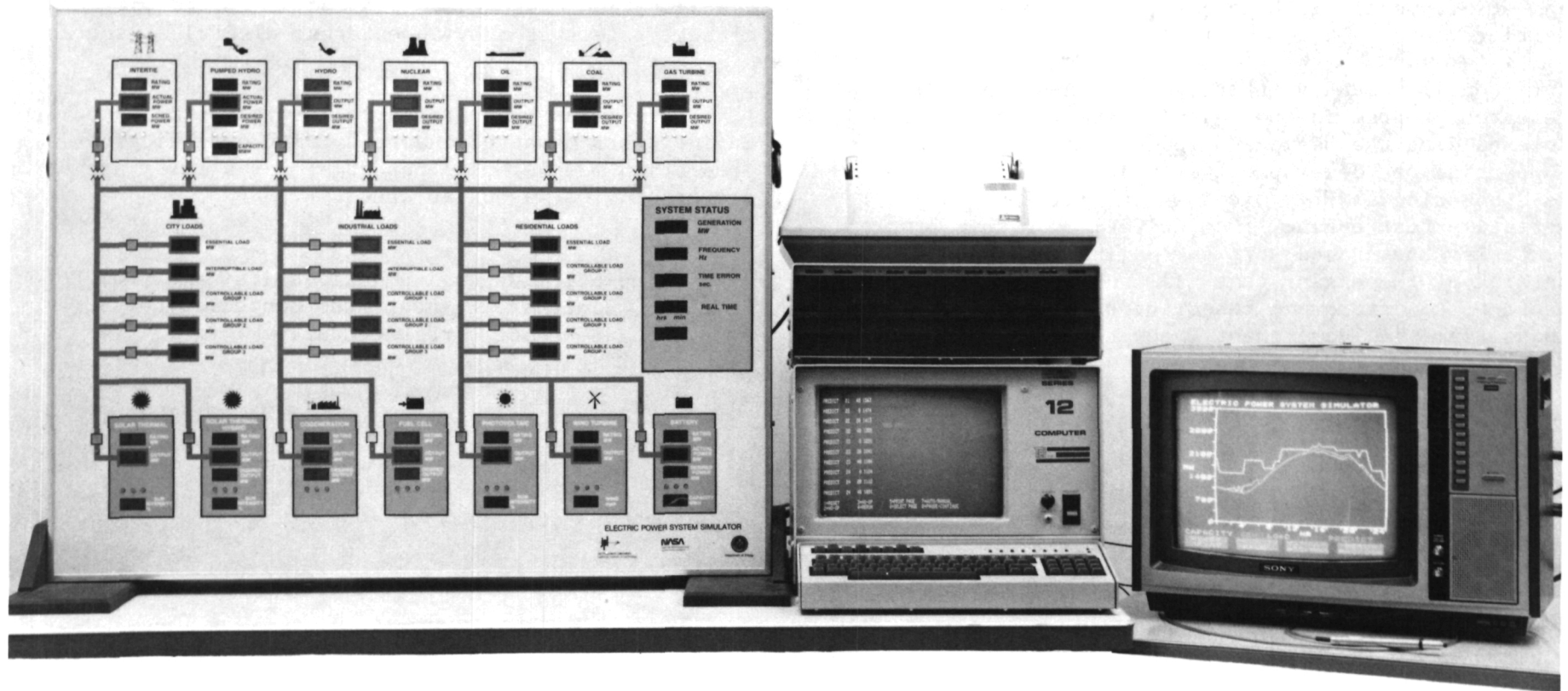
varying degrees of operator interaction. For example, given a load curve, it will generate a partial response, leaving some decisions to the operator.

A portable tabletop device, the simulator hardware comprises a micro-processor-driven display, a black-and-white video monitor with keyboard input to the microprocessor, and a color video monitor for display of predicted and actual load curves and power generation.

Completed early in 1980, the simulator has been demonstrated in the United States and Canada. It has proven useful in helping government and business leaders appreciate the complexity of present utility operations and anticipate the potential problems arising from alternative energy sources in the future. Capabilities of the simulator will be expanded as future utility requirements are identified and analyzed.

The Electric Power Systems Simulator was developed for the Department of Energy's Electric Energy Systems Program and the NASA Energy Systems Division.

Figure (opposite page): The JPL Electric Power Systems Simulator is a tripartite table-top device including (left to right): a microprocessor-driven display, the video monitor with keyboard input to the microprocessor, and the color video monitor which displays predicted and actual load curves and power generation.



D21

STIRLING LABORATORY RESEARCH ENGINES

The Stirling engine has high thermal efficiency, low noise and vibration levels, low emissions, multi-fuel capability, and application ranging from solar electricity generation to automotive propulsion. The problems with current commercial developments include difficult gas sealing, material challenges, complex analytical modeling, high cost, and proprietary barriers.

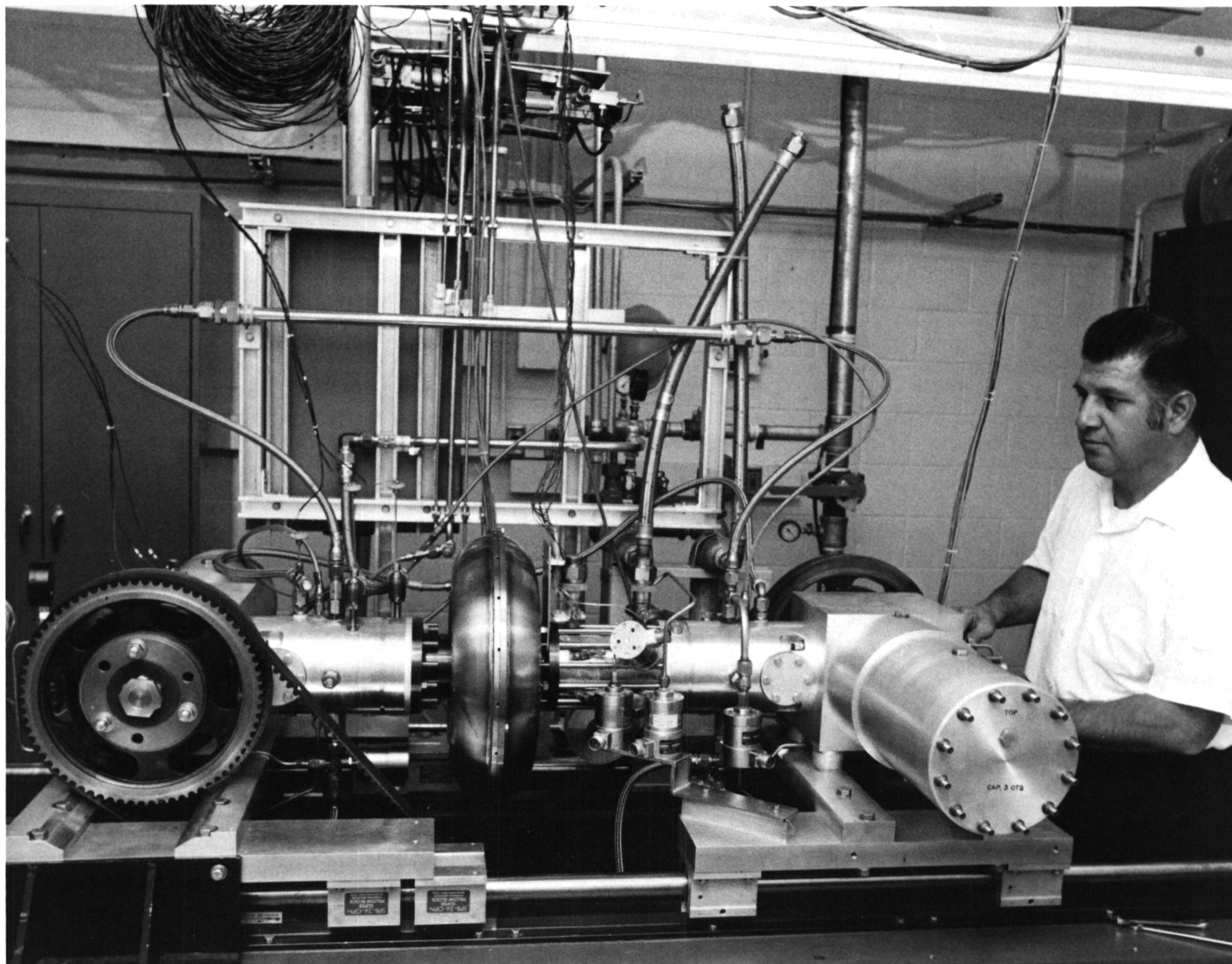
Until recently, there was no on-going basic research program in the United States. As one step in expanding the basic knowledge relative to and supporting the development of Stirling engines, NASA is sponsoring a JPL project which will lead to a versatile test engine. One objective of this program is to lay the ground work for an industry-produced version of the engine that will support the requirements of educators and researchers in academic, industrial, and government laboratories.

The preprototype engine represents the first assembled engine and is being used to support the development of a broad range of analytical modeling and experimental efforts. The engine is a horizontally opposed, single-action Stirling engine with a dual-crankshaft drive mechanism. The preprototype configuration uses helium gas and is heated within a closed-cycle system by an external electrical source.

Preliminary experimental results obtained during engine tests compared favorably with analytical prediction models. The potential for a fully operational test engine was established.

(The Stirling engine derives its name from Robert Stirling, Scottish engineer, who conceived the idea of an air engine using a regenerator.)

Figure (opposite page): The Stirling laboratory research engine built by JPL is shown here in the preprototype phase. It is being used to support the development of testing and analysis of the Stirling engine in the United States.



Page intentionally left blank

Page intentionally left blank

III. Earth Orbital Applications

920
SEASAT DATA UTILIZATION: SCANNING MULTICHANNEL MICROWAVE RADIOMETER

Continuing evaluation of the 1978 Seasat's Scanning Multichannel Microwave Radiometer (SMMR) data advanced the accuracy of several oceanographic determinations this year. Improved algorithms were formulated for retrieving sea surface temperature, surface wind speed, atmospheric liquid and water vapor, and rain rate.

A series of workshops compared Seasat spacecraft data with surface observations made during the mission, identified problems in earlier sensor and geophysical algorithms, and evaluated subsequent approaches to their solutions.

Accuracies of SMMR geophysical readings were assessed by a Joint Air-Sea Interaction (JASIN) workshop in March 1980, as follows:

Sea surface temperature (SST) estimates in the northern and western Pacific when rain and sunglint are absent show a deviation of 1.5 degrees Celsius about a warm bias of 0.6 degrees Celsius. (Figure opposite

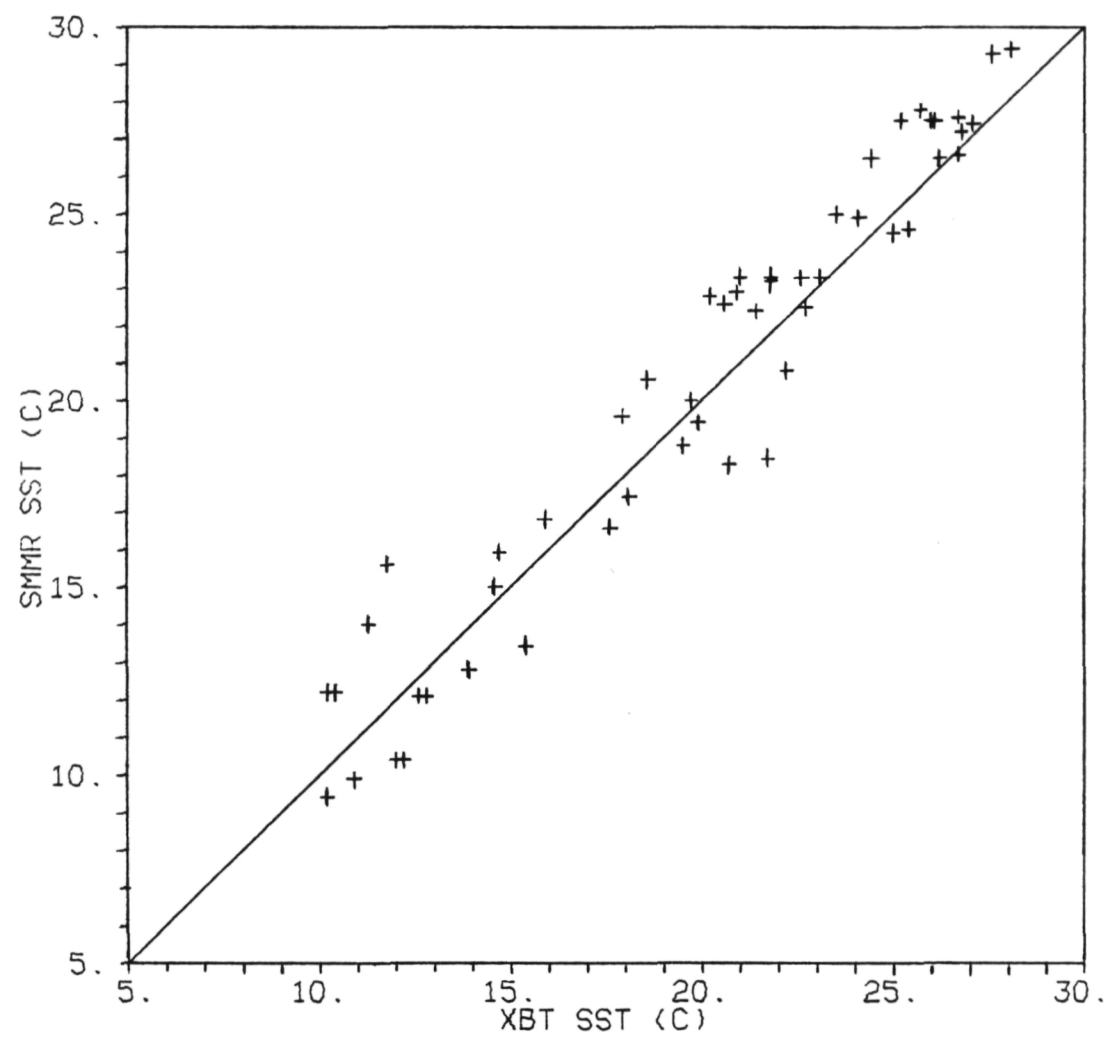
shows this comparison made during descending Seasat passes.) In areas of heavy radio frequency interference (RFI), such as the JASIN area between Great Britain and Ireland, SST determinations degrade markedly.

Wind Speed retrievals in the northeast Pacific and northwest Atlantic had a scatter of 2.5 meters per second (bias 0.5 m/s) at least 150 kilometers away from land and rain. In the JASIN area wind estimates were degraded by RFI and possibly land contaminations.

Atmospheric water vapor in the JASIN area was measured within an 0.1-gram-per-square-centimeter accuracy compared to surface readings taken within +2 hours of the overpass. In the tropics, retrievals are 15 percent high, but some land contamination may be present.

The SST, wind speed, and atmospheric water determinations, uncontaminated by land, rain, and sunglint, fell within mission specifications.

Figure (opposite page): SMMR SST comparisons with high-quality surface truth taken in the open Pacific. The spacecraft data are from descending passes (night time), uncontaminated by rain. The surface truth, from expendable bathythermographs (XBT), is accurate to 0.2°C. The comparisons, shown clustering around the perfect agreement line over a 20°C range in SST, have a 1.5°C scatter about a 0.6°C warm bias.



029

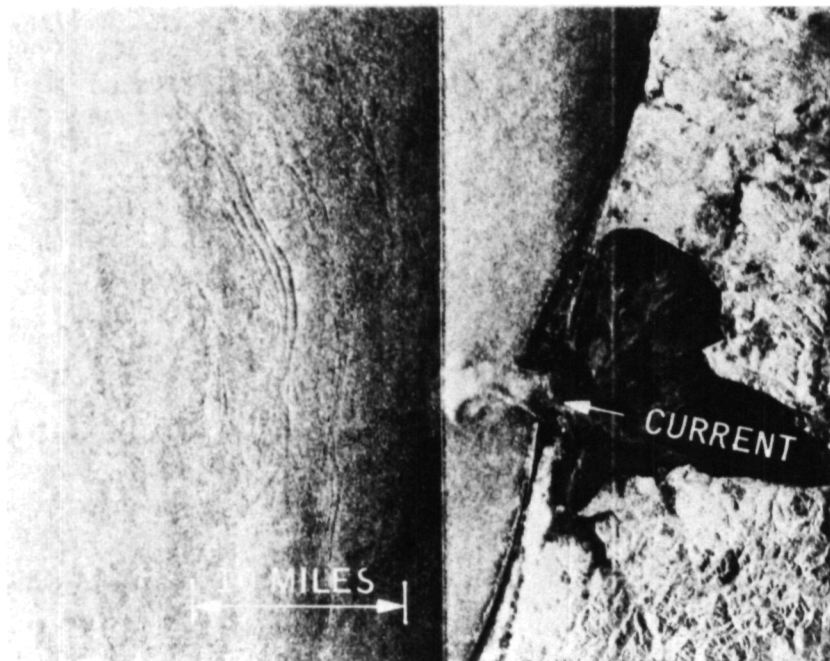
OCEAN CURRENTS MEASURED BY SEASAT RADAR

Recent work at JPL has demonstrated that the Seasat Synthetic Aperture Radar (SAR) is capable of detecting and measuring ocean current parameters. Since the ocean surface within the current boundaries is travelling at a different velocity than the rest of the ocean surface, it should be expected that the modulations due to the features within the current region would be shifted in position in the SAR image. This would be apparent as a bright band in the image obtained by the SAR on the side of the current boundary toward which average displacement of the image components takes place. A corresponding dark band should be observable on the opposite side. The width of the dark and the light bands should be related to the velocity profile of the current.

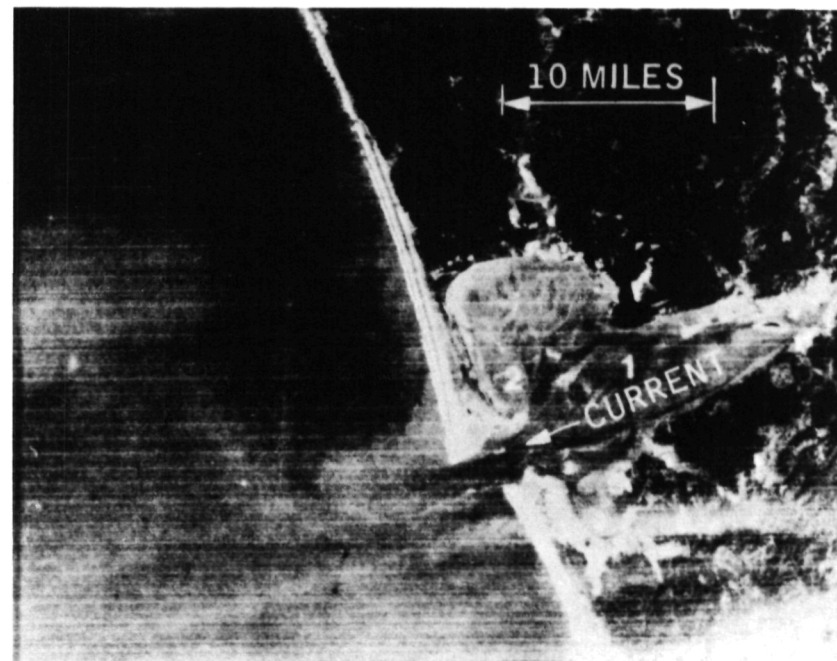
The above concept was tested with a Seasat image of Gray's Harbor, Washington, shown in the figure (opposite left). The satellite image was obtained during an ascending orbit moving toward the north with the subtrack location approximately 290 kilometers from the swath center to the west of the harbor entrance in the satellite range direction. The bright band

appears clearly at the south ebb current boundary as predicted. A somewhat diffused but visible dark band can also be discerned at the north current boundary. To demonstrate that these bands are generated by the doppler displacement of moving surfaces in the SAR image, a Landsat-1 image of Gray's Harbor during an equivalent ebb cycle is shown on the right. The optical Landsat image shows no bright or dark bands at either current boundary. By measuring the width of the bright band in the SAR image, an estimate of the current magnitude is shown to be 1.0 ± 0.4 meters per second. This compares favorably with measurements obtained from the tidal current tables at the time of the satellite crossing, which give an ebb current of 1.4 m/s.

It is also possible to obtain measurements of the radial direction of the current velocity directly from the SAR signal, by measuring the doppler shift in the signal transform. Future work will refine measurement of current magnitudes from image shifts and develop current measurement techniques from signal doppler shifts.



**SEASAT - SAR IMAGE
7 JULY 1978**



**LANDSAT-1, BAND 5 IMAGE
8 JANUARY 1973**

Grays Harbor, Washington

D30

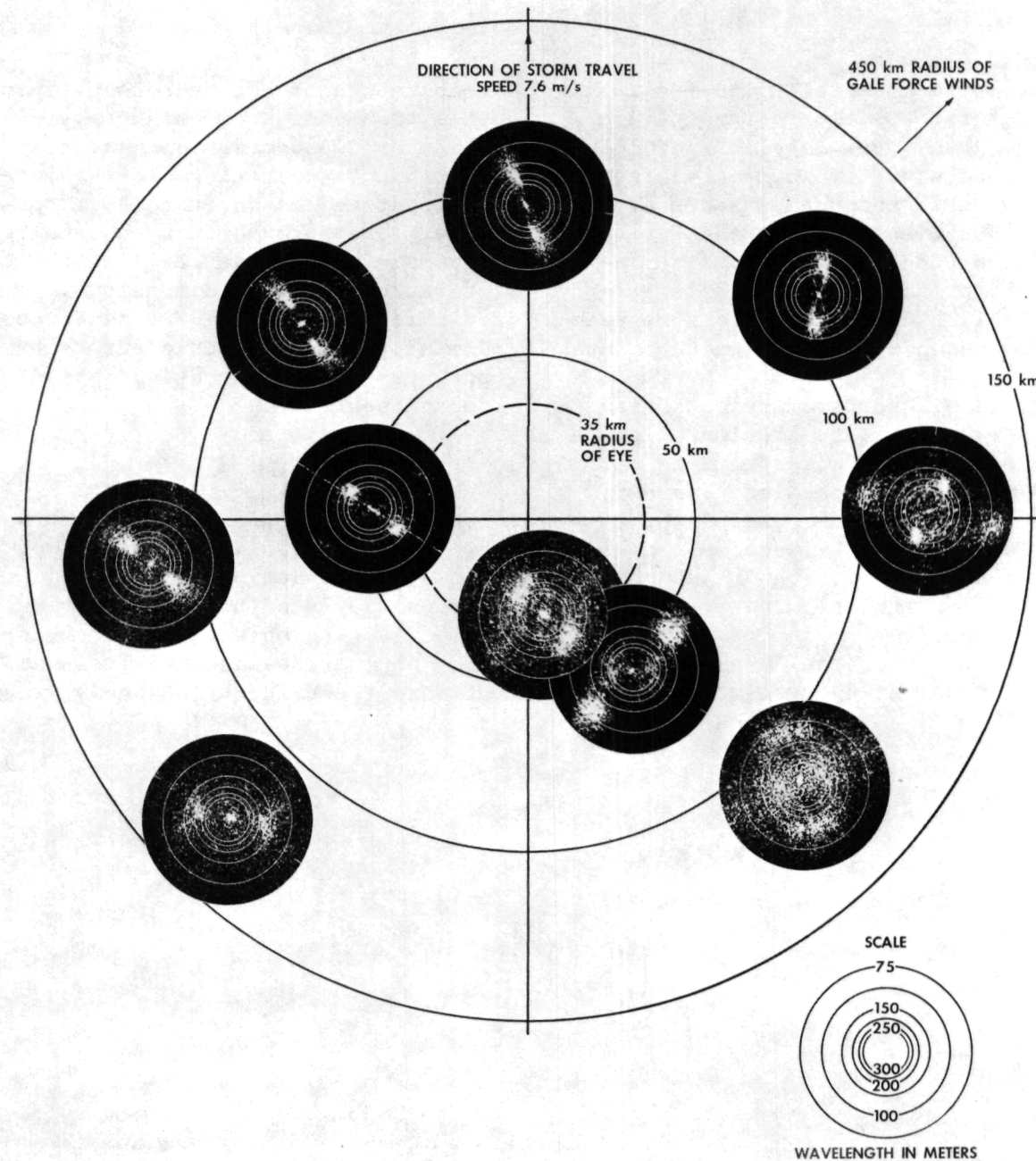
OCEAN WAVE PATTERNS UNDER HURRICANES

While much progress has been made in avoiding the loss of human lives due to hurricanes, primarily because of aircraft and satellite surveillance techniques, the meteorology of this cyclonic heat engine is not yet fully understood. Conventional techniques have not been adequate in acquiring data under hurricanes. However, the airborne Synthetic Aperture Radar (SAR) has been shown by JPL to be very useful in collecting information under hurricanes, particularly of the wave patterns. Since 1976, JPL has been collecting information on the directional properties of hurricane waves using the SAR onboard a NASA CV-990 research aircraft. These include the Tropical Storm Emmy, Hurricane Gloria, Typhoon Heather, and the Hurricane Frances.

The opposite figure shows the typical wave pattern under a hurricane. The figure shows that the waves are not symmetrically distributed around the hurricane eye. Dominant waves propagate ahead of the hurricane along

lines normal to the local wind direction. (The wind-field blows in a counterclockwise spiral around the eye.) Confused and unexplained directional distributions can be seen in the lower right sector of the hurricane. While much of the information in the figure is yet to be explained, some major observations can be stated. The axial symmetry of the wavefield can be attributed to the forward motion of the hurricane. The residence time for wave generation is significantly greater in the region to the right of the eye if the hurricane has a moderate forward velocity. The dominant growth appears to be associated with group velocities that are equal to or somewhat greater than the speed of the hurricane. The dominant waves spread out in an arc ahead of the hurricane eye and have wavelengths of the order of 250 meters with a corresponding group velocity of 10 meters per second. The hurricane forward speed is 8 m/s. These waves appear to have optimum hurricane residence time with respect to wave generation.

Figure (opposite page): Directional spectral wave transformations, Hurricane Gloria, 30 September 1976.



DB 13
PROJECT ARIES (ASTRONOMICAL RADIO INTERFEROMETRIC EARTH SURVEYING)

Project ARIES further demonstrated the feasibility of three-dimensional Earth position determination with a few-centimeter accuracy over baselines of 180 to 500 kilometers. The technique employs very long baseline interferometry (VLBI) and uses quasars as a reference frame. Caltech's Owens Valley Radio Observatory (OVRO) and the Deep Space Network at Goldstone are used with the ARIES transportable 9- and 4-meter antennas to establish distance vectors between the two reference stations and a grid of remote points.

The 4-m diameter radio interferometric station began operations. This high-mobility station allows a data acquisition yield of two distinct locations per week compared to the 9-m station's one location per month. The 4-m station has been made possible by utilizing an X-band (8.4 gigahertz) low-noise traveling wave maser receiving system, with the maser cooled to four kelvins by liquid helium.

The microwave performance of the X-band receiving system is equivalent to an operating system noise

temperature of 30 K across a 100-megahertz bandwidth. This technology was originally developed for interplanetary spacecraft communications. Validation experiments comparing the two antennas were conducted by locating the antennas 30 m apart at the JPL ARIES site. They proved that the smaller antenna yielded the same results as the larger within 10 centimeters or better in three dimensions. The transition to primarily X-band ARIES geodetic monitoring offers immunity to ionospheric errors by a factor of 13 over previous monitoring using S-band (2.3 GHz) reception techniques.

The ARIES Project is continuing to monitor its previously established network of ten locations while pursuing the refinement of radio interferometric geodesy goals of high accuracy at reduced costs. Cost-effectiveness objectives are being met by the 4-m system and computerized data analysis at a joint facility of JPL and the Caltech Astronomy Department.

Figure (opposite page): A handy tool for increasingly accurate Earth measurements is the 4-meter high-mobility radio interferometric station put into operation this year by Project ARIES at JPL and elsewhere.



D3P

COMBINING SEASAT RADAR AND LANDSAT MULTISPECTRAL IMAGES

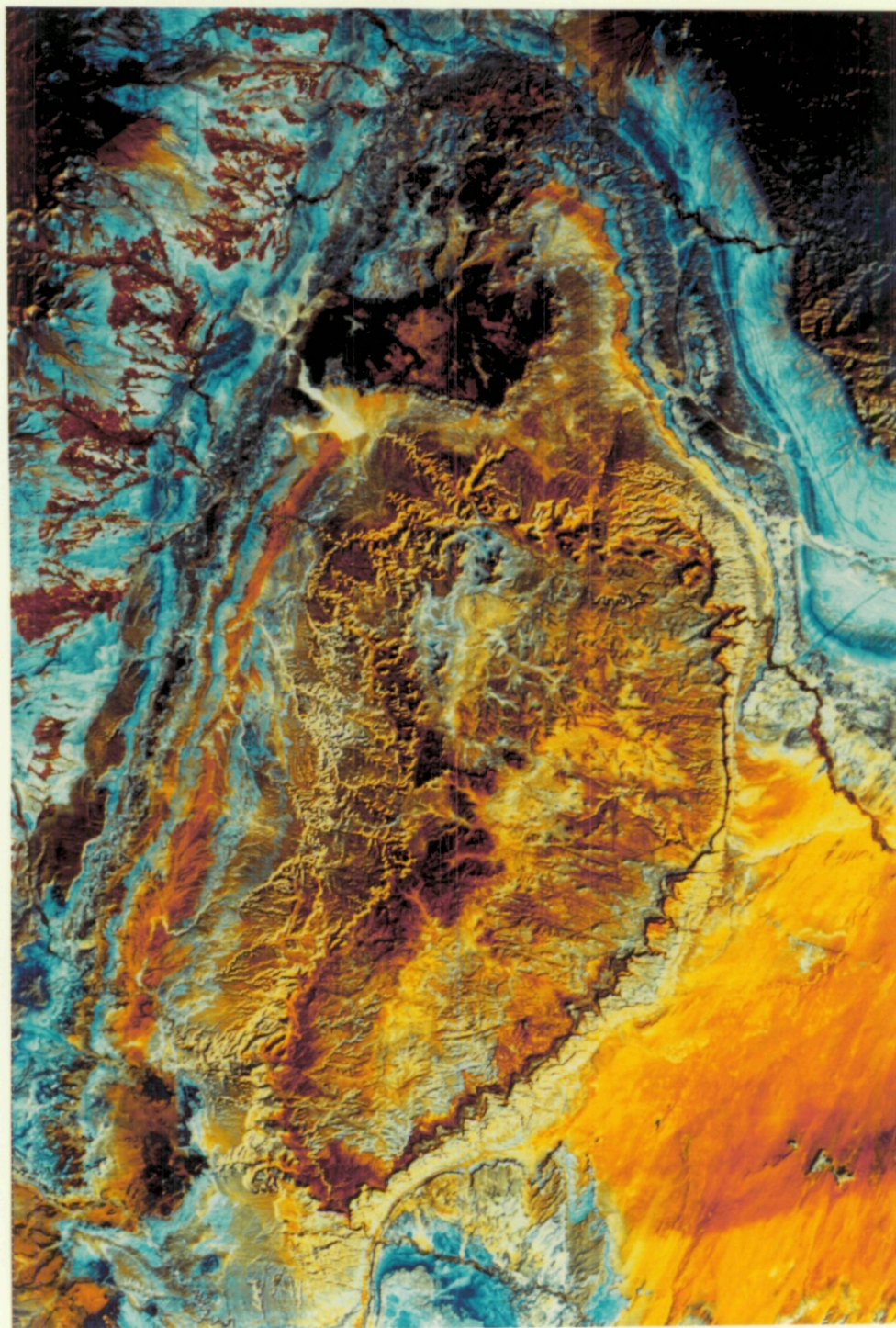
To develop geological remote sensing techniques for resources exploration, a Seasat radar image and a Landsat multispectral image of the San Rafael Swell in east central Utah were superimposed or coregistered by JPL's Image Processing Laboratory for an investigation conducted by the Radar Remote Sensing Team. Despite difficulties posed by differing geometries and brightness characteristics of the two systems, enough common points were found to coregister the images.

Because the two imaging systems give different information about the Earth's surface, the combination of the two appears to provide better rock identifica-

tion capability than either alone. The coregistration method is a promising geological tool for discriminating rock types such as sandstone and shale. For example, sandstone formations of similar composition but differing outcrop characteristics may be separated by the combined image because of the roughness information added by Seasat's radar data.

The San Rafael Swell is a rugged upfold of sedimentary rocks about 100 kilometers long and 50 km wide. Exposed rocks are mostly sandstone and shale with some limestone and conglomerate. The swell contains economically significant deposits of uranium, found in particular sandstone formations.

Figure (opposite page): The upfolded structural configuration and differing rock types are shown in this coregistered Seasat-Landsat image of the San Rafael Swell, whose jagged sandstone cliffs are sharply delineated. The browns and copper tones are basically sandstones and sand dunes; the blues are shales. The San Rafael River winds through the right center of the image, joining the Green River to the east.



Page intentionally left blank

Page intentionally left blank

IV. Information Systems and Space Technology Development

D33

DYNAMIC BALANCING IN A VACUUM

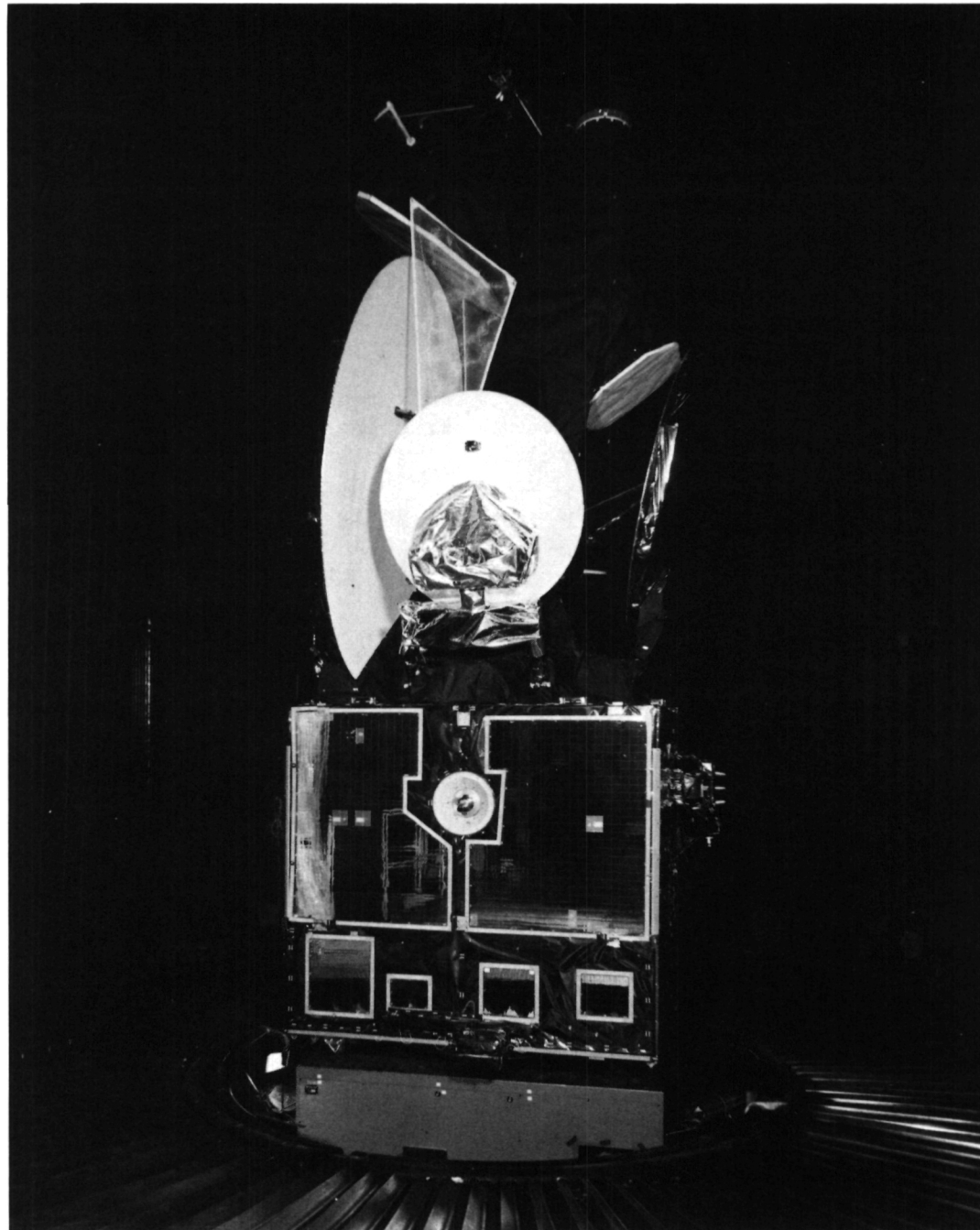
For asymmetric, spin-stabilized spacecraft, aerodynamic forces caused by appendages such as antenna reflectors induce unacceptable errors during dynamic balance operations in air. This aerodynamic poser was solved by JPL by balancing the Intelsat V spacecraft on a vacuum-rated Schenck-Trebel machine in the 25-foot JPL Space Simulator.

The balance facility, believed unique in the United States, measures the amount and direction of unbalance in two planes under vacuum conditions less than 1 torr.

The remote-controlled machine operates between 30 and 240 revolutions per minute. Motors and bearings are hermetically enclosed and cooled with ambient air plumbed through the bottom of the simulator.

Tests on the Intelsat V for the Ford Aerospace and Communications Corporation reduced the spacecraft unbalance from 4.28 kilograms to 30 grams, and the final center of gravity offset was less than 0.002 inches, well within acceptable limits.

Figure (opposite page): The Intelsat V spacecraft is shown attached to the dynamic balance machine in the JPL 25-foot Space Simulator before undergoing unbalance correction.



D3H

SPACECRAFT CONTAMINATION INVESTIGATIONS

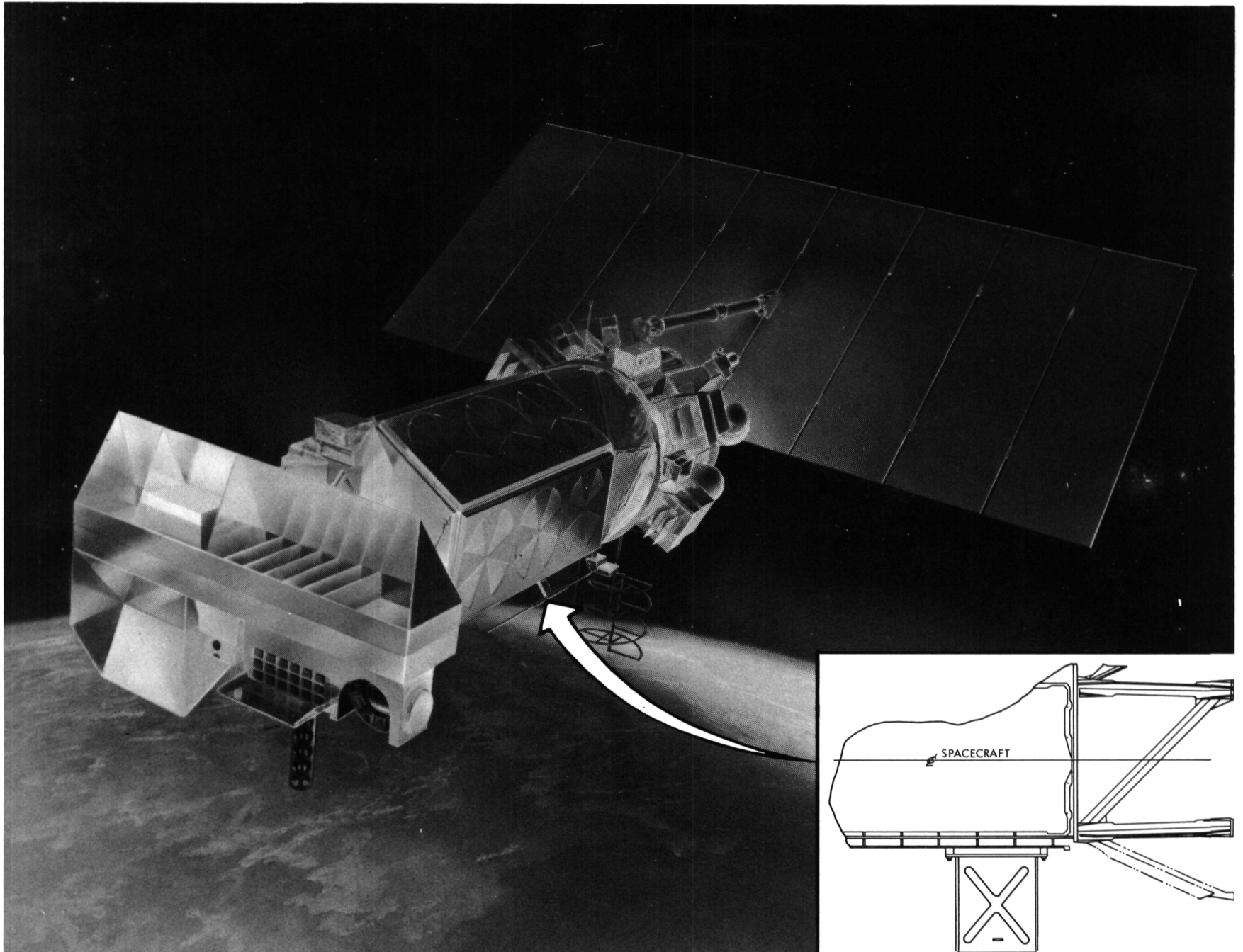
A spacecraft contamination monitor was developed for the National Oceanic and Atmospheric Administration (NOAA) environmental service satellite, scheduled for imminent launch. The tested and installed instrumentation will measure contamination from several sources: solid rocket motor plume backflow, hydrazine thrusters, and long term outgassing.

The NOAA weather satellite was selected for this experiment because two previous spacecraft of the same design encountered contamination-caused thermal control problems and systems anomalies. The JPL monitor should provide data necessary to quantify and understand the anomalies experienced by the NOAA and other scientific satellites.

Additionally, JPL developed a computerized Contamination Analysis Program (CAP) for solving large multinodal (many geometric surfaces) contamination problems in a free molecular flow environment. The low-temperature operation required for thermal control surfaces and optics makes some spacecraft extremely vulnerable to contamination. Comprehensive contamination assessments were performed for Galileo, the Infrared Astronomical Satellite (IRAS), and the Tracking and Data Relay Services Satellite (TDRSS).

Current design of these spacecraft appears capable of achieving mission objectives if CAP-recommended contamination procedures are employed in all phases of construction, ground handling, and flight operations.

Figure (opposite page): This artist's rendering (with inset cutaway drawing) shows how the JPL spacecraft contamination monitor will fit into the National Oceanic and Atmospheric Administration (NOAA) environmental services satellite scheduled for launch early in 1981.



The JPL surface chemistry laboratory measured the detailed chemical environment of the silicon/silicon dioxide (Si/SiO_2) interface using X-ray photoelectron spectroscopy (XPS) and related these measurements to the reliability and radiation hardness of microelectronic devices.

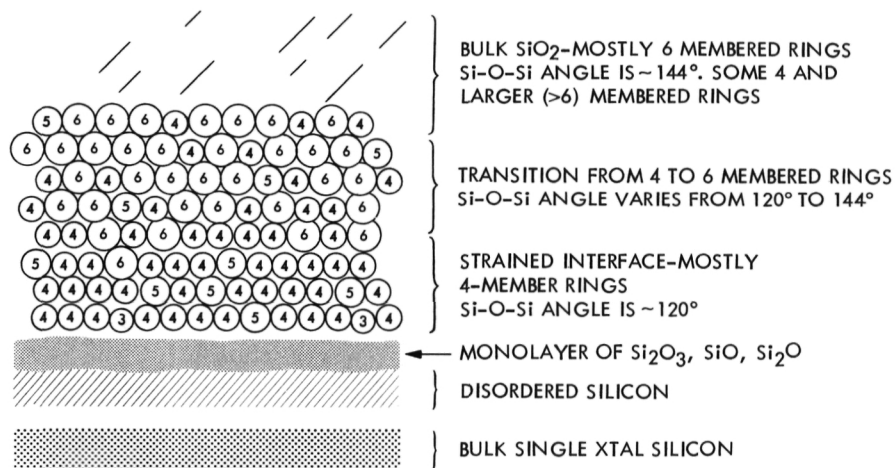
Using XPS and chemical depth-profiling techniques, it was found that the oxide is SiO_2 to within one monolayer of the silicon substrate. An abrupt chemical interface (approximately one monolayer) was found with a mixed composition comprising Si_2O_3 , SiO , and Si_2O . Except at this interface, the SiO_2 chemical units are arranged in ring structures whose average size depends upon distance from the interface. The bulk of the oxide is composed of 6-membered rings similar to alpha-quartz. Within 30 angstroms of the interface, there is a strained layer of 4-membered rings induced by the lattice mismatch between the bulk oxide and the substrate. This layer's composition is dependent upon the details of the wafer processing chemistry.

The ring model is illustrated schematically in the top left figure, where circles are used to indicate network rings. This observed structure has been used to develop a structural model for hole and electron trap generation by ionizing radiation. These traps have been observed during *in situ* experiments examining the interfacial regions of radiation-hard and -soft gate oxides.

XPS techniques have also been extended to the investigation of metal/semiconductor interfaces. The primary goal of these studies has been to examine these interfacial regions nondestructively and to relate the observed chemical structure to such electrical properties as Schottky-barrier heights and ohmic contact formation. One experimental approach is to deposit

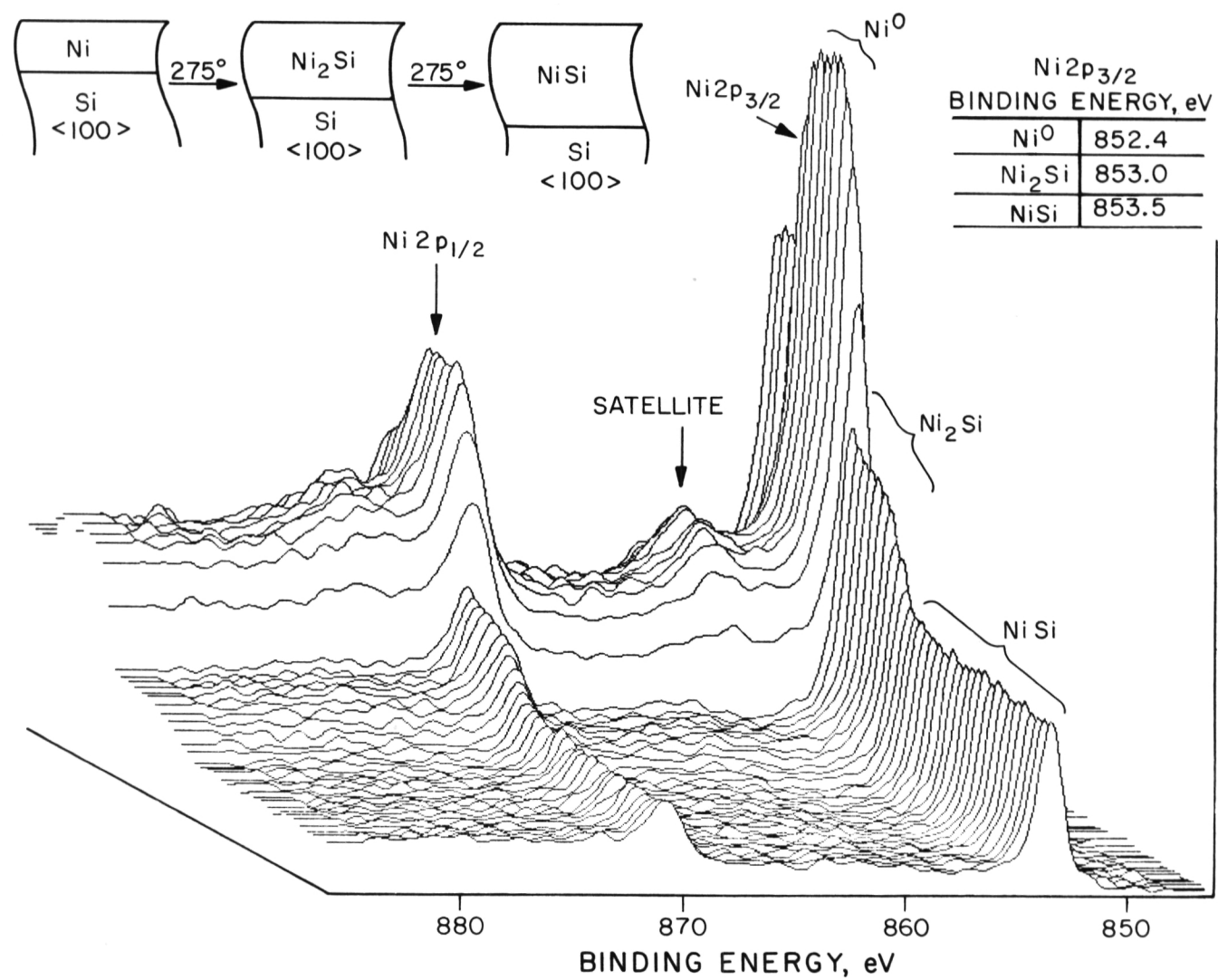
sequential monolayers of a metal on silicon under ultra-high vacuum conditions. By simultaneously monitoring the metal and silicon photoemission signals as a function of metal coverage, the chemical development of the interface has been followed *in situ*.

These metal/silicide/silicon interfaces have also been investigated by studying the metal and silicon XPS signals during *in situ* growth of the metal silicide. The experiments are yielding information on such fundamental questions as the variation of structure and chemical bonding across the interfacial region.



Schematic model of the Si/SiO_2 interface as determined using x-ray photoelectron spectroscopy.

Figure (opposite page): 3-D plot of the $\text{Ni}2p$ core levels illustrating the intensity change and chemical shift observed during sequential silicide compound formation.



D36

CHARGE COUPLED IMAGING DEVICE TEST FACILITY

Following the Voyager mission, vidicon-tube technology for spacecraft imaging systems will be supplanted by solid-state Charge Coupled Devices (CCDs). The 800 x 800 matrix CCDs offer performances previously unattainable: very wide spectral response, extremely low light level sensitivity, dynamic range of over 4000 levels, and a near-absolute geometric stability. The mission objectives for both Galileo and the Space Telescope were established based on the new CCD capability.

Imaging CCDs vary widely in operating characteristics and are electronically complex to drive. The individual device optimization of the driving signals coupled with the greater performance range to be characterized has increased the amount of required computing capacity by a factor of 20 over that previously expended on vidicons.

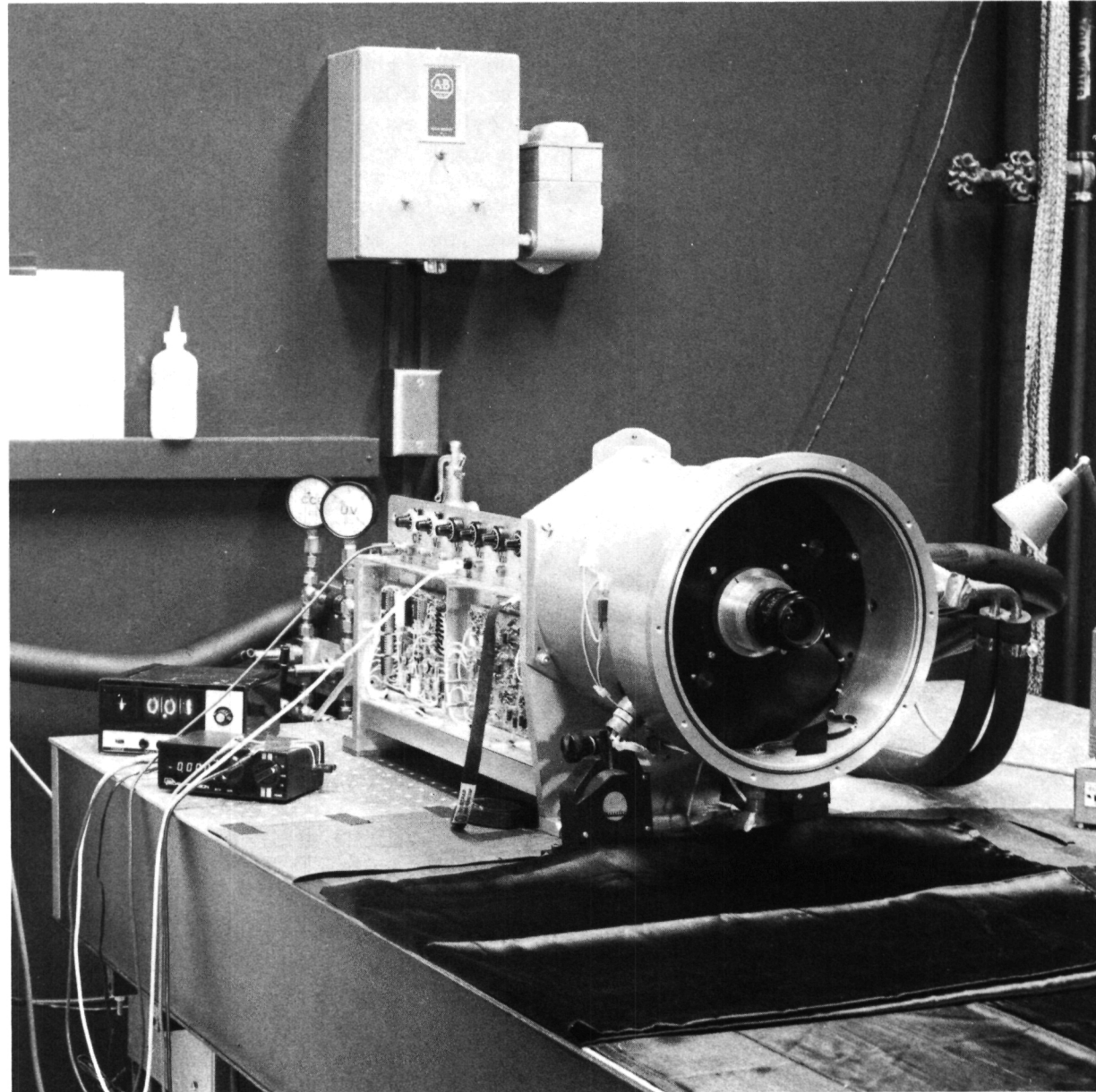
To meet these needs, JPL assembled the CCD Screening and Test Facility. This new facility includes a very light-tight, reflection-free test room, a CCD camera enclosure, supporting optics and

electronics, and an integrated computer setup that (a) controls, monitors, and records the operation of the CCDs, and (b) provides all the computation and products (printouts, plots, and hard copy images) required for analysis.

The computer system itself has involved several new technology developments, including (a) the incorporation of major imaging processes into main-frame micro-code, (b) a real-time software system capable of handling 3-1/2 megabits per second, and (c) the build-up of 16-bit hardware imaging display trace, and hard copy peripherals.

Pre-screening of a CCD requires 1-1/2 days of system time; a final screening requires 3 days. Both run in an automatic mode with the computer pausing only to allow directed target and/or light level changes. The established screening procedures require a technician for only half of daytime test hours and is allowed to run unattended (often overnight) for the remaining computing and analysis operations.

Figure (opposite page): Imaging CCD camera enclosure and control electronics.



D37

DEVELOPMENT OF AN ULTRAVIOLET EXCIMER LASER FOR ATMOSPHERIC SENSING

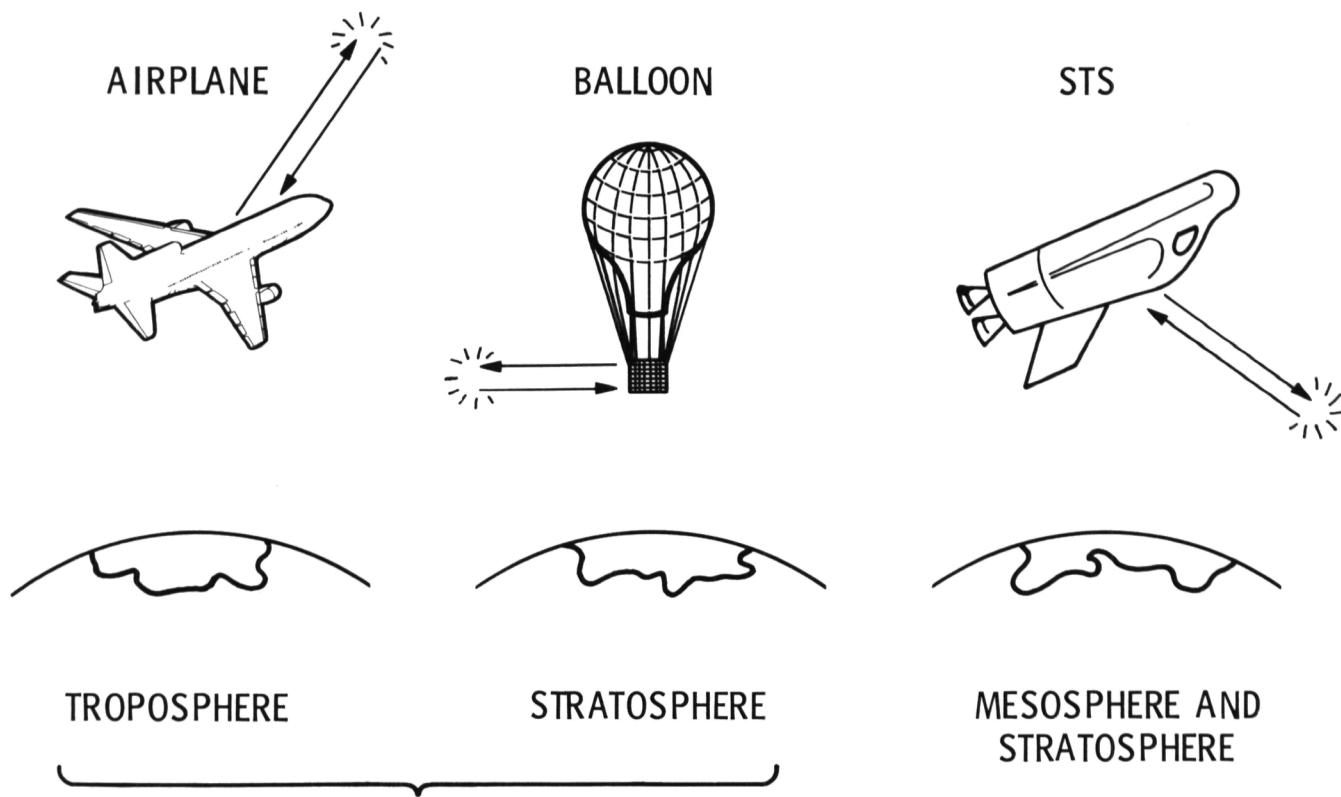
The oxygen-hydrogen radical plays a key role in the chemical cycles involving the formation and destruction of ozone; therefore, it is of vital importance for the understanding of chemical models of the atmosphere to have good measurements of the OH concentration profile. Even though the OH radical is important in atmospheric chemistry, it is present in only trace amounts, which makes detection by conventional sensing methods difficult.

Laser fluorescence remote sensing methods have proven to be a specific, extremely sensitive technique to measure concentration profiles of trace species. Until recently there was a scarcity of high-energy tunable laser sources in the ultraviolet needed to detect OH molecules.

At JPL a high energy xenon-chloride excimer UV gas laser was developed and demonstrated with a wavelength gain region from 3073.8 to 3085.7 angstroms, where several OH absorption lines are known to lie.

Because the UV laser pulse can lead to chemical formation of OH in the troposphere. JPL researchers developed simple techniques to extract the energy from a XeCl laser in a subnanosecond pulse with high efficiency. The shorter pulses eliminate the artificial OH generation problem that has plagued other attempts at laser measurement of OH in the troposphere.

In separate experiments the collision-free radiative lifetimes for the fluorescent state of OH excited by the XeCl laser pulse were measured, along with the quenching rate constants from excited states with various atmospheric gases, including nitrogen, oxygen, and water molecules. These radiative and quenching rates are necessary to calculate the fluorescence efficiency or how many photons are emitted back to the detector compared to the number of photons absorbed by OH during the laser pulse. The XeCl excimer laser development for OH detection can be applied to laser sensing of other molecules at other wavelength regions in the ultraviolet.



Laser remote sensing of the upper atmosphere.

930

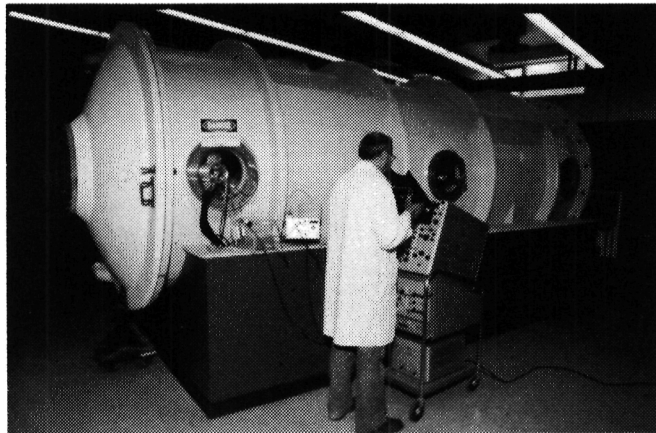
ADVANCED MPD THRUSTER RESEARCH

Magnetoplasmadynamic (MPD) arcjets for use as thrusters on NASA spacecraft are being investigated in tests underway at Princeton University and JPL. Initial data obtained using argon as propellant (any noble gas could serve) indicate that MPD thrust densities over 1000 times higher than other electric propulsion systems can be attained at efficiencies well over 30 percent.

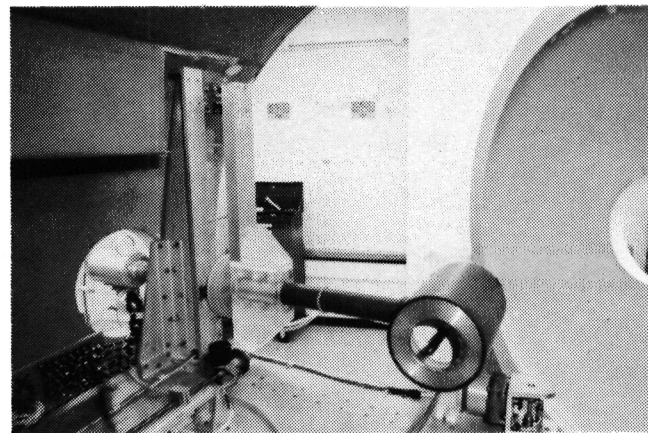
The test (begun at Princeton in 1976) employs a fiberglass vacuum tank and a swinging gate thrust

stand which measures the impulse of the MPD discharge. The device operates in one-millisecond-long pulses and requires pulsed power levels up to several megawatts.

Advanced MPD thruster performance analysis is expected to continue in tandem at Princeton and JPL with the construction this year of JPL thruster and vacuum test laboratories. The NASA research project is being managed by JPL.



FIBERGLASS VACUUM CHAMBER
HOUSING A SWINGING GATE
THRUST STAND



THRUST STAND WITH INTEGRALLY
MOUNTED MPD THRUSTER

MPD thruster system technology performance test facility.

NICKEL-CADMIUM BATTERY RESEARCH

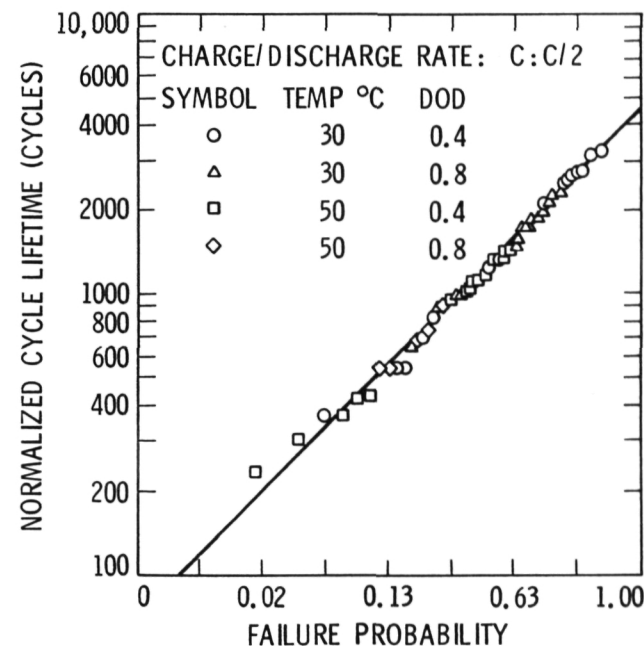
Spacecraft designers have the problem of trying to predict the reliability of nickel-cadmium batteries used in many power systems. Researchers at JPL developed a failure-predictability model that correlates variables such as battery temperature, size, and discharge depth for the first time.

The successful testing of the model is regarded as a major step toward realistic life prediction and

performance evaluation of nickel-cadmium batteries. The theory evolved hypothesizes that flaw growth in a battery is due to the interaction between electrons and flaws, and a cell failure will occur when a flaw reaches a critical size.

The figure below shows how the model can be used to estimate battery lifetime and reliability.

- FLAW THEORY
 - FAILURE DUE TO GROWTH OF FLAWS ABOVE CRITICAL SIZE
 - GROWTH RELATED TO ELECTRON MOVEMENT
- FOR THE FIRST TIME A THEORY SUCCESSFULLY CORRELATES CRANE TEST DATA TO YIELD LIFE PREDICTION
- MAJOR STEP TOWARD
 - LIFE PREDICTION AND PERFORMANCE EVALUATION
 - INDICATOR OF FAILURE MECHANISM
 - GUIDE FOR RESEARCH AND TEST PLANNING



Nickel-cadmium cell failure model.

D40

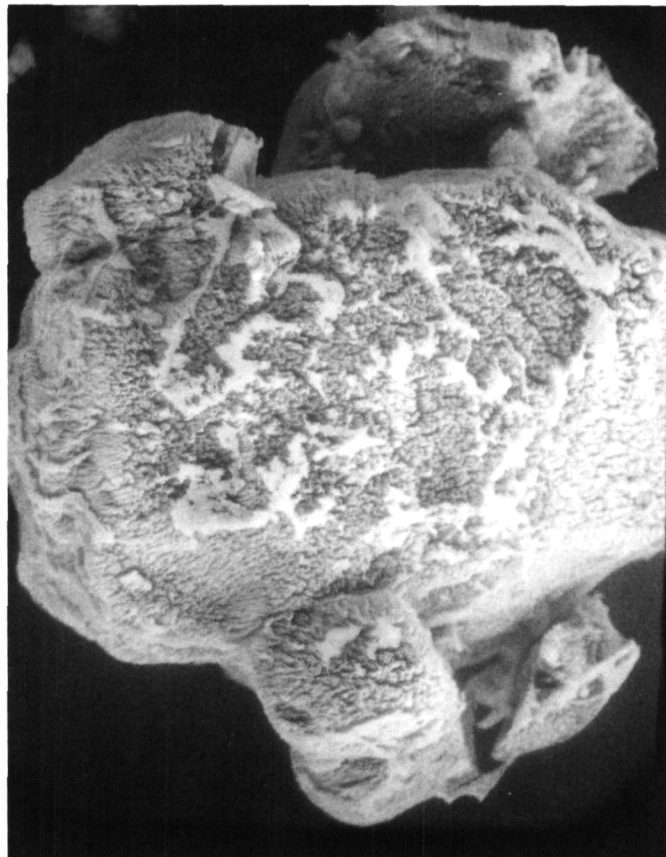
COATED OXIDIZERS FOR STABILITY IN SPACE PROPULSION ROCKETS

While solid-propellant technology for rockets is maturing, some of the fundamentals of combustion have remained elusive, largely due to instability problems. Based on a JPL model for solid-propellant combustion, a concept of thermal performance modification to suppress instability was developed.

The thermal performance is tailored in any propellant by coating the oxidizer (typically ammonium perchlorate crystals) with a specially selected chemical. Polyvinyl alcohol is one of several candidates being tried for the coating, which represents about one percent by weight of the propellant. The coated-oxidizer concept for instability suppression is not unique, but the idea of tailoring thermal performance by coating is believed to be novel.

The tests in a simple L-star end-burning rocket motor indicate that the coating does suppress instability in certain regimes of pressure and L-star. Results also were confirmed in the more advanced microwave burner. In the low-frequency regime, the measured response function shows a lower value for the coated oxidizer than for the uncoated.

The concept was tested on several batches of ammonium perchlorate propellants in hydroxy-terminated polybutadiene binder systems. Nonmetallized propellants were used since instability occurs more often in such systems than in their metallized counterparts. The project is continuing to evaluate the optimum coats for different specific applications.



A scanning electron microscope (SEM) picture (magnification 1000x) showing an ammonium perchlorate (AP) crystal coated with 0.1 percent by weight of polyvinyl alcohol (PVA) for instability suppression through thermal performance modification. PVA is one of the several candidate chemicals tried for the coating.

D41

FLUORINE-HYDRAZINE PROPULSION SYSTEM

A major step in the development of a 3560-newton (800-pound) thrust rocket engine was taken when JPL engineers successfully used rhenium for the thrust chamber. The rhenium chamber completed a 500-second firing test with no detectable erosion damage as part of NASA's ongoing Space-Storable Propulsion Systems Technology Program.

Rhenium is a refractory metal with good ductility and high-temperature and chemical resistance. It was first evaluated as a liner for a carbon thrust chamber, but an all-rhenium chamber has proven superior in this year's tests.

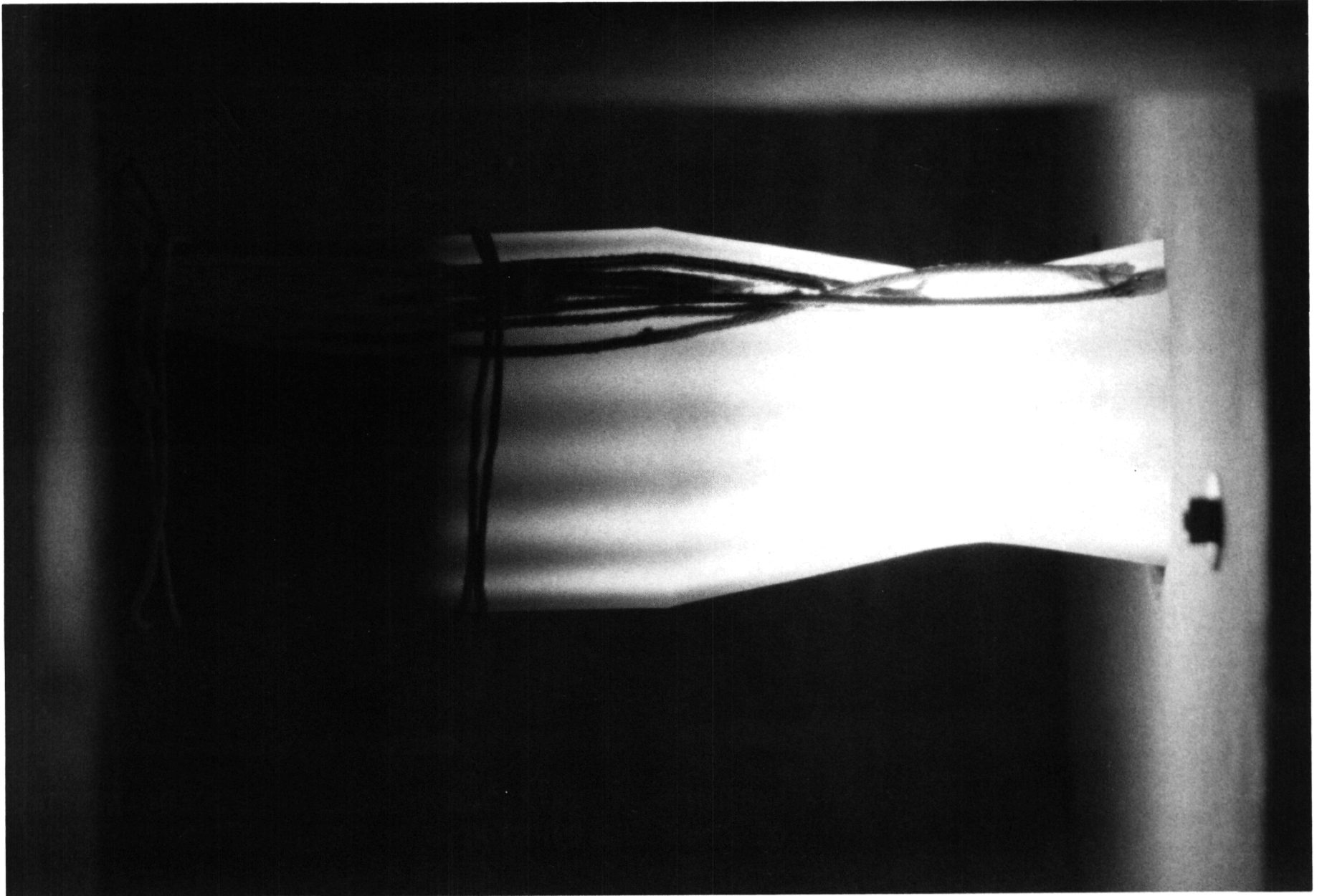
The goal of the program (sponsored by NASA's Office of Aeronautics and Space Technology) is to prove the feasibility of a fluorine-hydrazine propulsion system for spacecraft application by the end of Fiscal Year 1982. The advanced fluorine propulsion system is

designed to be used for Space Shuttle-launched planetary missions from the mid-1980s on.

The fluorine rocket engine's high specific impulse -- 3580 newtons per second for each kilogram of propellant -- can provide the performance required for long-duration missions to any planet in the solar system and for insertion into orbit around planets or their satellites. By combining hydrazine with a cryogenic oxidizer, an indicated performance improvement of 25 percent has been attained over previous liquid fluorine systems such as the Viking Orbiter.

Besides the rocket engine demonstration, this year's advances included fabrication of fluorine-compatible insulation, system thermal design and analysis, and completion of Space Transportation System safety reviews at the Johnson and Kennedy Space Centers.

Figure (opposite page): Glowing nozzle of the space-storable rocket engine near the end of a recent 500-second firing test of a thin-walled, all-rhenium thrust chamber. Temperatures of 140 degrees Celsius at the injector end (left) to 1600°C at the nozzle throat were registered. The test series at JPL's Edwards Test Station indicated the rhenium-chambered engine should be capable of over 10,000 seconds of burn.



Page intentionally left blank

Page intentionally left blank

V. Technology Applications

D48

AEROSOL PARTICLE ANALYSIS BY MASS SPECTROMETRY

A new technique for analyzing the chemical composition of single aerosol particles within the diameter range of 0.1 to 5 micrometers on a continuous, real-time basis is currently being developed at the Jet Propulsion Laboratory in collaboration with the University of California at Los Angeles (UCLA). It involves a combination of particle beam generation and mass spectrometric methods. The key enabling technology is the application of a JPL-developed ultrasensitive electro-optical ion detection (EOID) scheme for mass spectrometry.

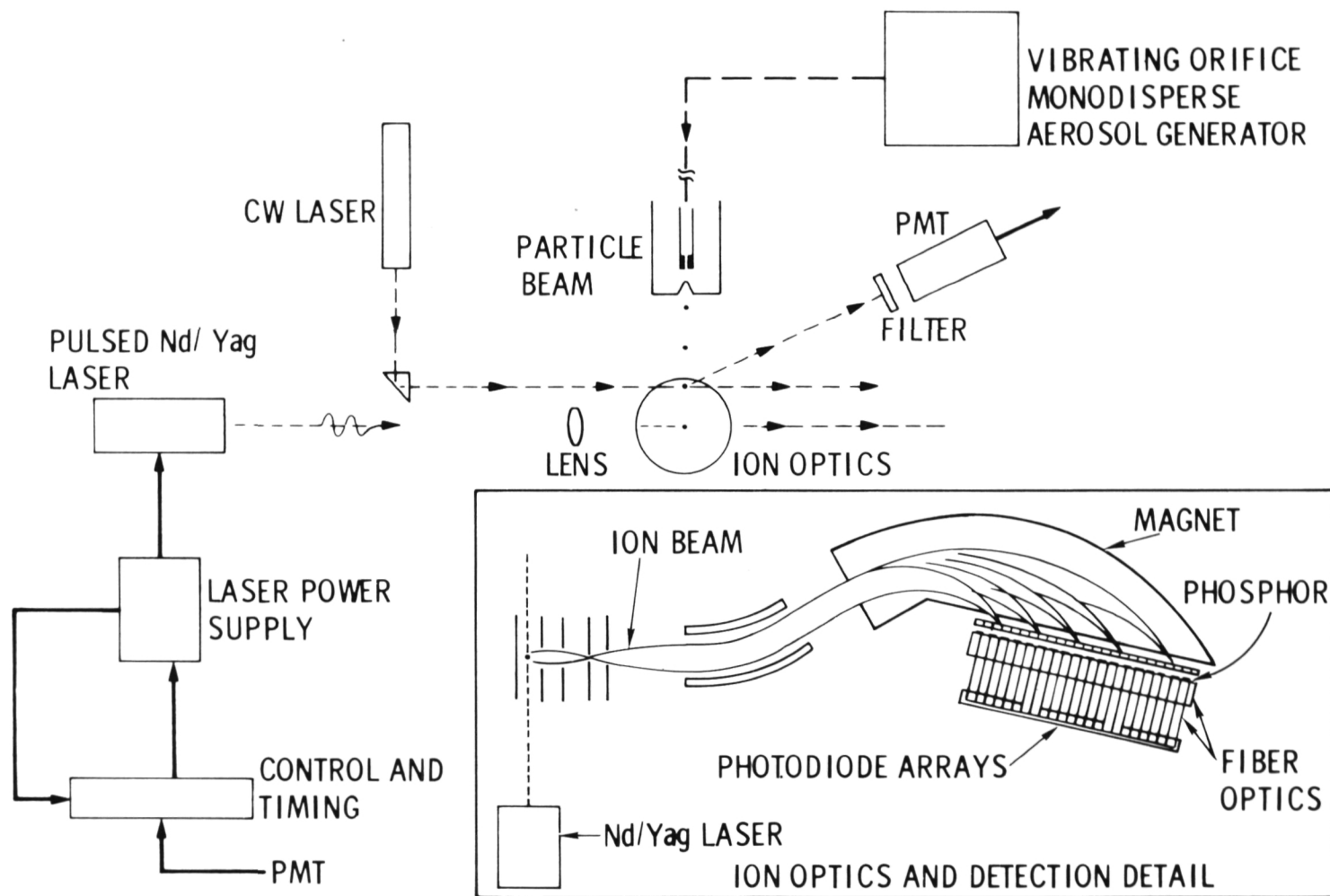
The goals of this research are (1) to prepare the aerosol particles for their efficient introduction into the ion source region of the spectrometer, (2) to develop an optimum method for particle volatilization and ionization, (3) to relate the resultant mass spectra to the chemical composition of the incoming particles, and (4) to apply the technique to the measurements of atmospheric aerosol and biological particles such as bacteria and viruses.

A beam of monodisperse (same size) particles of known chemical composition and flux has been generated. Methods for the volatilization and ionization of these aerosol particles are being studied. A combination of thermal volatilization of individual particles by impaction on a hot rhenium surface with electron bombardment ionization was employed for the chemical analysis. Results were obtained with different inorganic and organic aerosol particles of varying sizes.

One system of practical importance is sulfate/sulfite analysis of particles. Impaction of ammonium sulfate particles on a hot rhenium filament followed by electron bombardment results in fragment ions of SO^+ , SO_2^+ , and SO_3^+ (oxides of sulfur) from the sulfate part of the salt. No signal of SO_3^+ is observed from a sulfite particle. The absence of SO_3^+ ions from sulfite and its pronounced appearance from sulfate furnish a simple method for the identification and differentiation of sulfites and sulfates.

A major effort is being made to develop a soft, general, efficient method of vaporization and ionization. In particular, studies with a high-energy pulsed laser are being made. The controlled, extremely rapid heating provided by a short laser pulse is expected to provide undissociated ions of the parent molecules. This source is being interfaced with an existing focal plane mass spectrometer with EOID, allowing simultaneous measurement of ions within the mass range of 25-500 atomic mass units from single aerosol particles.

The health effects of aerosol particles depend on the size and chemical composition of individual particles rather than the overall mixed composition. Most methods now used for analysis of particulate matter give information only on the average elemental composition. The development of a single-particle chemical analyzer could provide a breakthrough in aerosol analysis and perhaps find important applications in air pollution, public health, and atmospheric science.



Schematic of the particle analysis by mass spectrometry system.

D48

OCEAN BOTTOM EXPLORATION SYSTEM

A collaborative effort between JPL and the British Institute of Oceanographic Sciences (IOS) has resulted in a unique synoptic image of the Atlantic Ocean floor near the Azores. Using image processing techniques developed for space missions, a mosaic was produced enabling ocean scientists to view significant portions of the ocean bottom at about the same scale that Earth scientists view the Earth using data from Landsat or Seasat.

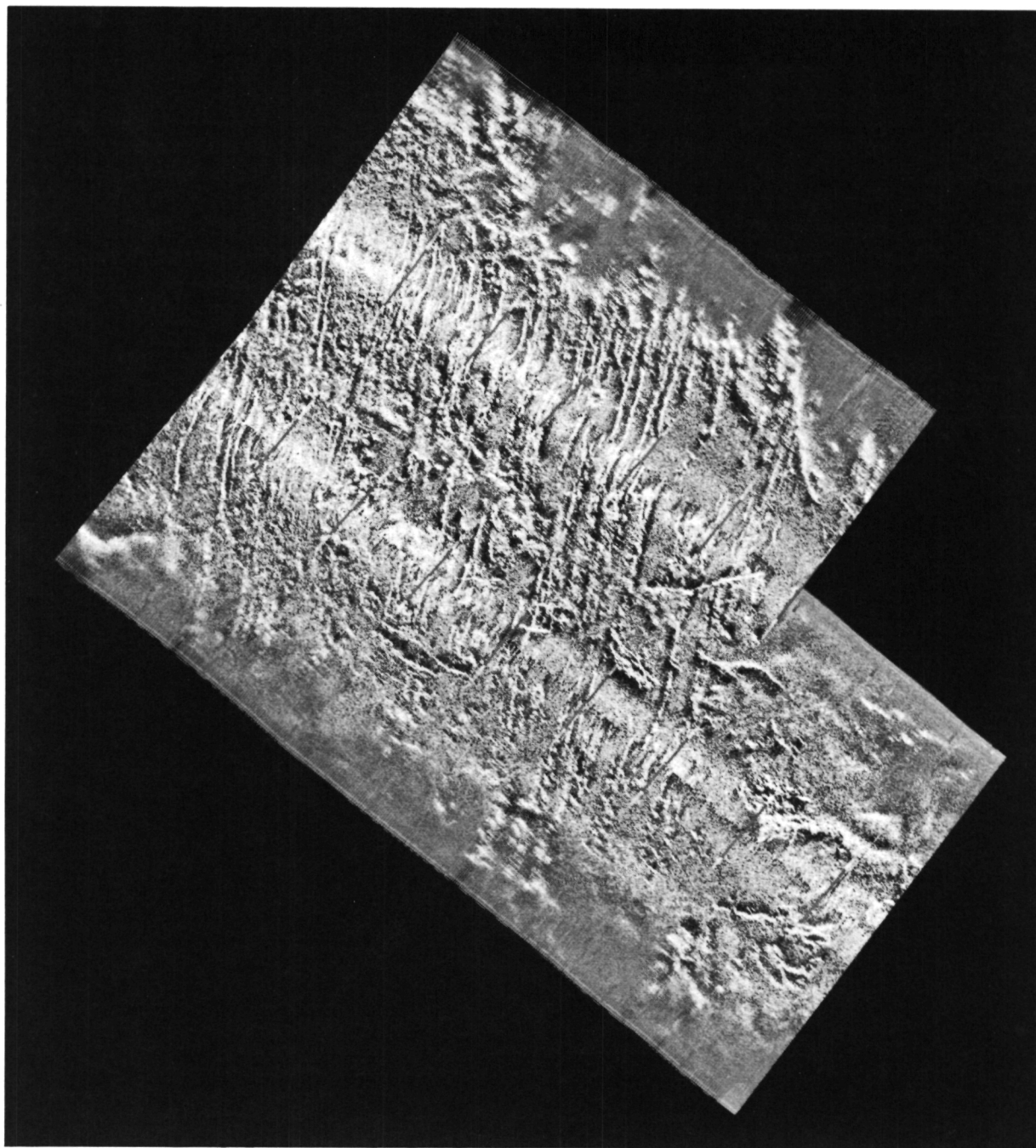
The striking 90 x 90-kilometer image of the Mid-Atlantic Ridge was generated from analog recordings of long-range side-looking sonar signals made by IOS

scientists employing a GLORIA system towed by the RRS Discovery during a 1978 oceanographic voyage. (GLORIA stands for Geologic Long Range Inclined Asdic.)

At JPL signals were digitized and submitted to computer processing, analysis, and enhancement. Images were registered to a map base and montaged to produce the mosaic.

Computer image processing of sonar signals at JPL is performed as part of the Seafloor Remote-Sensing Project, which applies the techniques originally developed for Earth and planetary remote-sensing.

Figure (opposite page): The scarped seafloor of the Mid-Atlantic Ridge, northwest of the Azores, is shown in this JPL mosaic produced from sonar signal recordings made by the British GLORIA system. The deep-tow system viewed the terrain at synoptic scales, 60 kilometers per swath. The image represents an area roughly 90 km on a side. The visible north-south scarps were believed to be formed by creation of new crust on the ridge coupled with a pulling apart of the ridge flanks by seafloor spreading.



D44

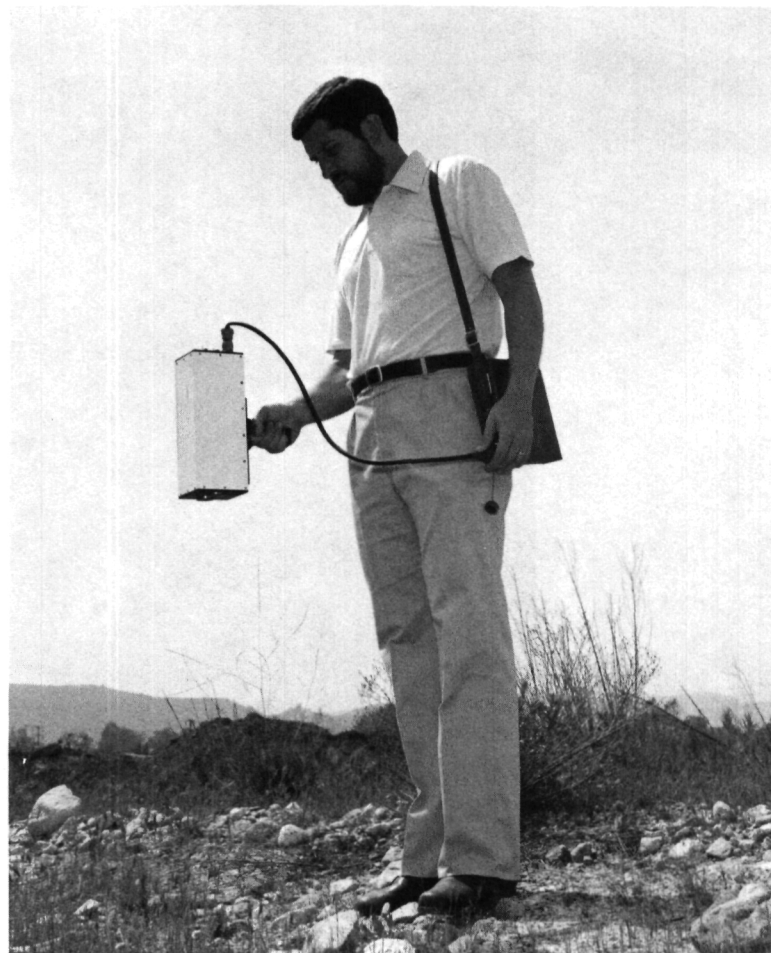
THE HAND-HELD RATIOING RADIOMETER

A new instrument has been developed at the Jet Propulsion Laboratory for use in identifying rocks and minerals in the field. The instrument, which simultaneously measures the surface radiance and displays the ratio, is an outgrowth of continuing research into remote-sensing methods for mineral and petroleum exploration.

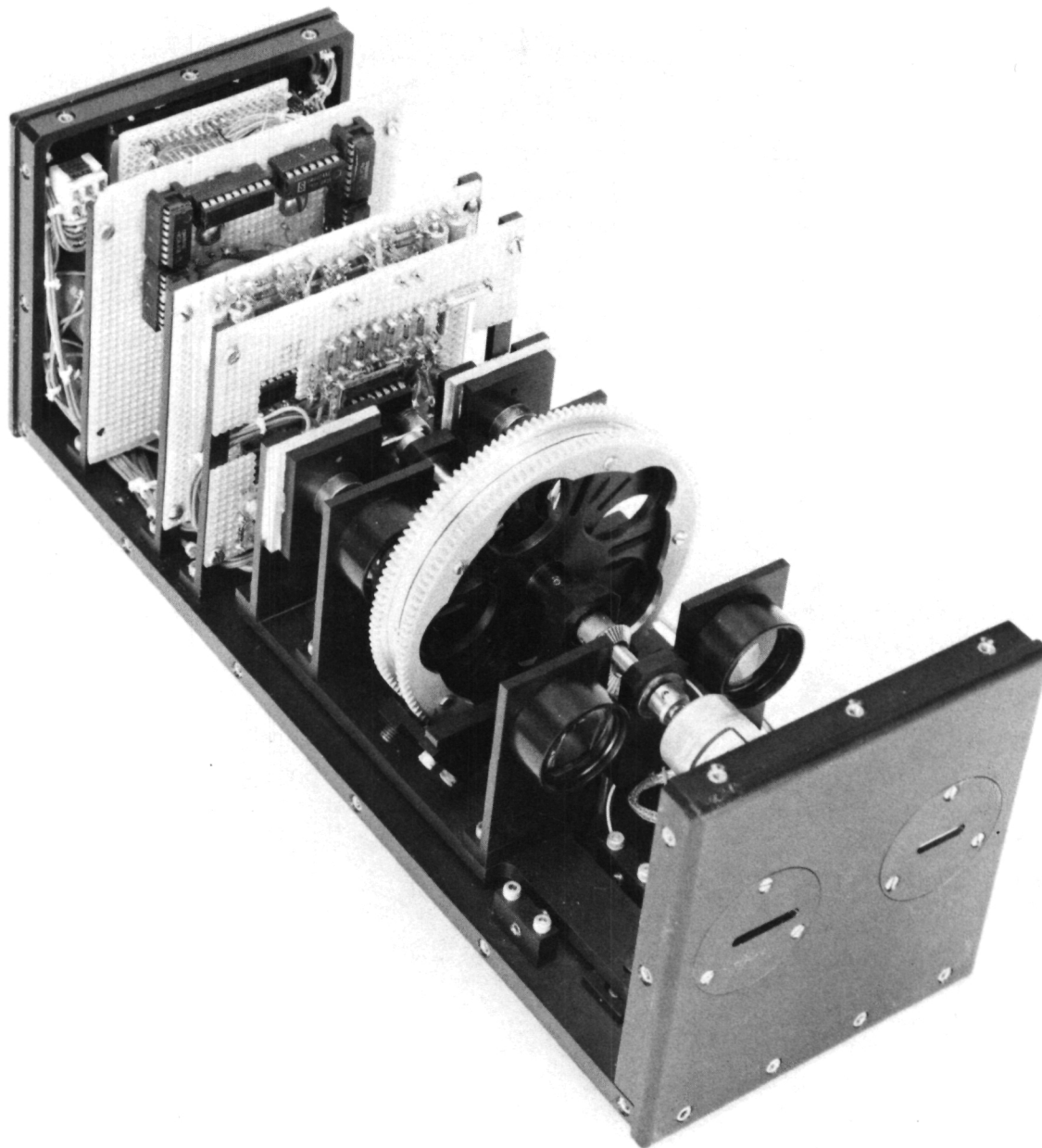
The instrument is called the Hand-Held Ratioing Radiometer (HHRR), and as its name implies is a self-contained, dual-beam, ratioing radiometer with digital readout. HHRR contains two optical trains, each containing two repeater lenses and a cooled lead-sulfide detector. One of the trains is adjustable so that measurements can be made from distances of one meter to infinity. The optical trains are intersected by set of two coaxially mounted filter wheels, each containing up to five interference filters. Filters with band passes as narrow as 0.01 micrometers can be used in the region 0.4 - 2.5 μm .

The development of HHRR was based on results obtained from the JPL Portable Field Reflectance Spectrometer that has yielded thousands of in situ reflectance spectra in the 0.4- to 2.5- μm region. Clays and carbonates, for example, have unique spectral properties in the 2- to 2.5- μm region. By using properly chosen spectral filters, and ratioing the signals to remove the effect of topography on the brightness measured, a number of materials can be identified uniquely. For instance, montmorillonite and kaolinite yield very different ratio values for filters centered at 2.10 and 2.17 μm . Therefore, for a number of materials, HHRR can be used as an analytical tool in the field. This can replace the normal procedure of returning samples to the laboratory for X-ray analysis, a procedure which is both expensive and time-consuming.

The instrument can be used on the ground or from a moving vehicle or aircraft. Caltech has applied for a patent, and Barringer Research Inc. of Denver, Colorado has taken a license to manufacture the instrument.



The Hand-Held Ratioing Radiometer being used in the field.



Closeup view of the Hand-Held Ratioing Radiometer with cover off.

Page intentionally left blank

Page intentionally left blank

VI. Basic Research

D45

LOW-ENERGY ION COLLISION STUDIES

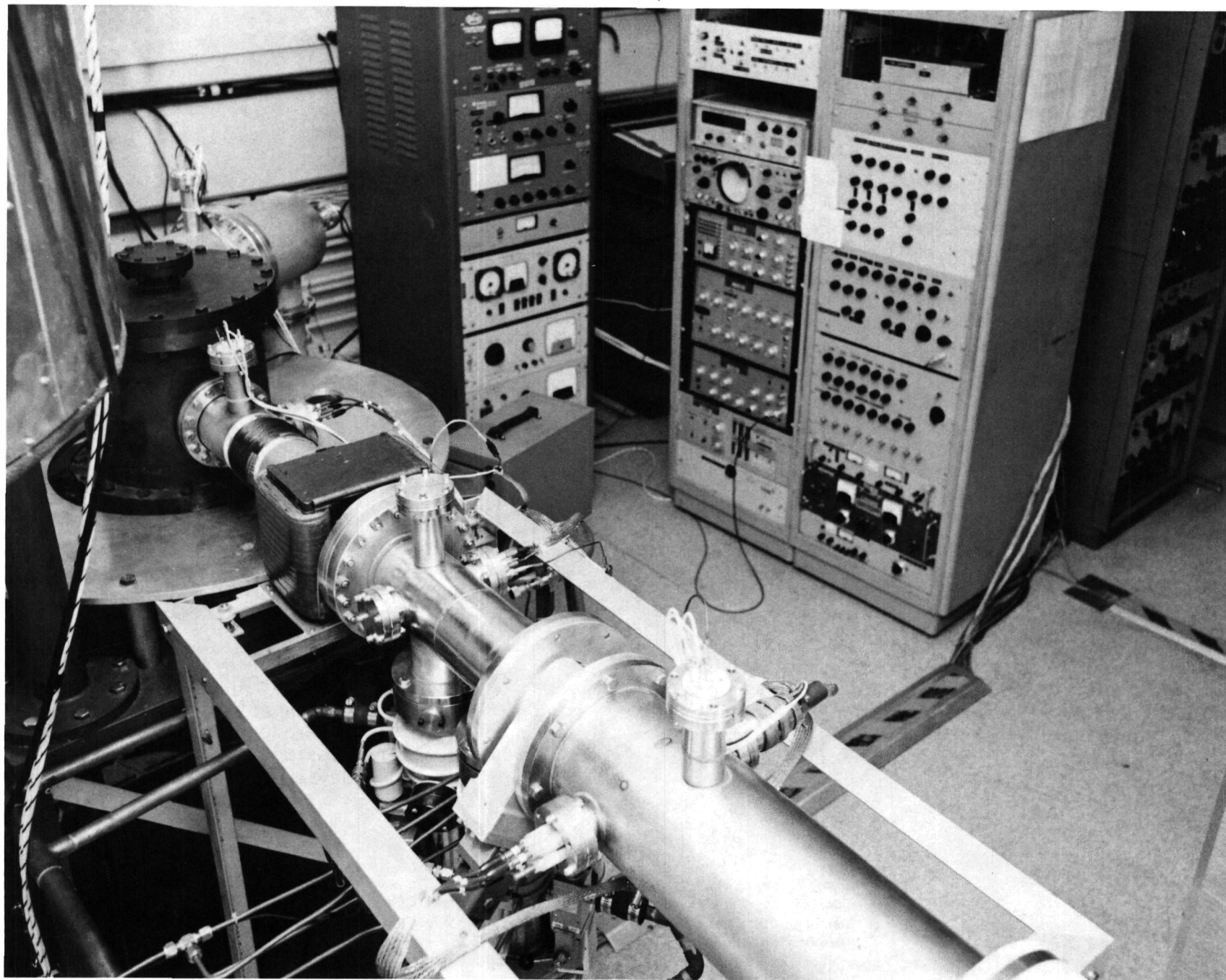
The collision of low-energy ions with neutral targets can provide, in addition to photoionization and electron ionization, yet another source of atmospheric, interplanetary and stellar electrons. The ion can penetrate into a dense medium such as the Earth's upper stratosphere or Jovian atmosphere and generate in situ a "hot stream" of energetic electrons along its path. The electrons may excite and ionize the component gases, slow down, and then attach or recombine.

With a newly designed crossed-beam apparatus, JPL researchers detected large currents of low-energy electrons in collisions of singly charged helium and magnesium ions with neutral neon, argon, hydrogen, nitrogen, and carbon monoxide. Large differential cross sections -- of the order of 0.1 square angstrom per steradian -- were measured in each system by comparing the secondary electron emission signal with elastic electron scattering signal from the neutral target. The combination of large cross section and low (0-50 electron volts) secondary electron energy means that rates of subsequent excitation, ionization and dissociation of the component gases will be significant.

Systems in which the secondary electron production can be important include the effect of solar wind protons on nitrogen and oxygen in the Earth's atmosphere; protons on carbon monoxide and carbon dioxide on the Venusian and Martian atmospheres; and protons, helium, oxygen, and sulfur ions in the Jupiter-Io system. In the Earth's atmosphere, the production of secondary electrons enhance the familiar Earth's auroral and night-sky emissions. On Venus and Mars, the excitation of CO and CO₂ will be enhanced, leading to increased optical emission from the molecules or their dissociation products, and to increased ionization of the CO and CO₂.

Interactions in the Jupiter-Io system are both complex and fascinating. Protons, sulfur, and oxygen ions can spiral into the polar regions of Jupiter, giving rise to a "hydrogen aurora" (analogous to the Earth's electron-N₂ aurora) either by direct ion-H₂ collision or via the secondary electron-H₂ path. Similar interactions can proceed through the strong accelerating electric fields present in the Jupiter-Io flux tube. Efforts are currently under way to generate beams of negative ions and sulfur ions (SII) to aid in the understanding of the Jupiter-Io system.

Figure (opposite page): Top view of the crossed-beam apparatus. Ions are generated in the lower right-hand section of beam tube, then velocity-analyzed, accelerated, magnetically deflected, and focused into the scattering center (circular tank near upper left corner). There they are crossed with the neutral beam, and emitted secondary electrons detected. Electronic racks in the background are vacuum gauge and pump control devices (left rack), data collection system (center rack), and ion/electron beam focusing potentiometers (right rack).



746

STUDIES OF ATMOSPHERIC PHOTOCHEMISTRY AND KINETICS

Several laboratory measurement techniques have been developed at JPL for studying gas-phase chemical reactions which play important roles in atmospheric chemistry. These techniques have been designed to investigate the kinetic behavior of many different chemical species over a wide range of pressure and temperature. An important goal of the JPL Kinetics Laboratory is to study the reactions of these species under the same conditions of pressure, temperature, and humidity found in the atmosphere.

Interest remains high in the effect of emissions of halogen- and nitrogen-containing species on the vertical distributions of ozone and temperature in the stratosphere. These classes of compounds may, under certain conditions, participate in catalytic cycles that upset the natural formation and destruction processes of stratospheric ozone. Information is needed on the reactions that perturb this balance.

A concerted program at several NASA centers aims to understand the chemistry and transport of atmospheric gases in the unpolluted troposphere with a view toward evaluating the atmospheric impact of urban industrial sources. The chemistry of the lower atmosphere is influenced strongly by the reactions of the methane molecule, which is produced by a number of natural biological processes. When certain oxides of nitrogen are present, the methane oxidation cycle results in

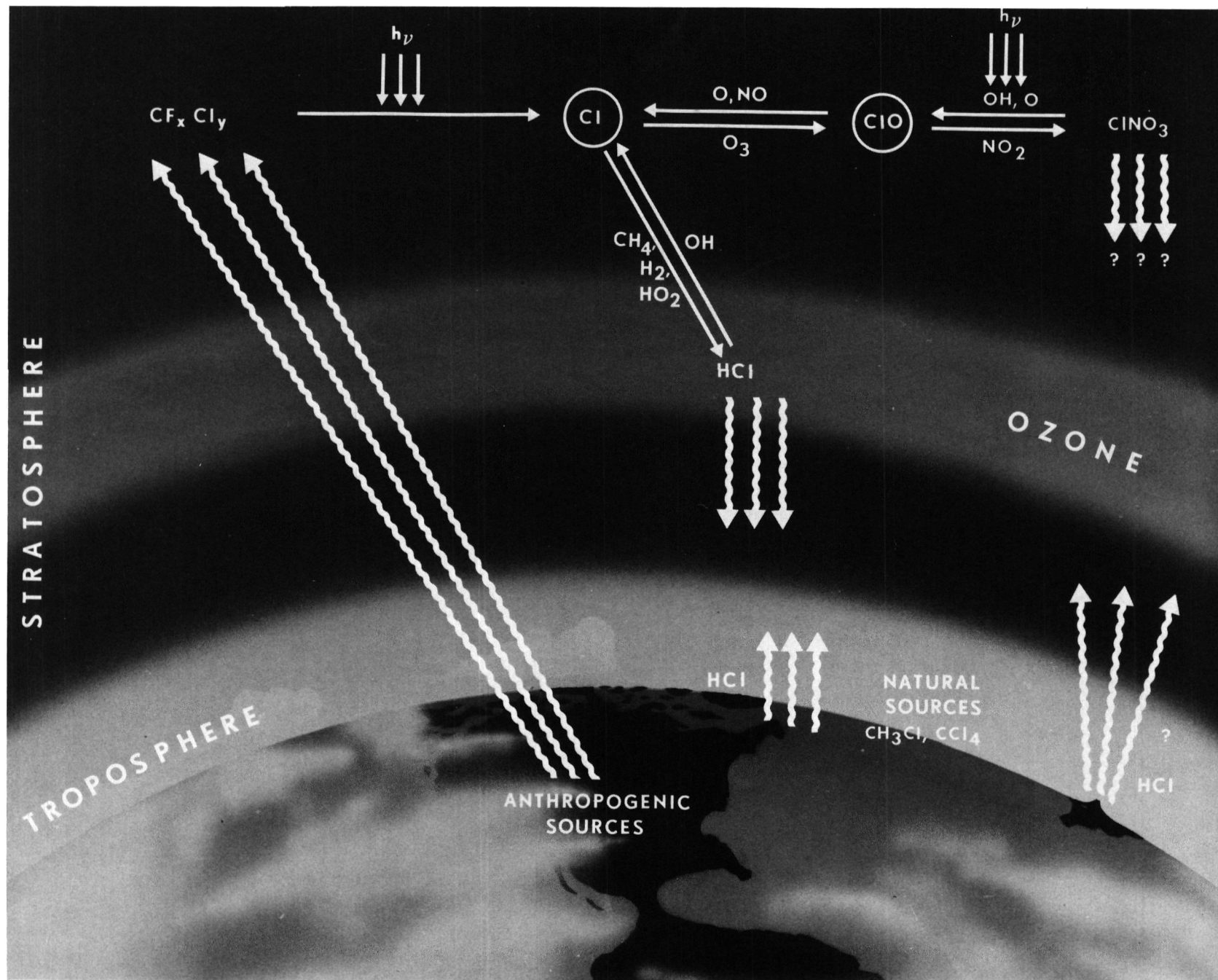
the formation of ozone. This process can be affected by industrial pollutants.

Major strides toward the understanding of the methane oxidation cycle were achieved at JPL by using a high-pressure flash-photolysis ultraviolet-absorption instrument. The first accurate measurements of the rate coefficient for the reaction of the elusive methylperoxy radical (an important species in the methane oxidation cycle) with nitrogen dioxide were made using this technique over a wide pressure range. The same apparatus was used to study the reactions of methylperoxy radicals with other trace atmospheric gases, including nitric oxide, sulfur dioxide, carbon monoxide, and other methylperoxy radicals.

Experiments with sulfur dioxide are particularly significant since it is the chemical transformation of this colorless gas into light-scattering aerosols that is responsible for visibility obscuring smog. The information gained was incorporated into complex models of chemistry and transport, which simulate the effects of pollutant emissions into the atmosphere.

The JPL laboratory also has contributed data on other atmospheric reactions involving the chlorine oxide, fluorine oxide, and hydroxyl radicals. A variety of state-of-the-art instruments has been developed using mass spectrometers, laser fluorescence systems, and other advanced detection devices.

Figure (opposite page): The drawing of Earth's atmosphere shows a highly simplified sequence of chemical reaction steps involving fluorocarbons that affect the stratospheric ozone layer. Research in the JPL Kinetics Laboratory is aimed at improving our understanding of the rates and mechanisms of these reactions. Among the important chemical species involved in stratospheric ozone (O_3) chemistry are chlorine compounds (Cl , ClO , $ClNO_3$, HCl), hydrogen (OH , HO_2 , H_2O_2), and nitrogen (NO , NO_2 , HNO_3) families as well as methane (CH_4), methyl chloride (CH_3Cl), and carbon tetrachloride (CCl_4). Other fluorocarbons are indicated by the chemical symbol CF_xCl_y .



INDEX OF NATIONAL AERONAUTICS AND SPACE ADMINISTRATION
SPONSORING PROGRAM OFFICES

OFFICE OF SPACE SCIENCE (OSS)

Deep Space Exploration

Voyager Saturn Encounter	4
Saturn's Magnetic Field	7
Saturn's Rotation Rate	8
Vertical Structure of Saturn's Equatorial Ionosphere and Middle Neutral Atmosphere	10
Jupiter's Newly Discovered Satellites	12
Jupiter's Red Spot Dynamics	14
Jupiter's Atmosphere Analyzed via Voyager Radio Occultation	17
Discovery of X-Ray Emissions From Jupiter	18
Mapping SO ₂ Frost and Sulfur on Io's Surface	20
Viking Project	22
Structures and Variations of the Atmosphere on Venus	24
Terminator and Nightside Ionosphere of Venus	26
Solar Wind Latitude Variations	28
Solar Irradiance Studies on the Solar Maximum Mission	30
High-Resolution Gamma Ray Spectroscopy Experiment on HEAO 3	32

Basic Research

Low-Energy Ion Collision Studies	98
--	----

OFFICE OF SPACE TRACKING AND DATA SYSTEMS (OSTDS)

Deep Space Navigation and Communication

New Frequency Standard Test Facility	34
Improved Hydrogen Maser Performance	36
Distribution of Standard Frequency Signals by Microwave	38
Radio Source Catalogs	40

OFFICE OF AERONAUTICS AND SPACE TECHNOLOGY (OAST), INCLUDING ENERGY

Energy and Energy Conversion Technology

Coal Pump Development	44
Supercritical Fluid Extraction of Coal	46
Solar Thermal Power Conversion	48
Extremely Low Energy Electron Studies of Gases Used as High-Voltage Insulators	52
Electric Power Systems Simulator	54
Stirling Laboratory Research Engines	56

Information Systems and Space Technology Development

Dynamic Balancing in a Vacuum	72
Spacecraft Contamination Investigations (and OSTA)	74
X-Ray Photoelectron Spectroscopy Interface Studies	76
Charge Coupled Imaging Device Test Facility	78
Development of an Ultraviolet Excimer Laser for Atmospheric Sensing	80
Advanced MPD Thruster Research	82
Nickel-Cadmium Battery Research	83
Coated Oxidizers for Stability in Space Propulsion Rockets	84
Fluorine-Hydrazine Propulsion System	86

OFFICE OF SPACE AND TERRESTRIAL APPLICATIONS (OSTA)

Earth Orbital Applications

Seasat Data Utilization: Scanning Multichannel Microwave Radiometer	60
Ocean Currents Measured by Seasat Radar	62
Ocean Wave Patterns Under Hurricanes	64
Project ARIES	66
Combining Seasat Radar and Landsat Multispectral Images	68

Technology Applications

Aerosol Particle Analysis by Mass Spectrometry	90
Ocean Bottom Exploration System	92
Hand-Held Ratioing Radiometer	94

Basic Research

Studies of Atmospheric Photochemistry and Kinetics 100

Further information concerning any project may be obtained by contacting the proper NASA program office, National Aeronautics and Space Administration, Washington, D.C. 20546.



National Aeronautics and
Space Administration

Jet Propulsion Laboratory
California Institute of Technology
Pasadena, California

ERRSAC
TECHNICAL INFORMATION CENTER